Development of high-speed two-photon microscopy for biological and medical applications

by

Ki Hean Kim

Submitted to the Department of Mechanical Engineering

in partial fulfillment of the requirements for the degree of Doctor of Philosophy in Mechanical Engineering

at the

MASSACHUSETTS INSTITUTE OF TECHNOLOGY

June 2005

Author.....

Department of Mechanical Engineering

June 3, 2005

Certified by.....

George Barbastathis

Professor of Mechanical Engineering

Certified by.....

Bevin P. Engelward

Professor of Biological Engineering

Certified by .....

Ian W. Hunter

Professor of Mechanical Engineering

Certified by .....

Peter T. C. So

Thesis Committee Chairman, Professor of Mechanical Engineering and Biological Engineering

Thesis Supervisor

Accepted by .....

Lallit Anand

Chairman, Departmental Committee on Graduate Students

Department of Mechanical Engineering

Development of high-speed two-photon microscopy for biological and medical applications

by

Ki Hean Kim

Submitted to the Department of Mechanical Engineering

in partial fulfillment of the requirements for the degree of Doctor of Philosophy in Mechanical Engineering

Abstract

Two-photon microscopy (TPM) is one of the most powerful microscopic technologies for in-vivo 3D tissue imaging up to a few hundred micrometers. It has been finding important applications in neuronal imaging, tumor physiology study, and optical biopsy. A practical limitation of TPM is its slow imaging speed (0.3 ~ 1 frames/s). We designed high-speed two-photon microscopes (HSTPMs) whose imaging speed is more than 10 times faster than traditional TPM, while their imaging depths, image contrast are comparable to those of TPM. The first high speed system is HSTPM based on polygonal mirror scanner. The scanning speed reaches 13 frames/s for typical tissues using a polygonal mirror scanner. This system is based on single-focus scanning and single-pixel signal collection. The usage of higher input power is required to compensate for the signal reduction due to higher scanning speed. However, since fluorescence signal is ultimately limited by the saturation of fluorophores due to their finite lifetimes, is the signal to noise ratio (SNR) of single focus scanning systems are also ultimately limited at high speed. This problem is circumvented in a second system based on parallelization by scanning specimens with multiple foci of excitation light and collecting signals with spatially resolved detectors. The imaging speed is increased proportional to the number of foci and similar excitation laser power per focus circumventing the problem of fluorophore saturation. However, it has been recognized that this method is severely limited for deep tissue imaging due to photon scattering. We quantitatively measured the photon scattering effect and demonstrated that its image resolution is the same as conventional TPM but its image contrast is degraded to the faster signal decay with the increase of imaging depth. We designed a new MMM based on multi-anode photomultiplier tube (MAPMT) which utilizes the advantage of MMM in terms of parallelization but overcomes the emission photon scattering problem by optimizing the design detector geometry. This method achieved equivalent SNR as conventional TPM with imaging speed more than 10 times higher

than TPM. We applied these HSTPMs to a number of novel biomedical applications focusing on studying biological problems that needs to resolve the high speed kinetics processes or or the imaging of large tissue sections with subcellular resolution to achieve the requisite statistical accuracy. In the study of transdermal drug delivery mechanisms with chemical enhancers,, large section imaging enables microscopic transport properties to be measured even in skin which is highly topographical heterogeneous. This methodology allowed us to identify the novel transport pathways through the stratum corneum of skin. In the study of tumor physiology, microvasculature in tumor tissue deep below the surface was characterized to be densely distributed and tortuous compared to that of normal tissue. The interaction of leukocyte and endothelium in tumor tissue was measured by imaging the kinetics of leukocyte interaction with blood vessel wall in tumor tissues using HSTPM. The capability of large section imaging was further applied to develop a 3D tissue cytometer with the advantages that cell-cell and cell-extracellular matrix interaction can be quantified in tissues. The statistical accuracy of this instrument was verified by quantitatively measuring cell population ratios in engineered tissue constructs composed of a mixture of two cell subpopulations. Further, this 3D tissue cytometer was applied to screen and to identify rare recombination events in transgenic mice that carry novel fluorescent genetic reporters.

Thesis Supervisor: George Barbastathis
Title: Professor of Mechanical Engineering

Thesis Supervisor: Bevin P. Engelward
Title: Professor of Biological Engineering

Thesis Supervisor: Ian W. Hunter
Title: Professor of Mechanical Engineering

Thesis Supervisor: Peter T. C. So
Title: Thesis Committee Chairman, Professor of Mechanical Engineering and Biological Engineering

Acknowledgement

I will never forget my graduate period at MIT. It was the best time of my school life. I worked quite hard, learned a lot and could figure out roughly what I want to do after school.

Of course, I couldn't have gone through without good people around me. I like to thank my advisor, Prof. Peter So first. Not to mention his excellence in research and teaching, he supported me in other aspects. He inspired me to move forward, trusted me, and showed great patience. He also showed how joyful it is to do research. He was a role model I want to follow. Another teacher I like to thank is Christof Buehler. We worked together in laboratory and he taught me how to design electronics circuit in practice. He also gave me endless advice and support. My thesis committee members, Prof. George Barbastathis, Prof. Bevin P. Engelward, and Prof. Ian W. Hunter spared their time and gave valuable advices to me.

I had many good colleagues who helped me and from whom I learned a lot. Lily Hsu Laiho was always ready to listen and advise me in all aspects. Hyuk-Sang Kwon, Daekeun Kim and Euiheon Chung gave their help whenever I needed. Judy Su was always happy to talk over cookies. Maxine Jonas showed me how to organize things. Michael Previte, and Serge Pelet were ready to answer my questions in Chemistry and Biology. Karsten Bahlmann and Tim Ragan had valuable discussion with me on various projects. Siavash Yazdanfar advised me how to make job search and social relationship. Carson Chen and Tiger Bee were always nice to me and stayed in the office with me.

I had many nice collaborators to thank. Betty Yu from Prof. Langer and Prof. Blankschtein laboratory in Chemical Engineering, MIT and I worked very productively that we could publish many papers and she also supported me to apply for academic positions afterward. Molly Stitt, Carrie Hendricks, Foster Kerrison from Prof. Engelward laboratory in Biological Engineering, MIT prepared many specimens for me and taught me cell culture. Wei-Chung Allen Lee from Prof. Nedivi laboratory in Brain and Cognitive Science, MIT prepared brain tissue specimens whenever I asked. Brendan Harley from Prof. Yannas laboratory in Mechanical Engineering, MIT generously provided material for my experiments.

I also like to thank my wife, Sunyoung Park. We encouraged each other in the final stage of graduate period. She was the person who helped me keep up writing my dissertation. She and I will continue to pursuit more achievement and contribution and love in the future. At last, I want to thank my family, especially my parents. My father gave me his endless support for me to get Ph.D. degree. My mother dedicated her life to raise her children. They sometimes talked about getting Ph.D. from MIT and I am very happy to give them my dissertation.

Table of contents

1. Introduction 14
1.1. Introduction of optical techniques 14
1.2. Two-photon microscopy (TPM) 15
1.2.1. Principle of two-photon excitation 15
1.2.2. TPM Design 18
1.2.3. Major advantages of TPM for biomedical imaging 19
1.2.4. Applications of TPM 22
1.3. High speed TPM 23
1.4. Statement of work 25
2. The development and applications of a high-speed two-photon microscopy (HSTPM) based on polygonal mirror scanner 27
2.1. HSTPM based on polygonal mirror scanner 27
2.1.1. Introduction 27
2.2. Instrument design 28
2.2.1. Experiments 32
2.2.2. Conclusions 36
2.3. Quantification of transdermal molecular transport kinetics with chemical enhancer 37
2.3.1. Introduction 37
2.3.2. Experiment 40
A Fluorescent probe selection 40
B Bulk permeability measurement 41
C Skin Sample Preparation for Imaging Experiment 42
D Two-photon 3D imaging 42
2.3.3. Results 44
A Visualization of wide-area axial scans 44
B Quantification of relative changes in transport properties 45
2.3.4. Conclusion 46
2.4. Visualization of oleic acid-induced transdermal transport pathway 47
2.4.1. Introduction 47
A Skin sample preparation 48
B Two-photon imaging 48
C Data Analysis 50
2.4.2. Conclusion 53
2.5. Tumor physiology study: microvasculature and leukocyte-endothelial interactions. 54
2.5.1. Introduction 54
A Animal model : dorsal skin-fold chamber 54
B Imaging of tumor vasculature 55
C Monitoring leukocyte-endothelium (L-E) interaction 56
2.5.2. Conclusion 58
3. Multifocal multiphoton microscope based on multi-anode photomultiplier tube (MAPMT) ... 59
3.1. Implications of tissue turbidity in MMM 59
3.1.1. Introduction 59
3.1.2. Results and Discussion 63
A Resolution variation due to emission photon scattering 63
B Signal decay due to photon scattering 65
3.1.3. Conclusion 71
3.2. Multifocal multiphoton microscope based on MAPMT 72
3.2.1. Introduction 72

3.2.2. Instrument 74
3.2.3. Results and discussion 77
3.2.4. Conclusion 86
3.3. Three-dimensional tissue cytometer 87
3.3.1. Introduction 87
3.3.2. System characterization 90
3.3.3. Procedures and Results 91
A Rare cell detection in 2D and 3D cell culture 91
B Rare cell detection in ex vivo tissue 101
C Detection of recombinant cells 102
D Discussion 104
3.3.5 Conclusion 105
4. Incorporating complementary modalities with two-photon microscopy 108
4.1. Two-photon fluorescence and confocal reflected light imaging of thick tissues 108
4.1.1. Introduction 108
4.1.2. Design of a two-photon fluorescence and confocal reflected light deep tissue microscope 110
4.1.3. Results and discussion 111
4.1.4. Conclusion 112
4.2. Single-photon counting multi-color two-photon microscope 115
4.2.1. Introduction 115
A Spectral imaging techniques 115
B Spectral-resolving devices 116
C Photodetectors 117
D Detector readout electronics 120
4.2.2. Experimental apparatus and description 122
A Experimental setup 122
B The multi-channel photon counting card 123
4.2.3. Experimental result and discussion 127
C Instrument calibration 127
D Spectral imaging of microspheres 128
E Spectral tissues imaging 130
4.2.4. Conclusions 131
5. Conclusion 132
5.1. Summary 132
5.2. Future outlook 133

List of figures

Fig. 1-1: Electronic energy diagram for two-photon excitation of fluorophores. Left side is for typical fluorescence and right side is for two-photon fluorescence. Fluorophores are excited by absorbing two excitation photons simultaneously where the energy for each excitation photon is half for excitation transition. 16

Fig. 1-2: (a) Spatial distribution of two-photon excitation, horizontal axis is optical axis (z) and vertical axis is transverse axis (r). The distribution is symmetrical around the optical axis. FWHM in z is 1.0 μm and FWHM in r is 0.3 μm with 1.0 NA and 800 nm excitation wavelength. (b) The distribution of fluorescence intensity integrated on transverse plane as function of z. Two-photon excitation has 3D optical sectioning because the quadratic relationship suppresses fluorescence generation from the cross sections which are out of focus. 17

Fig. 1-3: Configuration of two-photon microscopy. Excitation light from Ti-Sa laser is focused in a specimen by an objective lens. An x-y scan mirror scans the focus of excitation light in the specimen. The fluorescent photons generated from the scanned points in the specimen are collected by photomultiplier tube (PMT) imaging; a pulsed femtosecond laser is used as excitation light source. A detailed description is followed. 18

Fig. 1-4: Scattering of emission photons. In confocal microscopy, a pinhole in front of detector rejects scattered emission photons and collects only ballistic photons as signal. Two-photon microscopy does not need a pinhole because emission photons are generated only at the focus of excitation light. Therefore, a detector with a large detection area can collect all the photons, which arrive at the detector, as signal 22

Fig. 2-1: Schematic of HSTPM based on polygonal mirror. Polygonal mirror spins at a constant speed. Turning of each facet of the polygonal mirror generate a line scan along the fast axis. A pair of relay lens deflects the excitation beam to a galvanometer-driven mirror scanner. This mirror scanner moves the excitation beam along the slow axis. 28

Fig. 2-2: (a)–(c) Time series of a 100-μm piezo-induced linear movement of 2 μm, yellow-green spheres. Three typical images of a movie of 100 frames are depicted. (d) Accumulative image over the same time course as in (a). 31

Fig. 2-3: Two-photon, 3-D resolved images of mitochondria distribution in mouse fibroblast cells as revealed with dihydrorhodamine labeling. Left panel shows a typical two-dimensional slice. Right panel shows the 3-D reconstruction. 32

Fig. 2-4: Stroboscopically (11 frames/s) recorded movements of Calcein-AM-labeled blepharisma in an aqueous environment. Images were taken with the 253 water-immersion objective. 34

Fig. 2-5: Time-lapse sequences of euglena's movement. (a) Imaged with a wide-field fluorescence video microscope. Euglena was paralyzed within 3 s. (b) Imaged with a two-photon video-rate microscope. No photodamage was observed. The frame size is 62 mm. 35

Fig. 2-6: Schematic illustration of the brick and mortar model of the SC, including VE. The corneocytes (c) and keratinocytes (K) are represented by the brick-like structures in the continous phase of lipid bilayer lamellae (LB) that comprise the intercellular space 38

Fig. 2-7: Chemical structures of the two fluorescent model drugs. (a) RBHE is the hydrophobic model drug, and (b) SRB is the hydrophilic analog. The two molecules are similar in molecular weight, 627 Da and 559 Da, respectively, but are distinguished by functional groups that impart drastic differences. 41

Fig. 2-8: Visualization of fluorescent probe spatial distribution in the skin. Selected regions from the 4 mm2 total skin area scanned are shown for (a) RBHE control, (b) RBHE oleic acid, (c) SRB control, and (d) SRB oleic acid cases of the probe distributions close to the skin

surface. The arrow points to a circular dark region typical of stratum corneum corneocytes, whereas the intercorneocyte regions highlights in blue represent the lipid multilamellae. The box demarks the 100 μm × 100 μm area representing the field of view captured by a 40 × objective for one individual skin site. 43
Fig. 2-9: Relative changes in oleic-acid-induced transport. Key: 400 skin site RBHE (gray bar), 400 skin site SRB (white bar), RBHE limited sample size (black bar), SRB limited sample size (checked bar). The wide-area values correspond to the transport enhancement values obtained in this study utilizing the data from the 400 skin sites scanned, whereas the limited sample size values reported by a literature which is based on 4-6 sites 45
Fig. 2-10: Intensity profile analysis of the hydrophobic model drug (RBHE). For the control case, the image of the RBHE model drug spatial distribution, shown in (a), the image of the corresponding skin autofluorescence signal, shown in (c), and the intensity profile of the cross section marked in the images in (b). For the chemical enhancer case, the image of the model drug, shown in (d), the one of the skin autofluorescence in (f), and the intensity profiles in the marked cross section are shown in (e) 49
Fig. 2-11: Intensity profile analysis of the hydrophobic model drug (RBHE). For the control case, the image of the RBHE model drug spatial distribution, shown in (a), the image of the corresponding skin autofluorescence signal, shown in (c), and the intensity profile of the cross section marked in the images in (b). For the chemical enhancer case, the image of the model drug, shown in (d), the one of the skin autofluorescence in (f), and the intensity profiles in the marked cross section are shown in (e) 51
Fig. 2-12: Mice bearing dorsal skin-fold chamber 55
Fig. 2-13: Images of non-tumor-(A, B, C) and tumor-bearing mouse dorsal skin-(D, E, F). (A) Epifluorescence image of non-tumor-bearing dorsal skin shows normal vessel density and tortuosity. (B, C) two-photon images of non-tumor-bearing dorsal skin also show normal vessel density and tortuosity at the depth of 200 μm. The image shown in (B) represents the view looking down into the dorsal chamber from the surface of the chamber. The image in (C) is a 3D representation obtained by rotating the image in (B). The images were obtained using a 20 × objective and an imaging depth up to 300 μm. On the other hand, the images from tumor-bearing mouse dorsal skin shows high vessel density and tortured vascular structure 56
Fig. 2-14: Time sequence of images acquired using high-speed two-photon microscope showing L-E interaction in the dorsal skin-fold chamber. (A-E) Vessel in a non-tumor bearing chamber imaged at a depth of 150 μm below chamber window. The elapsed times are shown. The arrowhead follow a single leukocyte that had adhered to the vessel wall (A, B), released (C), and rolled along the vessel wall (D, E). (F-H) Vessel in BA-HAN-1C rhabdomyosarcoma growing in a dorsal skinfold chamber imaged at a depth of 200 μm below the chamber window. The elapsed times are shown. The arrowhead follows a single leukocyte traveling with the blood flow, not interacting with the vessel wall. The blood flow has an average velocity of 220·μm/sec. All scale bars represent 40 μ·m. 57
Fig. 3-1: Cartoon of photon scattering around two-photon excitation focus (a) excitation photon scattering reduces the amount of excitation photons arriving at the focus. Emission photons are also scattered before they are collected by detection optics and detectors. (b) Decay of unscattered photons with the increment of imaging depth in case of 2 % intralipid. Its mean free path length is 62.5 μm, 167 μm at emission (515 nm), excitation wavelength (800) respectively. It is noted that more scattering occurs to the shorter wavelength light (emission light). 62
Fig. 3-2: Variations in PSF FWHM of MMM. FWHMs in transverse direction (a) and axial direction (b) are measured up to 2 times of mean free path length (l_{em}^{s} =62.5 μm) at emission wavelength (515 nm). There is no significant change in both transverse and axial directions.

Objective used is 40 × with 1.2 NA. Input power level is approximately 5 – 10 mW at specimens. Acquisition time is 6.6 s per frame. 64
Fig. 3-3: Intensity decay with the increase of scattering length (a): peak intensity of PSF and PSF intensity integrated over the image plane. Peak intensity decays faster than the integrated intensity due to emission photon scattering. Variations in PSF profiles with the increase of scattering length (b): PSF is measured up to 100 μm radius from peak location. Intensity in the tail of PSF (> 25 μm) is monitored to increase due to scattering of emission photons... 66
Fig. 3-4: Simulation of the effect of emission photon scattering on image contrast: measured PSF profiles are used in the simulation. The original image is circles of 10 μm diameter arranged with 40 μm separation distance. (a) is the image on the surface and (b) is the image at 2.4 times scattering length at emission wavelength. Background noise decays less than signal with the increase of scattering length. Background intensity around the center circle increases due to background accumulation from other circles around. Signal to noise ratio (SNR) with the background noise included is lower than the SNR with signal fluctuation only, (c). 69
Fig. 3-5: Comparison of SMM and MMM in turbid brain tissue imaging: images of gfp expressing neurons at 10 μm deep, 80 μm deep, and 160 μm deep from the surface. Images from SMM keep good contrast up to 160 μm deep with neurons visible. Neurons are not quite visible at 160 μm deep, because images from MMM lose contrast quickly due to emission photon scattering. Image size is 160 μm × 160 μm deep. 70
Fig. 3-6: Schematic of multifocal multiphoton microscope based on MAPMT. Excitation beam (expanded) comes from bottom of this figure and illuminate a square microlens array. The microlens array splits the excitation beam into 8 x 8 multiple beams (beam-lets). In this figure, only two beam-lets are ray-traced. A specimen is scanned with an 8 x 8 array of excitation foci. The sample area that each excitation focus covers becomes small. The emission beam-lets are either collected by CCD or MAPMT. CCD integrates signal during the scanning of a single frame. MAPMT which has only the same number of pixels as excitation beamlets, integrate signal of 8 x 8 pixels synchronized with the scanning. 73
Fig. 3-7: Human skin image acquired with MAPMT-based MMM. Epidermal layer was imaged. From left to right, imaging depth goes deeper. Stratum corneum layer (a), stratum granular (b), and basal layer (c) are shown. Cells are visible with its autofluorescence. Image size: 360 um x 360 um, input power: 7 mW per focus, objective: 20 ×, imaging speed: 2.5 frames/s with 320 x 320 pixels. 77
Fig. 3-8: Signal decay with the increase of imaging depth was measured with SMM, CCD-based MMM, and MAPMT-based MMM. The specimen was sparsely distributed 4μm red spheres (605 nm) in 2 % intralipid. Signal decay is due to scattering of both excitation and emission photons. Decay due to excitation photon scattering is the same for all the systems. Difference in the decay is because the difference in the collection efficiency of emission photons of the systems. Scatterer: 2% intralipid emulsion, the mean free path length at emission wavelength is 80 um. Objective: 20 ×. The signal decay is expressed an exponential function, . The decay coefficient, c is 1.22, 1.87, 2.30 in case of the SMM, MAPMT-based MMM, and CCD-based MMM respectively. 79
Fig. 3-9: Effect of emission photon scattering on images acquired with MAPMT-based MMM. (a) The image of spheres at 150 μm deep from the surface. Ghost images appear with the scattered emission photons collected in neighboring pixels of the MAPMT, (b) image after the deconvolution process, (c) Variation of PSF due to emission photon scattering, the increase of intensity in the tail is the effect of emission photon scattering (d) Crosstalk in the pixels of the MAPMT, it is calculated by integrating the PSF over the effective detector area of individual pixels of MAPMT. 80

Fig. 3-10: Neuron images acquired with CCD-based MMM (a-c) and MAPMT-based MMM (d-f) at different depth locations (surface, 30 um, and 75 um deep). The images with at For images with MAPMT-based MMM, a deconvolution algorithm was applied to remove the effect of emission photon scattering (g-i). Objective: 20 × water immersion with NA 0.95, input laser power: 300 mW at 890 nm wavelength, frame rate is 0.3 frames per second with 320 × 320 pixels. 83
Fig. 3-11: Cell counting in the mixture of two subpopulations (ECFP, EYFP expressing cells) in 2D. (a-c) are images of mixture ratio 1/10 specimen from yellow channel (YC), cyan channel (CC), and from ratio analysis each. The cell pointed with an arrow is an EYFP cell which appears only in YC. It appears as a high ratio in the ratio image. (d) is ratio image of cell mixture 1/100. Only two EYFP cells were found. (e) shows that measured ratios agree well with expected ratios 94
Fig. 3-12: Cell counting in the mixture of two subpopulations in 3D. One group of cells was stained with Hoechst only and the other group was stained with both CellTracker green and Hoechst. Cells were grown in collagen scaffolds to generate 3D cell blocks. (a) is 3D image of 1/1 ratio specimens. Nuclei stained with Hoechst are shown as blue color and the cells stained with CellTracker green also are shown to express green color in their bodies. (b) is cell scatter plot from 1:1 ratio specimens. Two subpopulations are clearly distinguished by the difference in intensity ratio. (c) is the result of cell counting from specimens of different mixture ratios up to $1/10^5$. Measured ratios agree quite well with the expected ratios 97
Fig. 3-13: Algorithm for discriminating and counting cell populations, (a) and (b) are raw images, blue channel (BC) and green channel (GC). These images are converted to BW images (c, d) with thresholding on BC images and measuring the intensity ratio in individual pixels. Noise is removed by erosion and dilation operation (e, f). These BW images are convolved with a kernel image (g) to measure locations of nuclei and to count them (h, i). (j) is 3D view of the convolved image (h). 99
Fig. 3-14: Large section image of ex-vivo human skin in dermal layer. Images are acquired with the high-speed multiphoton microscopy based on polygonal scanner running at 13 frames per second. Collagen and elastin fibers are shown based on their autofluorescence. The size of images is 2.5 mm × 2.5 mm in (a). (b) and (c) are zoomed image from boxed regions of (a). (b) is the image of hair follicle, a cell cluster at the bottom of hair follicle are shown based on their autofluorescence (NAD(P)H). (c) is an image of sweat gland. 101
Fig. 4-1: Partial schematic of the proposed deep tissue microscope including an octagonal mirror system for fast scanning and a reflected confocal beam path: S - sample, OBJ - objective, DIC - dichroic mirror, EXL -excitation tube lens, SL - scan lens, XYS - x-yscanner, M - mirror, OCT - octagonal mirror scanner, BS - beamsplitter, FL - focusing lens, PH - pinhole aperture, LAS - laser light source, EML - emission tube lens, DSL - de-scan lens, P1 - fluorescence PMT, P2 - confocal PMT. Thin black doted lines denote infrared excitation and reflected light signal. Thick gray solid lines denote fluorescence signal. 110
Fig. 4-2: Simultaneous two-photon fluorescence and confocal reflected light images of 15 1um latex spheres. (a) and (b) are two-photon and confocal images of the spheres with the sample plane positioned at the center of the spheres. (c) and (d) are two-photon and confocal images of the spheres with the sample plane positioned at the top of the sphere (about 6 μm above the center) 112
Fig. 4-3: Simultaneous confocal reflected (a) - (c) and two-photon fluorescence (d) – (f) images of frozen human skin. Stratum corneum layer in (a) and (d), basal cell layer in (b) and (e), and dermal layer in (c) and (f) 113

Fig. 4-4: Schematic diagram of the multi-color multi-photon fluorescence microscope. M : mirror, DC : dichroic mirror, BP : band-pass filter, λ/2 : half-wave plate, P : polarizer, mA-PMT : multi-anode PMT 122
Fig. 4-5: Schematic diagram of the multi-channel photon counter card (mC-PhCC). Photon pulse signals from the multi-anode PMT are recorded by 18 photon counting channels. Each channel comprises of amplifier/discriminator, one-shot, counter(#), and hold register (REG). Collected data are transferred to the temporary data storage (FIFO) in channel sequence and then transferred to the host computer either via either a parallel link (SUB-D) or high speed serial link (GigaStar). The signals RESET, GATE, ENABLE, PIX_CLK are driven by the host computer and allow the scanner to be synchronized with the data acquisition and readout procedure of the mC-PhCC. A detailed description of the mC-PhCC is given in text. 125
Fig. 4-6: Fluorescence images of *three* different color microspheres. The beads are 1, 2, and 4 μm in diameter with emission peaks at 535, 490, and 455 nm, respectively. The experimental settings are: excitation wavelength: 780 nm, power at the specimen: 5 mW, spectrum range: 100 nm, spectral resolution: 7 nm, acquisition time: 2.6 s. The color (gray level) bar represents intensity. **(a)** Images recorded from individual spectral channels **(b)** An intensity image in which signals from all 16 spectral channels are summed **(c)** Representative spectra of spheres: each of the three fluorescence spectra is derived from a style></pages><volume><style face='normal' font='d 129
Fig. 4-7: Spectrally resolved imaging of *ex-vivo* human skin (dermal layer). Experimental settings are: excitation wavelength: 880 nm, power at the specimen: 5 mW, spectrum range: 100 nm, spectral resolution: 7 nm, acquisition time: 7 second per frame. (a) Color coded intensity image where blue color represents collagen and green color represents elastin **(b)** Representative spectra at two different positions. Position A corresponds to a collagen-rich area. Position B corresponds to an elastin rich area. 130

Chapter 1

Introduction

In past decades, optical techniques have been proved to be very important in biomedical study. In this chapter, recent developments of optical techniques including two-photon microscopy (TPM) are briefly summarized with their biomedical applications. TPM is introduced including its physical principle, instrument design, and current biomedical applications. The focus of this thesis is the extension of TPM for high speed imaging. We will review existing work in high-speed TPM field and provide a motivation for our work. A statement of work summarizing the accomplishments in this thesis will be presented.

1.1. Introduction of optical techniques

Technological advances in the optical imaging and labeling have revolutionized biological studies by enabling the monitoring of cellular events in vivo and in real time. Optical techniques provide subcellular resolution in the range of 200 nm and induce minimal photodamage. There are many optical contrast mechanisms suitable for biomedical imaging such as reflectance, fluorescence, polarization, and absorption. Several microscopic techniques such as confocal microscopy, two-photon fluorescence microscopy (TPM), and total internal reflection microscopy have 3D resolution. Imaging resolution has been improved down to a few tens of nanometers using 4-pi microscopy and stimulated emission depletion (STED) microscopy. Image acquisition speed has been also improved so that cellular events can be studied in video rate (30 frames/s) and beyond. Advances in fluorescent labeling technology make it possible to monitor molecularly and biochemically specific cellular processes. Fluorescent markers based on green fluorescent protein (GFP), which can be incorporated into the genome, enable the creation of transgenic cell lines and animals where genetic changes can be monitored. Quantum dots, which are based on semiconductor crystal in nanometer scale, allow long

term fluorescence imaging without photobleaching. They emit different colors depending only on their sizes while excitable over a broad spectral range.

Among all these advances, two-photon microscopy (TPM) is one of the most important inventions in optical microscopy in the past decade. Two-photon microscopy (TPM), which was first implemented in 1990 (Denk et al. 1990), is a 3D imaging technique with subcellular resolution. It is based on the nonlinear excitation of fluorophores. It has excellent penetration depth of several hundred micrometers while induces minimal photodamage. TPM has become an indispensable tool in various biomedical studies which requires in-vivo tissue imaging. More details of TPM are explained below.

1.2. Two-photon microscopy (TPM)

1.2.1. Principle of two-photon excitation

TPM utilizes two-photon excitation (TPE) of fluorophores. Different from conventional, one-photon excited, fluorescence where a fluorophore is excited by absorbing a single excitation photon, two-photon excitation requires the simultaneous absorption of two excitation photons (Fig. 1-1). In two-photon excitation, the energy of the excitation photons is chosen such that the excitation transition of fluorophores requires the combined energy of two excitation photons. Therefore, two-photon excitation wavelength is approximately twice longer than one-photon excitation of a given fluorophore. Two-photon excitation light is typically in near-infrared range. An important feature of TPE is that photo-interaction is localized in 3D at the focus of the excitation light. This localization is due to the quadratic relationship of TPE with excitation photons which requires simultaneous absorption of two excitation photons. The probability of TPE per molecule, $P_{2\gamma}$ is proportional to the square of excitation photon flux, $I_{ex}(t)$. For comparison, the probability of one-photon excitation, $P_{1\gamma}$ is linearly proportional to the flux of its excitation photon.

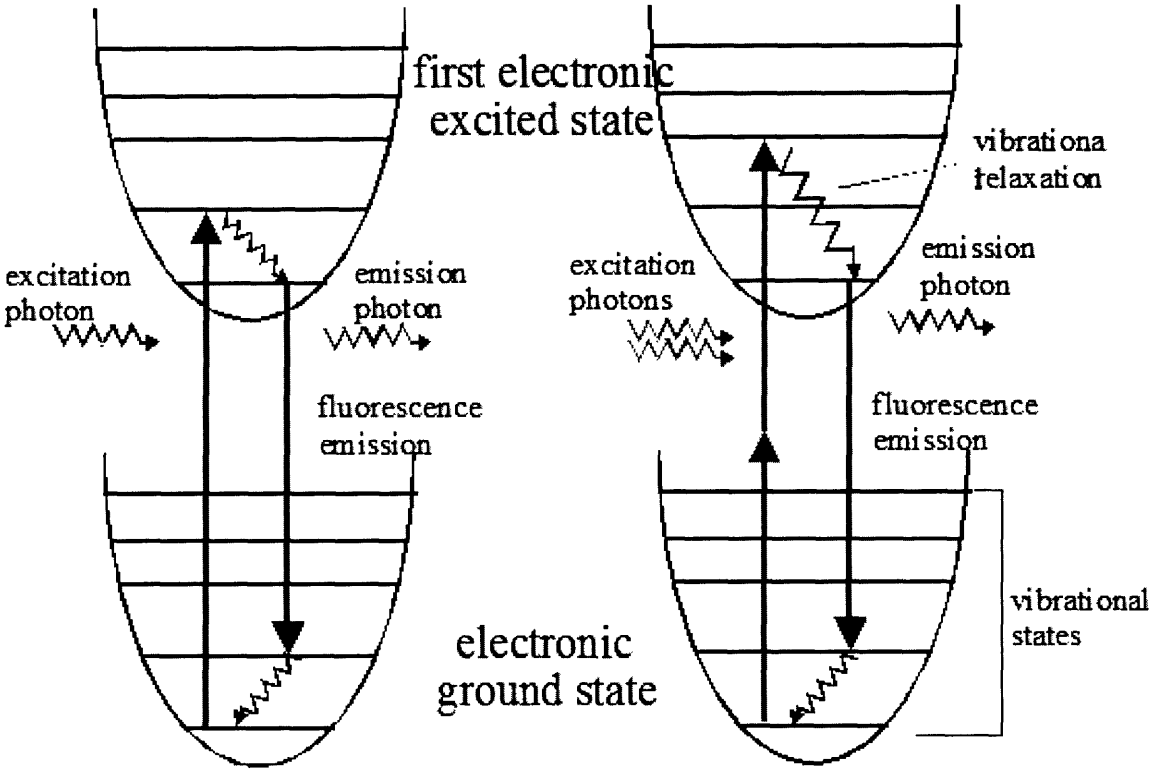

Fig. 1-1: Electronic energy diagram for two-photon excitation of fluorophores. Left side is for typical fluorescence and right side is for two-photon fluorescence. Fluorophores are excited by absorbing two excitation photons simultaneously where the energy for each excitation photon is half for excitation transition. Equation Chapter 1 Section 1

$$P_{1\gamma} \propto I_{ex-1\gamma}(t)$$
$$P_{2\gamma} \propto [I_{ex-2\gamma}(t)]^2 \tag{1-1}$$

The photon flux distribution at the excitation focus is described by diffraction theory of light. Fig. 1-2(a) shows the spatial distribution of the square of excitation photon flux around the focus. Its distribution is symmetrical in the optical axis and is presented as the function of the distances along the optical axis (z) and the transverse axis (r) with their origin placed at the focus. This distribution is normalized with the maximum intensity at the origin. The distribution shows the fast decay of two-photon excitation probability from its origin along both optical and transverse axis. Mathematically, the TPE point spread function (PSF) along both axes is described as

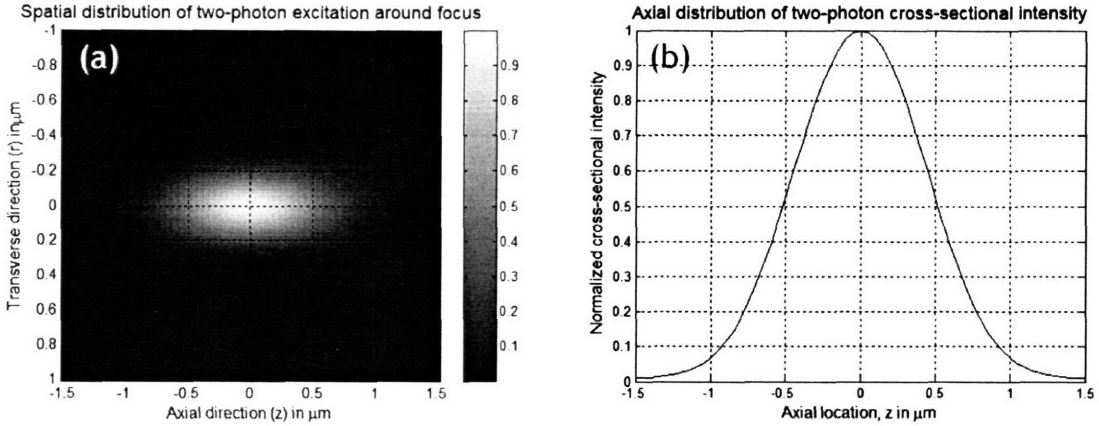

Fig. 1-2: (a) Spatial distribution of two-photon excitation, horizontal axis is optical axis (z) and vertical axis is transverse axis (r). The distribution is symmetrical around the optical axis. FWHM in z is 1.0 μm and FWHM in r is 0.3 μm with 1.0 NA and 800 nm excitation wavelength. (b) The distribution of fluorescence intensity integrated on transverse plane as function of z. Two-photon excitation has 3D optical sectioning because the quadratic relationship suppresses fluorescence generation from the cross sections which are out of focus.

$$P_{2\gamma}(v,u=0) \propto [\frac{J_1(v)}{v}]^4 \quad where \quad v = \frac{2\pi \mathrm{NA}}{\lambda} r$$
$$P_{2\gamma}(v=0,u) \propto [\frac{\sin(u/4)}{u/4}]^4 \quad where \quad u = \frac{2\pi \mathrm{NA}^2}{\lambda} z \qquad (1\text{-}2)$$

In the equations, v and u are generalized coordinates along r and z directions respectively, NA is the numerical aperture of a focusing lens (objective), λ is the wavelength of excitation light, and $J_1(v)$ is Bessel function of the first kind of order 1. These are fourth order equations due to the quadratic dependence of the excitation probability to the excitation flux. The spatial distribution of TPE around the focus of excitation light is presented in Fig. 1-2 (a). With the wavelength of excitation light being 800 nm and NA of the focusing lens being 1.0, its full width at half maximum intensity (FWHM) are 0.3 μm, 1.0 μm in transverse, axial direction respectively. Further, TPE itself has depth discrimination [don't start sentence with also]. Fig. 1-2 (b) shows the cross sectional intensity distribution of TPE as a function of axial location (z). TPE from the out of focus cross sections is suppressed because of the quadratic relationship of TPE with the excitation photon flux. On the other hand, one-photon excitation (typical fluorescence microscopy) does not have depth discrimination, because fluorescence generated on each cross section is constant along the optical axis. Therefore, the signal

generated from the focal plane is often obscured by the background signal generated in the out-of-focus cross sections.

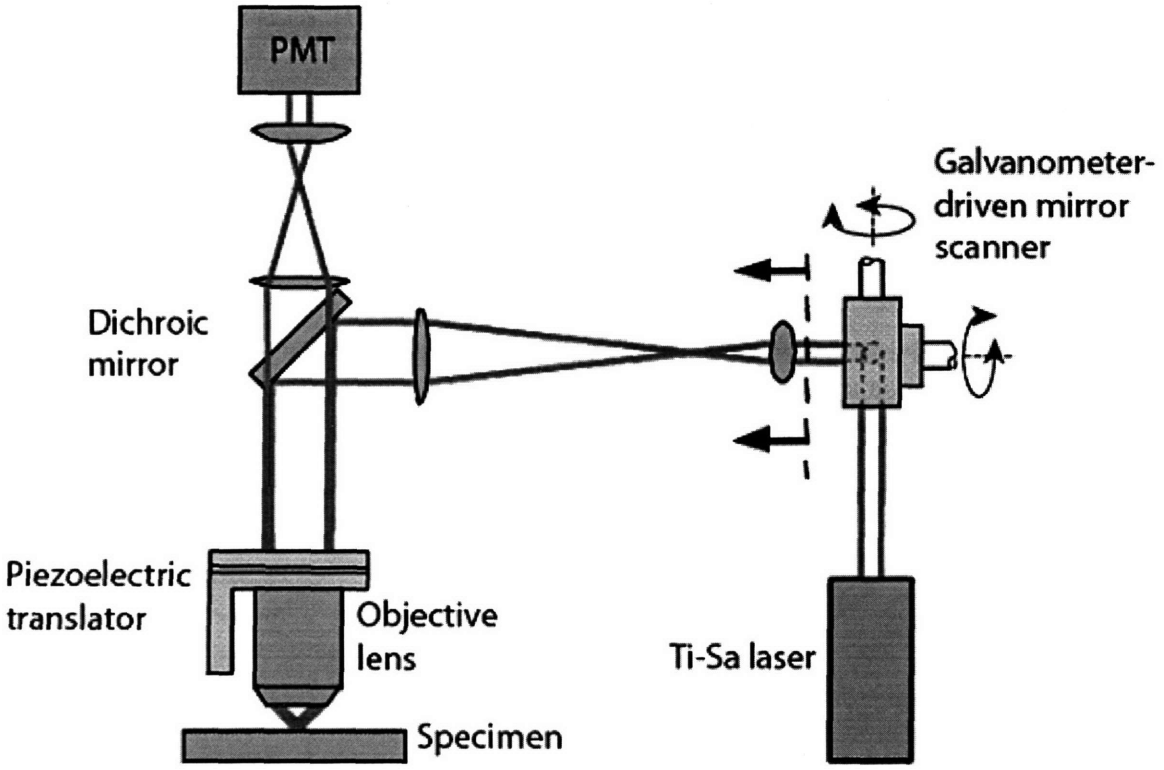

Fig. 1-3: Configuration of two-photon microscopy. Excitation light from Ti-Sa laser is focused in a specimen by an objective lens. An x-y scan mirror scans the focus of excitation light in the specimen. The fluorescent photons generated from the scanned points in the specimen are collected by photomultiplier tube (PMT) imaging; a pulsed femtosecond laser is used as excitation light source. A detailed description is followed.

1.2.2. TPM Design

The schematic of TPM is presented in Fig. 1-3. TPM generates 3D resolved images based on the localized two-photon excitation volume. An image is formed by raster scanning the focus of the excitation light using an x-y mirror scanner. The emission photons generated are collected by a detector, such as a photomultiplier tube (PMT). Two-photon excited fluorescence is an inefficient except in extremely high photon flux. In order to generate sufficient signal level for

The light source for TPM is from a Ti:sapphire laser (Mira 900, Coherent, Santa Clara, CA) pumped by continuous wave (CW) Nd:YVO_4 laser (Verdi, Coherent, Santa

Clara, CA). The laser pulse duration is 150 fs and the pulse repetition rate is about 80 MHz. The beam expanded laser light is directed into the microscope via a galvanometer-driven x-y scanner (Cambridge Technology, Cambridge, MA). Images are generated by raster scanning the x-y mirrors. The excitation light enters a microscope via a modified epi-luminesence light path. The scan lens is positioned such that the x-y scanner is at its eye-point while the field aperture plane is at its focal point. Since the objectives are infinity-corrected, a tube lens is positioned to re-collimate the excitation light. The scan lens and the tube lens function together as a beam expander which over-fills the back aperture of an objective lens. Proper over-filling of the back aperture is required for the objective to achieve the manufacturer specified numerical aperture. The excitation light is reflected by the dichroic mirror to the objective. The high numerical aperture is essential for the formation of a diffraction limited spot on the order of 0.1 femtoliter. The objective axial position is moved by a piezo-objective translator. The fluorescence emission is collected by the same objective and transmitted through the dichroic mirror along the emission path. An additional barrier filter is needed to further attenuate the scattered excitation light because of the high excitation intensity used. A de-scan lens is inserted between the tube lens and the photomultiplier tube (PMT). The de-scan lens re-collimates the excitation. It also ensures that the emission light strikes the PMT at the same position independent of scanner motion.

The microscope field of view is about 100 μm × 100 μm with a 40 × objective and it changes depending on the objective magnification. The typical frame rate is approximately 0.3 - 1 frames/s for 256 × 256 pixel images.

1.2.3. Major advantages of TPM for biomedical imaging

Localization of TPE in 3D at the focus of excitation light provides inherent 3D resolution in TPM. More importantly, the typical TPE excitation volume is below 1 fl in size minimizing phototoxicity to specimens compared to one-photon excitation in which fluorescence is generated along the path of excitation light. Photodamage is also decreased by use of near-IR excitation rather than UV and visible radiation. Reduction of the photochemical-interaction volume results in a dramatic increase in biological-

specimen viability. The noninvasive nature of two-photon imaging can be best appreciated in a number of embryology studies. Previous work on long-term monitoring of *Caenorhabditis elegans* and hamster embryos, using confocal microscopy, has failed because of photodamage-induced developmental arrest. However, recent TPM studies indicate that the embryos of these organisms can be imaged repeatedly over the course of hours without observable damage (Mohler et al. 1998; Mohler et al. 1998; Squirrell et al. 1999). It is more important that the hamster embryo was reimplanted after the imaging experiments and eventually developed into a normal, healthy, adult animal. At the focal volume where photochemical interactions occur, TPM can still cause considerable photodamage. Three major mechanisms of two-photon photodamage have been recognized. (*a*) Oxidative photodamage can be caused by two- or higher photon excitation of endogenous and exogenous fluorophores with a photodamage pathway similar to that of UV irradiation. These fluorophores act as photosensitizers in photooxidative processes (Keyse et al. 1990; Tyrrell et al. 1990). Photoactivation of these fluorophores results in the formation of reactive oxygen species that trigger the subsequent biochemical damage cascade in cells. Current studies have found that the degree of photodamage follows a quadratic dependence on excitation power, indicating that the two-photon process is the primary damage mechanism (Konig et al. 1996; Sako et al. 1997; Hockberger et al. 1999; Koester et al. 1999; Konig et al. 1999). Experiments have also been performed to measure the effect of laser pulse width on cell viability. Results indicate that the degree of photodamage is proportional to two-photon excited fluorescence generation, and is independent of pulse width. Hence, using shorter wavelength for more efficient TPE also produces greater photodamage. An important consequence is that both femtosecond and picosecond light sources are equally effective for two-photon imaging in the absence of an IR one-photon absorber (Koester et al. 1999; Konig et al. 1999). Flavin-containing oxidases have been identified as one of the primary endogenous targets for photodamage (Hockberger et al. 1999). (*b*) One- and two-photon absorption of the high-power IR radiation can also produce thermal damage. The thermal effect resulting from two-photon water absorption has been estimated to be on the order of 1 mK for typical excitation power and has been shown to be insignificant (Schonle et al. 1998). However, in the presence of a strong IR absorber such as melanin (Jacques et

al. 1987; Pustavalov 1995), there can be appreciable heating caused by one-photon absorption. Thermal damages have been observed in the basal layer of human skin in the presence of high average-excitation power (Buehler et al. 1999). As a method to avoid thermal mechanical damage in skin imaging, the usage of a laser pulse picker was suggested (Masters et al. 2004). (*c*) Photodamage may also be caused by mechanisms resulting from the high peak power of the femtosecond laser pulses. There are indications that dielectric breakdown occasionally occurs (Konig et al. 1996). However, further studies are required to confirm and better understand these effects.

Another important feature of TPM is its excellent penetration depth of up to a few hundred micrometers in turbid specimens. This is significantly improved over fluorescence confocal scanning microscopy (Centonze et al. 1998). The limitation of imaging depth is due to photon interaction with tissue constituents. In TPM, photon scattering is a major factor and photon absorption is negligible because tissue constituents have low absorption coefficient in the range of visible and near-infrared wavelength in which both excitation and emission lights are. Photon scattering is inversely proportional to the wavelength of light for both Rayleigh and Mie scattering. Since scattering effect has inverse power law dependence on wavelength, the excitation light of TPM which is in near-infrared wavelength can reach to the focus with significantly less scattering than confocal that uses UV or blue/green excitation.

For signal collection, emission photons are also scattered before collected by detection optics. The effect of scattering on signal collection is illustrated in Fig. 1-4. When scattering, the propagation direction of the emission photons are changed and may not be collected by the detection optics. In case of confocal microscopy, the emission pinhole rejects most of scattered emission photons and only ballistic unscattered photons are collected as signal. TPM does not need of pinhole for 3D resolution and hence has better collection efficiency than confocal for deep tissue imaging. The implication of emission photon scattering and its relationship with HSTPM will be further discussed in Chapter 3. The ability of TPM to image tissues up to a few hundred micrometers in-vivo opened up many biomedical applications. In the next section, current studies using TPM is summarized.

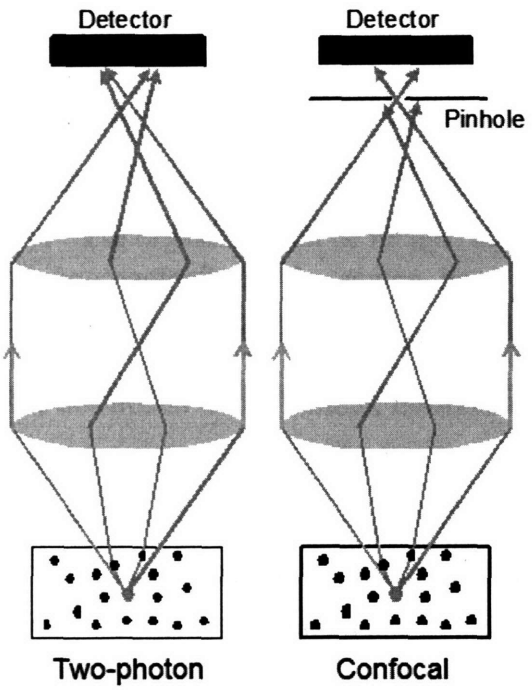

Fig. 1-4: Scattering of emission photons. In confocal microscopy, a pinhole in front of detector rejects scattered emission photons and collects only ballistic photons as signal. Two-photon microscopy does not need a pinhole because emission photons are generated only at the focus of excitation light. Therefore, a detector with a large detection area can collect all the photons, which arrive at the detector, as signal.

1.2.4. Applications of TPM

TPM provides information of 3D cellular and tissue structure based on biochemical states (endogenous and exogenous fluorophores). The advantages of TPM, excellent imaging depth and minimal phototoxicity, have provided many new opportunity for the study of tissue physiology in embryos, the brain, the eye, the pancreas, and the skin. In neuron biology study, synaptic function (especially Ca^{2+}) (Denk 1994; Denk et al. 1994; Svoboda et al. 1997; Helmchen et al. 1999; Mainen et al. 1999; Maletic-Savatic et al. 1999; Shi et al. 1999; Svoboda et al. 1999; Yuste et al. 1999) and neuronal plasticity (Engert et al. 1999; Grutzendler et al. 2002; Trachtenberg et al. 2002), blood flow (Kleinfeld et al. 1998) have been studied. In embryology, two-photon imaging allows the study of developing embryos without damage (Jones et al. 1998; Mohler et al. 1998; Mohler et al. 1998). In eyes, oxidative metabolism and cellular dynamics were measured based on autofluorescence (Piston et al. 1995). In the study on pancreas, metabolic

processes of pancreatic islets were studied (Bennett et al. 1996; Piston et al. 1999). In skin study, TPM imaged the structure of skin in 3D based on the endogenous fluorophores such NAD(P)H in cells, collagen and elastin fibers in dermal layer of the skin (Masters et al. 1997; So et al. 1998).

In addition to the physiological study of tissue, TPFM can be used as a complementary technique to guide the medical procedure in biopsy. The images provide the biochemical composition and distribution of the specimen in cellular and tissue scale. This information can distinguish the cells to be removed from the normal one that it can help to determine the surgical margin of the biopsy. It can also be used for photodynamic therapy where a light-absorbing compound is administered and preferentially retained by targeted cells and tissues. These tissues can be killed by the exposure of intense light. The localized nature of TPE allows photodynamic action to be triggered within a femtoliter volume allowing selective destruction of specific cells without harming surrounding tissues.

1.3. High speed TPM

A practical limitation of TPM is its imaging speed which typically lies in range of 0.1 ~ 2 frames per second. While this speed is sufficient in many cases, two classes of problem demand higher imaging rate. First, high speed multiphoton microscopy can be applied to study kinetic processes in 3D biological environment such as the cytosol of a single cell or within a microscopic volume of tissues. Second, high speed 3D microscope allows sampling a statistically significant volume of biological specimen. Since the field of view of most microscopes is limited to about 100 μm on a side with imaging depth of 100 μm, the investigation volume is limited to only 1×10^{-3} mm^3. While this volume is sufficient for cellular imaging, many tissues have physiologically relevant structures ranging from the cellular level up to millimeters. High-speed TPM will allow physiological study in cytological scale in vivo inside tissue. It can be also used in the study of rare cellular events in tissue combined with genetic engineering. Additionally, high-speed imaging can avoid physiological motion in diagnostic applications.

While high speed multiphoton microscopy is a powerful tool for a variety of biomedical investigation, there are significant instrumentation challenges in its implementation. Three methods have been taken to bring two-photon imaging speed to the video rate (~approximately 30 frames per second). The first method is based on line scanning (Brakenhoff et al. 1996). A line-scanning approach reduces image acquisition time by covering the image plane with a line instead of a point. The line focus is typically achieved with a cylindrical element in the excitation beam path. The resulting fluorescent line image is acquired with a spatially resolved detector such as a CCD camera. The main drawback associated with line scanning is the inevitable degradation of the image point-spread function, especially in the axial direction. The second method is based on increasing the speed of typical scanner. Two forms of HSTPM have been developed based on high speed polygonal scanner (see Chapter 2) and resonance scanner (Fan et al. 1999). The third method increases the imaging speed by parallelizing the multiphoton imaging process (Bewersdorf et al. 1998; Buist et al. 1998). It scans a specimen with a multiple of excitation foci instead of forming only a single focus. These foci are raster scanned across the specimen in parallel where each focus needs to cover a smaller area. The emission photons from these foci are collected simultaneously with a spatially resolved detector. One advantage of this method is that the imaging speed is increased by the number of excitation foci generated, without increasing the power of excitation light per each focus. In general, higher imaging speed can be achieved by using higher input power. However, there is limitation in input laser power, because fluorescence generation is saturated due to the finite lifetimes of fluorophores. The saturation level of input laser is dependent on the excitation photon flux and fluorophores. It is approximately less than 10 mW with typical fluorophores and the objectives. Scanning with multiple excitation foci has an advantage that imaging speed is increased by parallelizing, while the input power per focus is kept below the saturation limit.

Although MMM has a high imaging speed, it is questionable whether it can achieve similar tissue imaging depth as in conventional TPM. As it was mentioned before, the imaging depth in TPM is mainly limited due to photon scattering. Conventional TPM has a high imaging depth because it has a good collection efficiency of emission photons. In conventional TPM, a single-channel detector collects emission

photon while the specimen is scanned with a single excitation focus and the signal is collected by a large non-spatial resolved detector. An image is formed by the temporal encoding of the integrated signal with the known raster scanning pattern. Pixel information of the image is determined by time-encoded scanning pattern. Therefore, TPM is not sensitive to spatial dispersion of emission photon due to scattering. On the other hand, in MMM, a CCD camera generates an image by integrating emission photons from a specimen during the scanning time of a single frame. The pixel information is determined by the spatial distribution of emission photons on the CCD camera. Therefore, MMM is sensitive to emission photon scattering and MMM may not be appropriated for deep tissue imaging which is one of important features of TPM. The extension of MMM technology for deep tissue imaging is the focus of the work presented in Chapter 3.

1.4. Statement of work

This dissertation presents the development of high-speed two-photon microscopes and biomedical applications. Two high-speed systems were developed specifically for turbid tissue imaging. The first system is a high-speed scanning system based on a polygonal mirror scanner. Since this system is single-focus scanning as conventional TPM, it is advantageous in terms of emission photon collection. Since MMM has the advantageous in imaging speed but may not be suitable for tissue imaging due to its sensitivity to scattered emission photons, we thoroughly investigated the effect of emission photon scattering in TPM. Based on the measurement result, we designed a new form of MMM system that is more optimized for tissue imaging. The new MMM design uses a multi-anode photomultiplier tube (MAPMT) instead of a CCD camera as detector.

These high-speed TPMs were used in various biomedical applications. In the study of transdermal drug transport, HSTPM was used to measure the change of microscale diffusion properties of skin with the application of chemical enhancer (oleic acid). This study showed that microscopic study is possible for tissues like skin which have heterogeneous properties spatially with HSTPM. Equally importantly, HSTPM was

used to elucidate transdermal diffusion pathway with respect to skin structure. HSTPM was also applied in the in vivo study of tumor physiology in a mouse model. Microvasculature inside tumor tissues was imaged in-vivo and its difference from that in normal tissues was characterized. The response of immune system to tumors was monitored by imaging the blood flow of vessels in tumor tissues and by measuring the interaction of leukocyte-endothelium interaction. HSTPM was further used to develop high-throughput cytometric instrument. The advantage of this 3D tissue cytometer is that it can screen cells in-vivo inside tissue so that it can study cell-cell and cell-extracellular matrix interactions. Further, this method also avoids the morphological distortion during sectioning procedure in typical histology, because it can image tissue in situ without mechanical sectioning.

Realizing that spectroscopic information are critical to be combined with TPM imaging to understand biomedical processes, confocal reflected imaging was combined to TPM to provide complementary morphological information of tissues. TPM provides information of biochemical states in tissue because it is based on fluorescence (endogenous and exogenous). Confocal reflected imaging provide additional structural information such as the shapes of cells, nuclei etc as complementary. Finally, a two-photon spectral imaging system that can resolve 16 color emission in parallel in conjunction with their spatial distribution. This instrument will help in resolving and identifying tissue biochemical components with respect to their distribution.

Chapter 2

The development and applications of a high-speed two-photon microscopy (HSTPM) based on polygonal mirror scanner

The development of a HSTPM for tissue imaging is presented with its design and characterization (Section 2.1). This new system has found applications in many biomedical applications including a study on transdermal drug delivery using oleic acid as an enhancer (Section 2.2, 2.3) and a study on tumor physiology are presented in the next (Section 2.4).

2.1. HSTPM based on polygonal mirror scanner

2.1.1. Introduction

The increase of TPM imaging speed can open many biomedical study opportunities. High-speed imaging can be used to monitor kinetics events of tissue physiology with subcellular resolution in vivo. Further, using HSTPM allows tissue properties to be measured in specimen up to a size of 1 mm^3 instead of 10^{-3} mm^3 covered by a traditional TPM.

We developed a HSTPM optimized for deep tissue imaging. The imaging speed is enhanced by increasing the scanning speed using a polygonal mirror scanner that is significantly faster than conventional galvanometer-driven scanner with about 500 Hz bandwidth. The specimen is raster scanned with a single excitation focus and emission photons are collected using non-spatially resolved detectors, such as photomultiplier tubes, similar to conventional TPM. This method is advantageous for tissue imaging as in

conventional TPM featuring efficient signal collection. We will describe the system design, improvement, and characterization experiments. We further demonstrate the performance of this system in mapping three-dimensional (3-D) cellular mitochondria distribution and the motion of protozoa.

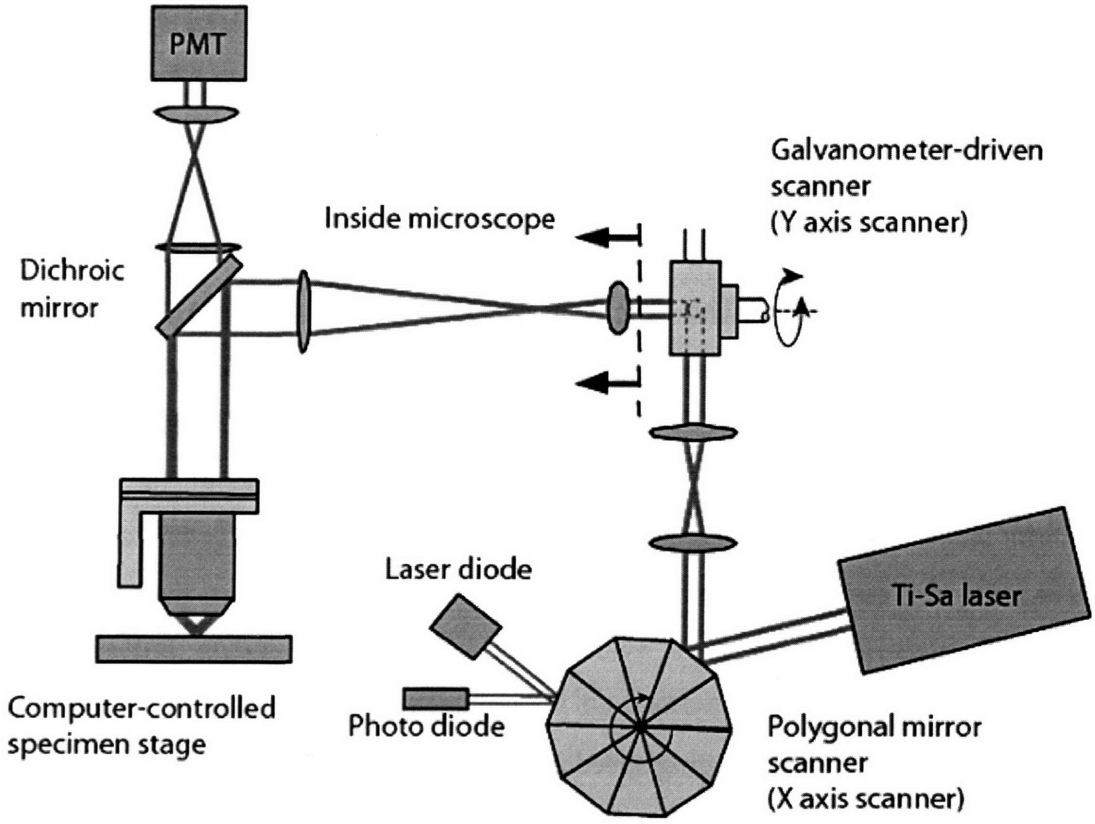

Fig. 2-1: Schematic of HSTPM based on polygonal mirror. Polygonal mirror spins at a constant speed. Turning of each facet of the polygonal mirror generate a line scan along the fast axis. A pair of relay lens deflects the excitation beam to a galvanometer-driven mirror scanner. This mirror scanner moves the excitation beam along the slow axis.

2.2. Instrument design

The schematic of this video-rate two-photon microscopy design is presented in Fig. 2-1. A femtosecond Ti:Sapphire laser (Mira 900; Coherent, Palo Alto, California) is used to induce two-photon fluorescence. The microscope system is optimized for the excitation

wavelength in the range of between 700 to 900 nm. The laser beam is rapidly raster scanned across a sample plane by means of two different scanners. A fast rotating polygonal mirror (Lincoln Laser, Phoenix, Arizona) accomplishes high-speed line scanning (x axis), and a slower galvanometer-driven scanner with 500-Hz bandwidth (Cambridge Technology, Cambridge, Massachusetts) correspondingly deflects the line-scanning beam along the sample's y axis. The spinning disc of the polygonal mirror is composed of 50 aluminum-coated facets (5 mm × 5 mm) arranged contiguously around the perimeter of the disc. The facets repetitively deflect the laser beam over a specific angular range and correspondingly scan a line 50 times per revolution. Rotation speed of 10,000, 15,000, 20,000 or 30,000 rpm can be selected. In the fastest mode, the corresponding scanning speed of 40 μs/line allows the acquisition of approximately one hundred 256 × 256 pixel images per second.

Two lenses between the scanners function together as a relay element that projects the excitation beam deflected by the polygonal mirror onto a stationary point at the center of the y-axis scan mirror. The microscope is placed such that its telecentric plane intersects with the stationary point at the y-axis scan mirror. The laser beam is coupled into an upright microscope (Axioscope, Zeiss, Thornwood, New York) by means of a modified epiluminescence light path. The beam is reflected by the dichroic mirror toward the objective and is focused on the specimen. To perform 3-D volume scans, we mounted the objective on a computer-controlled piezoelectric objective translator with an approximate bandwidth of 300 Hz (P-721.00, Physik Instrumente, Waldbronn, Germany). The maximum z-axis travel range is 90 μm. The maximum push/pull capacity is 100/20 N. Its resolution is on the nanometer scale with feedback control. Translation of the objective axially yields z stacks of xy-plane images. The induced fluorescence signal is collected by the same objective and passes through the dichroic mirror. Residual scattered light is removed by an additional barrier filter (SP700, Chroma Technology, Brattleboro, VT). The fluorescence is recorded either by an intensified, frame-transfer CCD camera (Pentamax; Princeton Instrument, Trenton, New Jersey) or a high-sensitivity PMT (R3896, Hamamatsu, Bridgewater, NJ).

In case of the CCD camera, the CCD camera integrates emission photons from specimens during the scanning time of a single frame. Then, 12-bit data of the 512 × 512 pixel CCD chip are read out at 5 MHz. The maximum achievable image transfer rate is approximately 11 frames/s for 256 × 256 pixel images (2 × 2 pixel binning). This CCD frame rate is the major obstacle in increasing frame speed of this system and can be improved by use of a faster imager. Consequently, the polygonal mirror's spinning speed is adjusted to 10,000 rpm, and the CCD exposure time is correspondingly set to 90 ms.

In case of the PMT, The current signal from the PMT is converted to a voltage signal using a transimpedance circuit with an impedance of 900 Ohms and is further conditioned by a low pass filter (BLP-2.5, Minicircuits, Brooklyn, NY). The voltage signal is measured using a 12-bit AD converter (AD9220EB, Analog Device, Norwood, MA) which has 10 Mbps speed. The signal is transferred to the computer memory through the PCI bus. Images are generated by integrating signal synchronized with the raster-scanning pattern. Rotation speed of the polygonal mirror is set at 4,000 rpm for typical tissue imaging so that the rate of line scan is 3.3 KHz. The imaging speed is approximately 13 frames per second with 256 × 256 pixel images. We select the frame rate based on the available signal strength from most tissue specimens. The field of view is approximately 200 μm × 200 μm with a 25 × objective.

An independent laser diode (1 mW at 632 nm, Thorlabs, Newton, New Jersey) along with a photodiode detector (Thorlabs) is used to encode the polygonal mirror position and to generate a reference signal. This signal is used by a custom-built circuit board to synchronize the xy scanners, the objective translator, and the CCD camera or PMT detection circuitry. The electronic circuit is based on reconfigurable logic (XS4010E, Xilinx, San Jose, California) that drastically enhances experimental flexibility.

For the given 76-MHz pulse repetition rate of the Ti:Sapphire laser, only approximately 50 pulses hit the sample during a typical pixel dwell time of 0.67 μs. It is critical to optimize the light budget for both the excitation and the emission paths. Use of circular instead of linear polarized laser light, allows the average excitation power to be

increased by approximately 40% without excitation saturation of the sample, which is essential for maintaining the diffraction-limited excitation point-spread function. The linear-polarized light of the Ti:Sapphire laser is circularly polarized by a quarter-wave plate (CVI Laser Inc., Putnam, Connecticut). Next, both the deflection angle and the diameter of the scanning beam are balanced carefully to maximize the field of view and power throughput while still overfilling the objective's back aperture for diffraction-limited focusing. A number of objectives [Fluar 100 ×, numerical aperture (NA) 1.3, oil; Fluar 40 ×, NA 1.3, oil; Plan- Neofluar 25×, NA 0.8, water; Zeiss] were used in our experiments, and the corresponding line-scanning dimensions on the specimens are 45, 113, and 182 μm. Furthermore, these high-throughput objectives, along with a high-quantum-yield photodetector, allow us to acquire approximately 5% of the total emitted fluorescence. Assuming a typical two-photon excitation volume of 0.1 fl and the fluorophore concentration of 10 μM, approximately 164 photons per pixel can be acquired with the imaging speed of 13 frames/s. Typically, to avoid excitation saturation of chromophores, the average laser power incident upon the specimen must be less than about 10 mW for the excitation wavelength in the range of 730 to 780 nm.

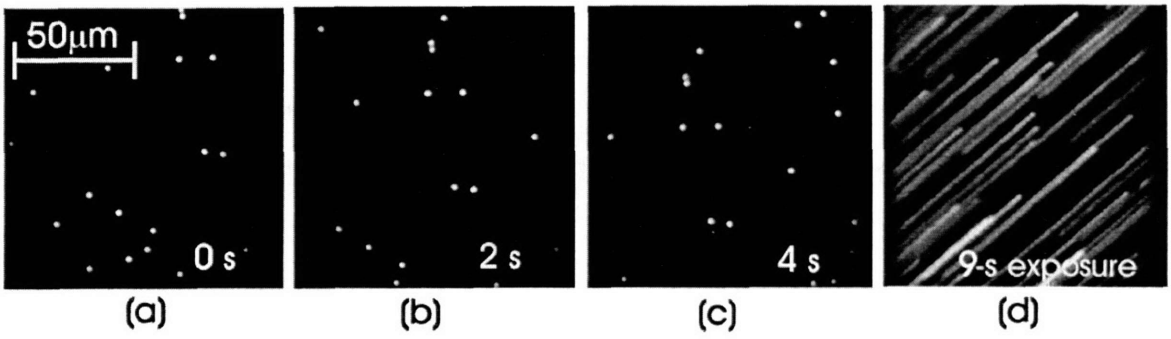

Fig. 2-2: (a)–(c) Time series of a 100-μm piezo-induced linear movement of 2 μm, yellow-green spheres. Three typical images of a movie of 100 frames are depicted. (d) Accumulative image over the same time course as in (a).

2.2.1. Experiments

To demonstrate real-time imaging with high spatial resolution, we stroboscopically recorded the piezo-driven linear displacement of a microscope slide that contained 2-mm-diameter, yellow-green latex spheres (Molecular Probes, Eugene, Oregon) immobilized in Fluoromount G (Southern Biotechnology, Birmingham, Alabama). The slide was attached to a computer-controlled piezostage that was mounted such that the spheres were shifted diagonally across the microscope's xy-image plane at a rate of 10 μm/s. An image series containing 100 frames was acquired at 780 nm. Three selected frames spanning equal amounts of time are depicted in Fig.s. 2-2 (a)–(c). If these motions were imaged at a slower rate, only the trajectories of these spheres could be seen, but the individual spheres would not be resolved. Fig. 2-2 (d) illustrates this point with a single image acquired by exposure of the sample to the CCD continuously for 9 s.

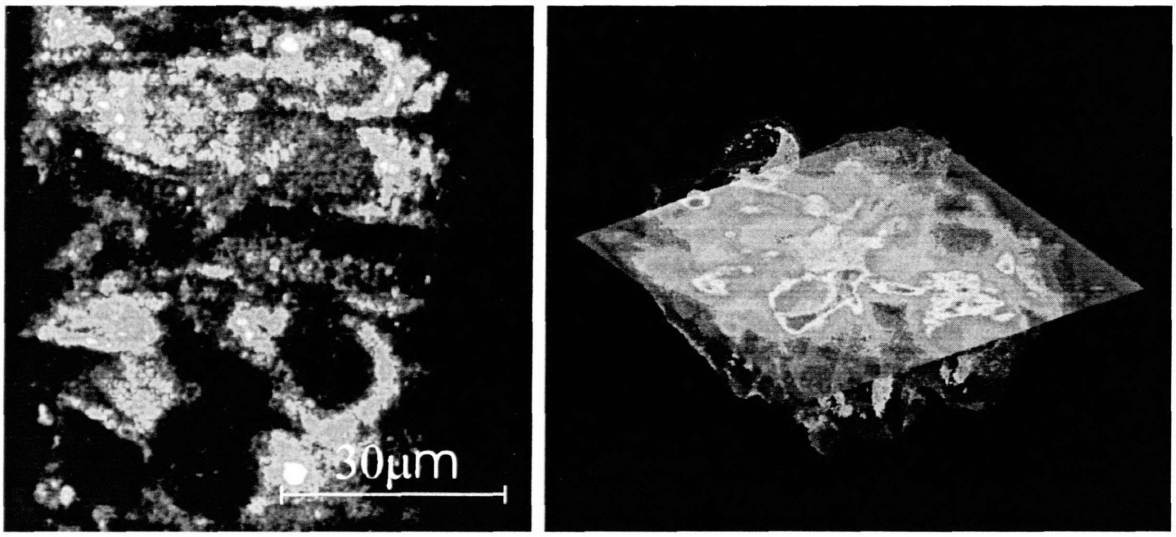

Fig. 2-3: Two-photon, 3-D resolved images of mitochondria distribution in mouse fibroblast cells as revealed with dihydrorhodamine labeling. Left panel shows a typical two-dimensional slice. Right panel shows the 3-D reconstruction.

To demonstrate the potential of 3D cellular imaging, we acquired a z-axis series of images of mouse fibroblast cells (CCL-92, ATCC, Manassas, Virginia) that had grown to approximately three cell layers thick on a cover-glass chamber slide (PGC, Gaithersburg, Maryland) containing 1 ml of medium. The sample was labeled with dihydrorhodamine (Molecular Probes), which is cell permeant and nonfluorescent. Dihydrorhodamine was first dissolved in dimethyl sulfoxide at a concentration of 10 μM. The stock probe solution was mixed with the medium in the chamber at a final concentration of 5 μM. With the presence of reactive-oxygen species within the cell, dihydrorhodamine was cleaved by reactiveoxygen species into individual fluorescent rhodamine molecules that localized in the mitochondria. One hundred images spanning a depth of 20 μm were acquired in 9 s with the excitation wavelength of 780 nm. The mitochondria distribution in the cell was visualized clearly in 3-D (Fig. 2-3). With successive scanning, the fluorescence intensity was observed to increase consistently with photoinduced production of reactive-oxygen species in cells.

The characteristic movement of blepharisma, a protozoa species, was visualized in Fig. 2-4 (Fisher Scientific Co. Hampton, Vermont). The blepharisma sample was stained with 3 mM Calcein-AM (Molecular Probes) for 15 min. With the excitation wavelength of 780 nm, we acquired a time-lapse sequence of 100 images at the top surface of the coverslip. Images of the protozoa's were captured as they swam across the scanning region. The characteristic expansion and contraction movement of the blepharisma was very fast; more than 50% change in the organism's body length could occur within 0.2 s. We could also track the rapid swimming motion of the organism at a rate as high as 1000 μm/s.

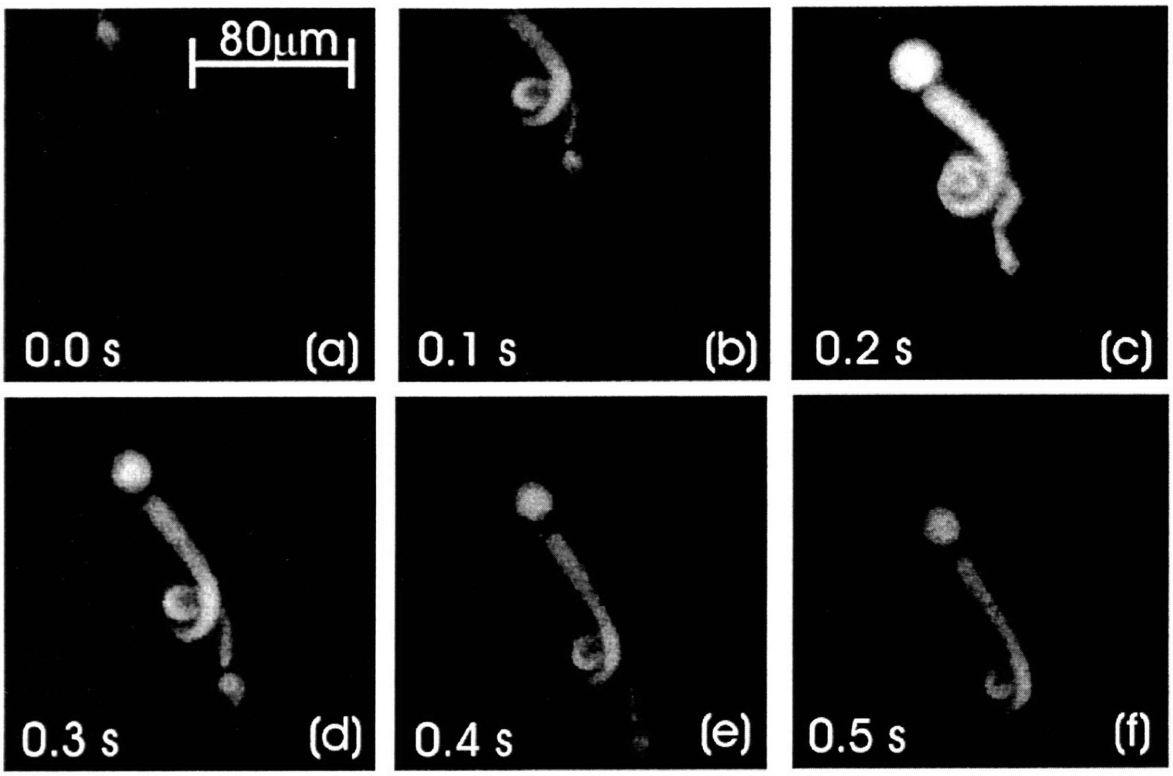

Fig. 2-4: Stroboscopically (11 frames/s) recorded movements of Calcein-AM-labeled blepharisma in an aqueous environment. Images were taken with the 253 water-immersion objective.

The reduction of photodamage is an important advantage of two-photon video-rate imaging as compared with traditional techniques, including wide-field fluorescence video microscopy and video-rate confocal microscopy. We used two-photon video-rate imaging with traditional wide-field fluorescence video microscopy to compare euglena locomotion. The imaging of euglena was based on their native chlorophyll fluorescence. A standard fluorescence microscope (Leitz, Orthoplan2, Stuttgart, Germany) equipped with a standard 100 W mercury arc lamp was used for wide-field fluorescence video microscopy. A three-color dichoric filter cube (Chroma Technology, Brattleboro, Vermont) simultaneously provided excitation wavelengths at 350, 480, and 510 nm. The fluorescence images were acquired by a video-rate 3-chip color camera (Sony, DXC-960MD).

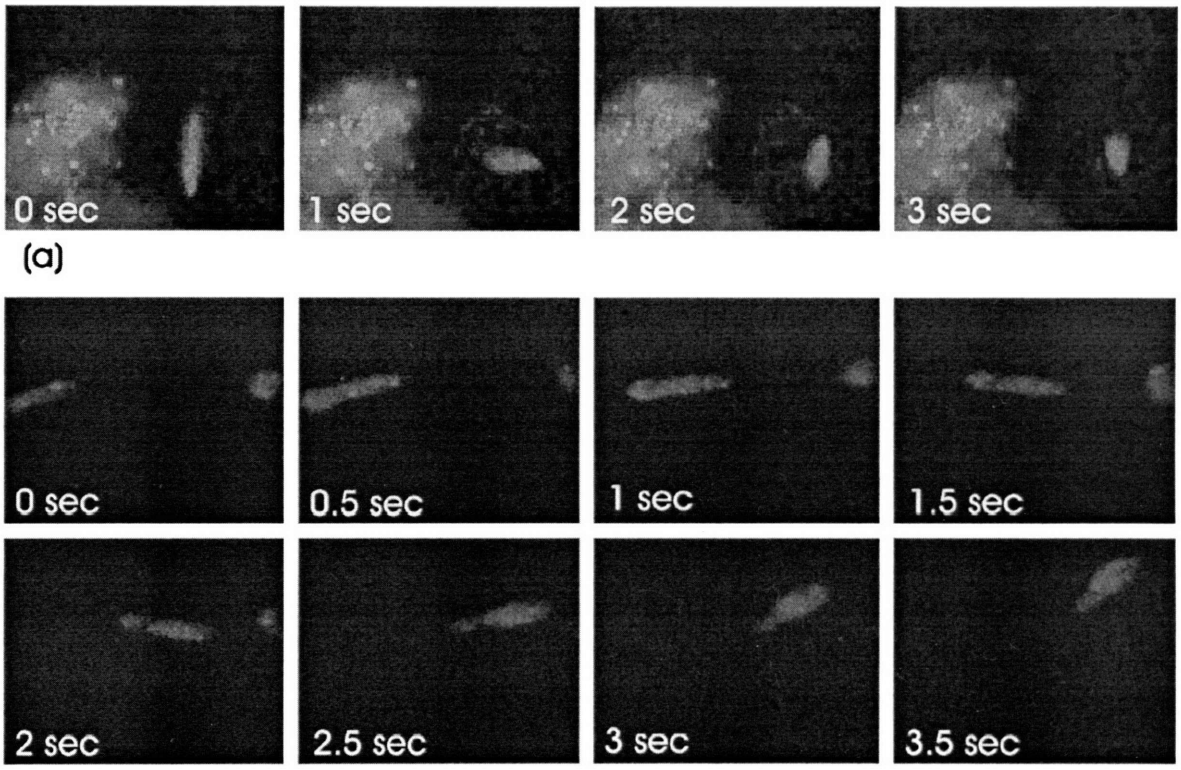

Fig. 2-5: Time-lapse sequences of euglena's movement. (a) Imaged with a wide-field fluorescence video microscope. Euglena was paralyzed within 3 s. (b) Imaged with a two-photon video-rate microscope. No photodamage was observed. The frame size is 62 mm.

Time-lapse sequence images showing the response of a euglena to the arc-lamp excitation are shown in Fig. 2-5(a). With arc-lamp illumination, the euglena was observed to lose mobility almost instantly. The organism subsequently lost control of its cell shape within 3 s. The paralyzed euglena never regained activity after 10 s of data acquisition in a standard wide-field fluorescence microscope. In contrast, euglena motility could be noninvasively imaged by the use of the two-photon video-rate microscope. A time lapse sequence of euglena swimming across the imaging area is shown in Fig. 2-5(b). No loss of motility or cell shape control was ever observed for more than 30 euglenas that swam across the observation volume. Fig. 2-6 demonstrates the less phototoxicity associated with two-photon video-rate imaging and the potential of this technology for future clinical application.

2.2.2. Conclusions

We have developed a high-speed, two-photon scanning microscope designed primarily for deep tissue imaging. We have obtained real-time tissue images with submicrometer resolution in three dimensions. We have shown that the main advantage of two-photon video-rate imaging lies with its low phototoxicity. The short, pixel dwell time due to high scanning speed requires us to optimize the light budget. Future improvement on the excitation efficiency may consist of compressing the laser pulses width by means of group velocity compensation and increasing the pulse repetition rate to approximately the inverse of typical fluorescence decay lifetimes. High-speed, 3-D, resolved two-photon microscopy provides new opportunities for the development of noninvasive biomedical applications, including optical biopsy, quantitative study of 3-D tissue architecture, and monitoring of wound healing and tissue regeneration

2.3. Quantification of transdermal molecular transport kinetics with chemical enhancer

2.3.1. Introduction

In collaboration with Dr. Betty Yu and Prof. Daniel Blankschtein in the Department of Chemical Engineering of Massachusetts Institute of Technology, we applied HSTPM for the study of transdermal drug delivery. Transdermal drug delivery is an important alternative method for drug administration as compared with other conventional methods such as oral and subcutaneous administration. Transdermal drug delivery is convenient, painless, and can avoid first-pass drug metabolism (Finnin et al. 1999). The primary barrier to transdermal delivery is the stratum corneum (SC) which is outmost layer of the skin forming a protection layer. It is comprised of closely packed corneocytes and their lipid multilamellae form an "oily" environment (Scheuplein et al. 1971; Potts et al. 1991). Therefore, SC allows the transport only small hydrophobic drugs such as scopolamine, clonidine, nitroglycerine, estradiol, fetanyle, and nicotine (Cullander et al. 1992; Schaefer et al. 1996). Many other drugs which are either large or hydrophilic can not be delivered well through the skin. The usage of chemical enhancer, which can reversibly lower the resistance, has been studied to enhance transdermal drug delivery (Golden et al. 1987; Francouer et al. 1990; Naik et al. 1995; Yoneto et al. 1995; Johnson et al. 1996b; Peck et al. 1998). Oleic acid is a well known chemical enhancer and it is known to enhance the transport by making the lipid multilamellae more fluidic (Golden et al. 1987; Francouer et al. 1990; Schaefer et al. 1996). However, many microscopic transport coefficients responsible for the total transport increase remains to be clarified including: the changes in the microscale transport properties of the permeant, including the vehicle to skin partition coefficient (K), the skin diffusion coefficient (D), and the skin barrier diffusion length (L).

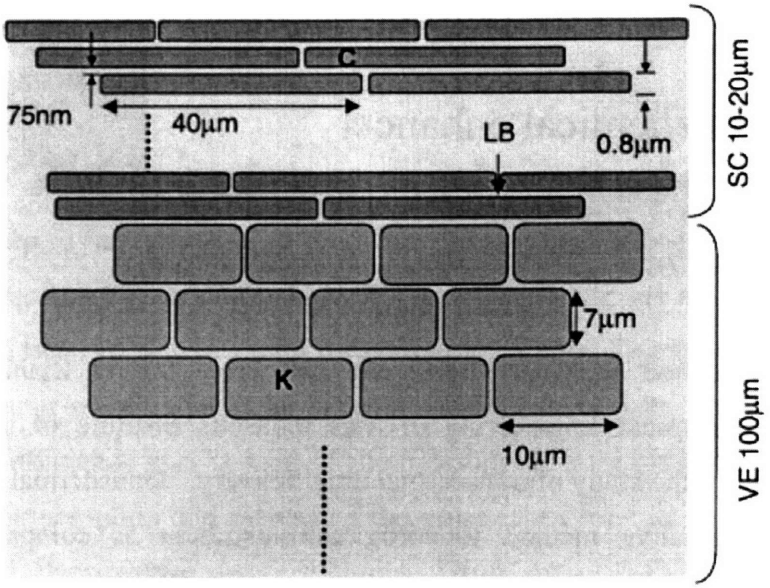

Fig. 2-6: Schematic illustration of the brick and mortar model of the SC, including VE. The corneocytes (c) and keratinocytes (K) are represented by the brick-like structures in the continous phase of lipid bilayer lamellae (LB) that comprise the intercellular space

A method was recently devised to measure the change of these microscopic transport coefficients in the presence of oleic acid based on the application of fluorescent drug models on skins and 3D tissue imaging with TPM (Yu et al. 2001). Fluorescent probes of large molecular weights as other drugs were chosen and applied on ex-vivo skin specimens without and with oleic acid. Rhodamine B hexyl ester perchlorate (RBHE) and sulforhodamine B (SRB) were used as hydrophobic and hydrophilic drug models respectively. Two-photon microscopy was used for 3D imaging through the specimens up to 32 μm deep from surface. From 3D image data, the intensity on the surface and the intensity decay with the depth increment can be measured. The surface intensity is associated with vehicle to skin partition coefficient (K). The intensity decay is related with diffusion coefficient (D) but also due other experimental factors such as light scattering in the skin. Therefore, the absolute measurement is not possible with imaging. However, the change of transport properties can be measured by comparison of specimen in the presence and absence of oleic acid enhancer. By combining the standard permeability measurement, the change of transport properties with the action of chemical enhancer can be obtained. More details are explained in the theory section.

Although this method revealed the changes of transport properties of the skin with the action of oleic acid, our initial measurements were based on 3D images of small sections (~0.01 mm^2). The measurements were based on 4-6 sites where the image areas are 100 μm × 100 μm. Realizing that skins are topographically heterogeneous, we performed follow-on experiments that sample a significantly larger skin area. The difficulty in sampling large skin area is mostly due to the slow speed of conventional TPM which is 0.3~1 frames/s. By applying HSTPM based on polygonal mirror which runs at 13 frames/s, we have succeeded in statistically quantifying transport properties changes induced with oleic acid over 4 mm^2 sample areas.

The theoretical description for the relative change of transport property with oleic acid is derived based on one-dimensional diffusion law (Fick's First Law). The steady-state flux, J of a permeant across the SC membrane with diffusion is

$$J = -D\frac{dC}{dz} \qquad \text{Equation Chapter 2 Section 1}$$

In the equation, D is permeant diffusion coefficient in the membrane, and dC/dz is the concentration gradient in z direction (the direction of increasing SC depth). Additional transport properties, which are related with experimentally measured permeability, include the vehicle to skin partition coefficient, K and the skin barrier diffusion length, l which represents the thickness of skin region over which the greatest barrier to permeant transdermal transport is exhibited. Since the diffusion coefficient, D, cannot be directly measured by our experiment. However, our experiment allows us to focus on the oleic acid induced changes in the transport properties and the enhancement of D, E_D is measured by combining permeability measurement and intensity profile. Permeability of skin, P can be measured by a standard method and related with probe flux, J by $P = J/\Delta C$ where ΔC is the difference in the probe concentration between donor and the receiver (Schaefer et al. 1996). The enhancement of diffusion coefficient can be obtained from the following formula.

$$E_P = \frac{D_E}{D_C}\left(\frac{\left(dC/dz\right)_E}{\left(dC/dz\right)_C}\right) = E_D E_g$$
$$\Rightarrow E_D = E_P / E_g \tag{2-2}$$

Where E_g is enhancement of intensity gradient and E_p is enhancement of permeability. From 3D image data, probe intensity profiles are obtained by averaging intensity on each layer. Concentration-gradient enhancement, E_g, is calculated with the linear regression of probe intensity profiles.

The enhancement of vehicle to skin partition coefficient, E_K can be easily obtained from 3D two-photon images. E_K is the ratio of surface intensity of enhancer to the one of control in case the same probe concentration is used for both control and oleic acid solutions.

$$E_K = \frac{[I(z=0)]_E}{[I(z=0)]_C} \tag{2-3}$$

Permeability can also be expressed based on other transport properties (Schaefer et al. 1996).

$$P = \frac{KD}{l} \tag{2-4}$$

By combining with (1.2), the enhancement of diffusion length is obtained.

$$E_l = \frac{E_K}{E_g} \tag{2-5}$$

2.3.2. Experiment

A Fluorescent probe selection

The two fluorescent probes (Molecular Probes, Eugene, OR), rhodamine B hexyl ester perchlorate (RBHE) and sulforhodamine B (SRB), served as the hydrophobic and hydrophilic model drugs, respectively, and were selected based on their similarity in

molecular structure, disparity in octanol-water partition coefficient, and fluorescence emission range. Fig. 2-7(a) and (b) show the chemical structures of the two fluorescent probes. Their molecular weights are similar, RBHE: 627 Da and SRB: 559 Da.

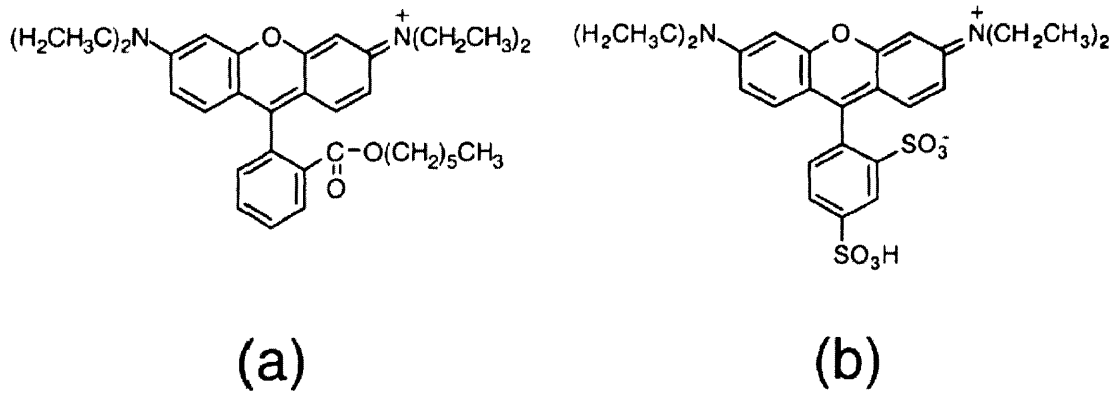

Fig. 2-7: Chemical structures of the two fluorescent model drugs. (a) RBHE is the hydrophobic model drug, and (b) SRB is the hydrophilic analog. The two molecules are similar in molecular weight, 627 Da and 559 Da, respectively, but are distinguished by functional groups that impart drastic differences.

In terms of emission color, these two probes were selected to minimize the effects of the skin autofluorescence, characterized by absorption and emission peaks of 488 nm and 515 nm, respectively. Specifically, under the 780 nm laser excitation, the fluorescence signals of the probes, their spectral absorption/ emission peaks at 556 nm/578 nm (RBHE) and 565 nm/586 nm (SRB), have minimal overlap with that corresponding to the skin autofluorescence.

B Bulk permeability measurement

Control (no chemical enhancer) and chemical enhancer solutions of RBHE and SRB, prepared as described above, were radiolabeled with the equivalent tritiated probe (American Radiolabeled Chemicals, St Louis, MO) at 1 μCi per ml. Following the procedure described in the literature, the permeability measurements were performed (Johnson et al. 1996a) in triplicate using heat-stripped skin (Peck et al. 1994; Li et al. 1998) with each of the four probe vehicles, RBHE-control, RBHE-enhancer, SRB-control, and SRB-enhancer, serving as the donor solution for each set of experiments. The skin

conductivities were measured before and after the experiments, as described above for each sample examined. The presence of radiolabeled permeants was detected with a liquid scintillation analyzer (2200CA Tri- Carb, Packard Instrument Company, Downers Grove, IL), and the steady-state permeant permeabilities were calculated with the standard formula.

C Skin Sample Preparation for Imaging Experiment

Detailed specimen preparation procedures has been previously published (Yu et al. 2003). A short description is presented here. Excised human cadaver skin (National Disease Research Interchange, Philadelphia, PA) was mounted in side-by-side diffusion cells (Permegear, Riegelsville, PA). Donor vehicle solutions of RBHE and SRB consisting of ethanol and PBS, at a 1/1 ratio, by volume, were prepared at concentrations of 0.5 mg per ml and 0.7 mg per ml, respectively. In preparing the solutions containing the model chemical enhancer, an additional 5 % by volume of oleic acid was added to the PBS/ethanol probe solutions. Skin samples were left in contact with well-stirred donor solutions for 48 h, until the steady-state diffusion profile was established. After exposure to the model drug solution, the samples were rinsed with PBS, and mounted on microscope slides.

D Two-photon 3D imaging

Four hundred consecutive skin sites in a 2 mm × 2 mm area of each skin sample were 3D imaged from the skin surface to a depth of 21 μm (at 0.7 μm intervals) using the high-speed two-photon microscope. The imaging time for each section was approximately 1.5 hours. The 400 different consecutive skin sites (each with an area of 100 μm × 100 μm) were computationally stitched together at a specific skin depth.

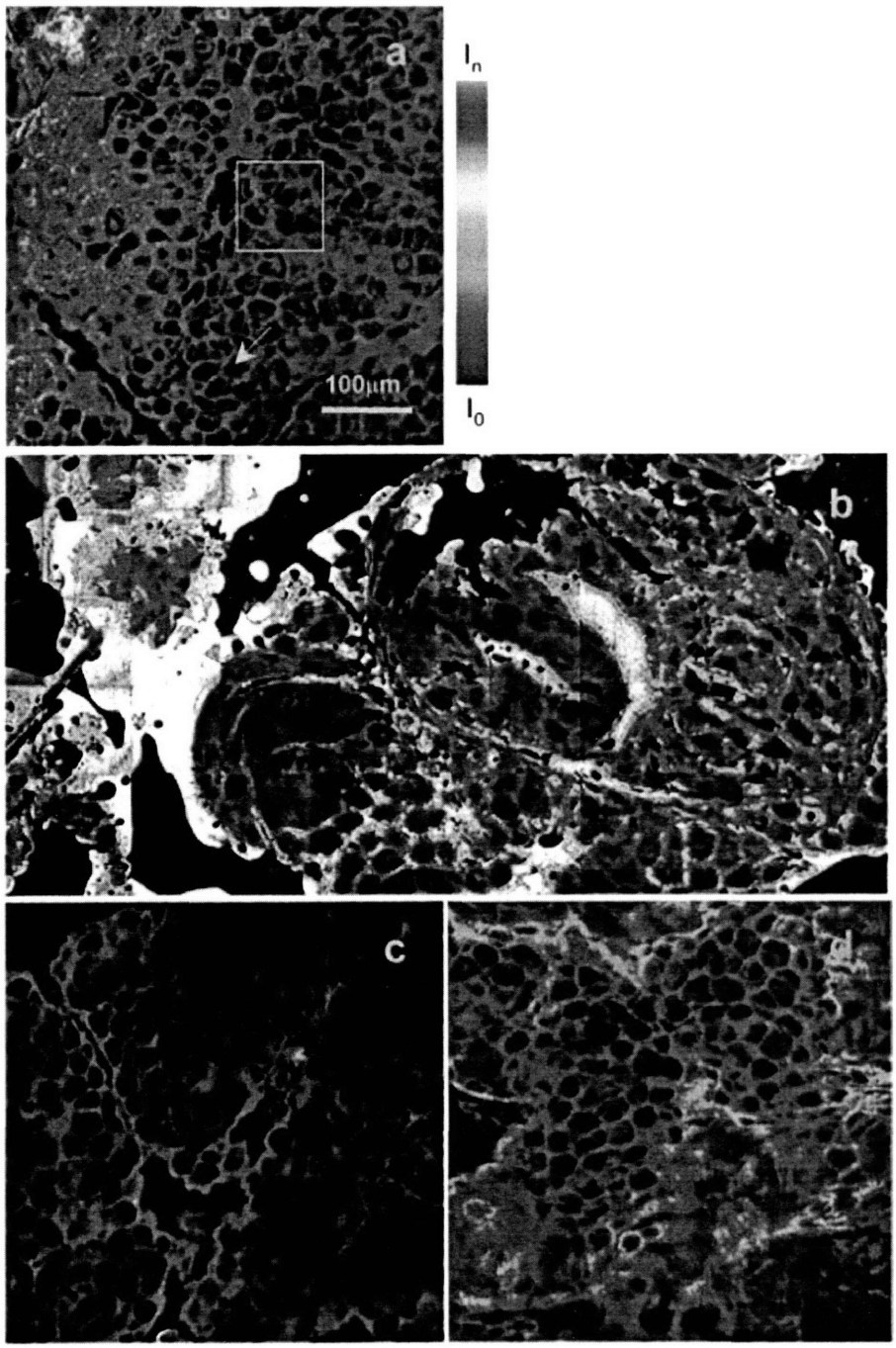

Fig. 2-8: Visualization of fluorescent probe spatial distribution in the skin. Selected regions from the 4 mm2 total skin area scanned are shown for (a) RBHE control, (b) RBHE oleic acid, (c) SRB control, and (d) SRB oleic acid cases of the probe distributions close to the skin surface. The arrow points to a circular dark region typical of stratum corneum corneocytes, whereas the intercorneocyte regions highlights in blue represent the lipid multilamellae. The box demarks the 100 μm × 100 μm area representing the field of view captured by a 40 × objective for one individual skin site.

2.3.3. Results

A Visualization of wide-area axial scans

For each skin sample, a selected fraction of the total 4 mm^2 skin area evaluated is shown in Fig. 2-8. Fig. 2-8(a - d) depict the spatial heterogeneity of probe distributions captured over a small portion of the total skin area imaged. The green box in Fig. 2-8(a) represents the area encompassed by one microscope field of view. For both RBHE and SRB, oleic-acid-induced increases in the probe partitioning into the stratum corneum are revealed by the increased intercellular probe intensities that are represented by the light blue regions. In addition to the increased probe distribution throughout the intercorneocyte regions, Fig. 2-8(b) illustrates an increase in the heterogeneity of the probe distribution, with regionalized areas of high probe concentration (regions in white).

In contrast to the similar probe intensity distributions observed in an overwhelming majority of the 400 skin sites scanned for the RBHE control (Fig. 2-8a), Fig. 2-8(c) illustrates the nonuniform spatial distribution of the hydrophilic probe SRB typical of the 2 mm × 2 mm area scanned. The black to dark blue colors marking the intercellular regions observed in Fig. 2-8(c) reflect the low skin permeabilities to hydrophilic permeants such SRB. In the presence of oleic acid, the overall increase in SRB skin penetration is accompanied by the appearance of distinct intercellular regions of higher probe concentrations that are highlighted in light blue (see Fig. 2-8d).

The wide-area axial scans presented in Fig. 2-8 unquestionably demonstrate the advantages of HTPM in efficiently increasing the sample area (100-fold) to provide a dramatically improved visualization of the range of variation in probe distributions over a clinically more relevant area of skin (2 mm × 2 mm). From these scans, the skin area represented by one field of view (100 μm × 100 μm) clearly does not validly capture the variability of the probe distributions over the 400 consecutive skin sites scanned.

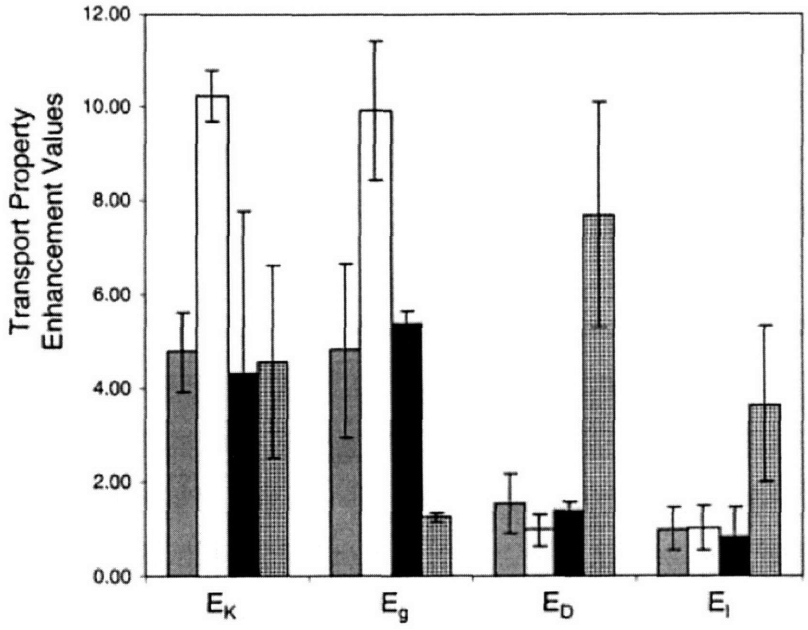

Fig. 2-9: Relative changes in oleic-acid-induced transport. Key: 400 skin site RBHE (gray bar), 400 skin site SRB (white bar), RBHE limited sample size (black bar), SRB limited sample size (checked bar). The wide-area values correspond to the transport enhancement values obtained in this study utilizing the data from the 400 skin sites scanned, whereas the limited sample size values reported by a literature which is based on 4-6 sites.

B Quantification of relative changes in transport properties

As shown in Fig. 2-9, the predominant effects of oleic acid action based on the 400-skin-site analysis for the hydrophilic (SRB) and the hydrophobic (RBHE) probes are the enhancements in the vehicle to skin partitioning (E_K = 4.77 ± 0.83 and 10.22 ± 0.55, respectively) and in the concentration gradient (E_g = 4.81 ± 1.86 and 9.93 ± 1.50, respectively). Good agreement exists for the hydrophobic probe E_K, E_g, E_D, and E_l values between the 400-skin-site study (Fig. 2-9, gray bars) and the previous four to six site study (Fig. 2-9, black bars). The changes in the transport properties for the hydrophilic probe, however, exhibit a high degree of variability between these two very different skin sample sizes. This can be seen by comparing the white bars in Fig. 2-9, which represent the 400-skin-site hydrophilic probe enhancement values, and the checkered bars in Fig. 2-9, which represent the four to six skin site enhancement values. Moreover, the hydrophilic four to six skin site E_l value of 3.66 ± 1.67 predicts an increase in the skin barrier thickness, suggesting that, in the presence of oleic acid, the primary transport

barrier extends beyond the stratum corneum layer. This E_l value deviates from unity and is inconsistent with the role of the stratum corneum as the primary barrier to transdermal transport.

2.3.4. Conclusion

High-speed two-photon microscopy was used for quantitative study of microscale property changes (change of transport properties with the action of chemical enhancer) even with the heterogeneous specimen (skin) by investigating large enough size of 2 mm × 2 mm. The difficulty in microscopic study of the skin properties is its inherent heterogeneity. Therefore, a large section of a few mm^2 needs to be investigated to get statistical study on the skin. High-speed two-photon microscopy has been successfully to skin study by doing 3D imaging of 2 mm × 2 mm section within 1.5 hours (with 50 layers). The change of microscale transport properties with the action of chemical enhancer was well quantified with small variance (20 %). The enhancement of drug transport is mainly due to both the vehicle to skin partition coefficient enhancement, E_K and the enhancement of intensity gradient, E_g (Yu et al. 2002; Yu et al. 2003).

2.4. Visualization of oleic acid-induced transdermal transport pathway

2.4.1. Introduction

The primary transport pathway through the skin is known to be intercellular lipid region and the role of corneocytes in transdermal transport has not been examined in depth (Matoltsy 1976). TPM can image SC structure based on its autofluorescence in addition to probe distribution (Masters et al. 1997; Masters et al. 1998). Therefore, it is possible to map the spatial distribution of probe with respect to SC structure in order to measure whether probes stay in the intercellular lipid region or diffuse into corneocytes. We can also monitor the change in the spatial distribution of probe with respect to SC structure which is induced with oleic acid.

SC is comprised of corneocytes which are wide (10 μm diameter) but very thin (0.8 μm thickness) (Bommannan et al. 1990). The thickness of corneocytes (~0.8 μm) is comparable than the resolution of TPM. Therefore, the images of inside corneocytes may contain the signal from below and above the corneocyte (outside). Therefore, we imaged specimens in 3D with a fine depth increment of 0.7 μm which is equivalent to the axial resolution of two-photon microscopy. Analysis of these image stacks in 3D minimizes imaging artifacts due to the finite resolution of the microscope. The distribution of both SC and probe was measured by doing two-photon 3D imaging with dual color channels. We chose fluorescent probes that have well separated emission spectra from the autofluorescence of the SC (Kollias et al. 1998; Gonzalez et al. 2000; Na et al. 2001; Yu et al. 2001). Therefore, two probe and SC signals can be easily separated each other. One channel collects signal from autofluorescence of SC which is in the blue/green spectral region, and the other channel collects signal from probe which is in the red spectral region.

A Skin sample preparation

The preparation procedure is the similar to the description in Section 2.2. The concentrations of hydrophobic and the hydrophilic probes, rhodamine B hexyl ester (RBHE) and sulforhodamine B (SRB) (Molecular Probes, Eugene, OR), were adjusted such that the exogenous fluorescent model drug intensity signal detected was comparable with the endogenous SC autofluorescence intensity. The dilution of the RBHE and SRB vehicles to 0.005 mg per ml (compared with the 0.33 mg per ml utilized in the studies reported previously; (Yu et al. 2001; Yu et al. 2002)) enables the simultaneous imaging of the skin autofluorescence as well as of the exogenous fluorescent model drug intensities, such that model drug signal saturation is avoided. After 24 h of skin exposure to the model drug solution, the samples were rinsed with PBS, and mounted on microscope slides.

B Two-photon imaging

Simultaneous imaging of SC structure and probe distribution was performed by splitting the emission light into two channels. Two channels were implemented by using the filter set (Chroma Technologies, Brattleboro, VT). The filter set consists of a dichroic mirror (part no. 530DCXR), a short pass filter (part no. E535SP), and a bandpass filter (part no. D630/40). The dichroic mirror reflects emission wavelengths below 530 nm from the SC to one channel using an additional short pass filter to further reject signal from the probes. Fluorescence emission signals from the probes at wavelength above 530 nm are transmitted through the dichroic mirror, purified using a bandpass filter, and are detected in the second channel. The first channel containing SC autofluorescence information will be referred to as the green channel. The second channel, or the red channel, detects the model drug fluorescence signal. The model drug spatial distributions in the following studies were evaluated in nine consecutive skin sites, each skin site having an area of 100 μm by 100 μm. At the laser power used, the skin autofluorescence intensities treated with the control and the enhancer vehicle solutions in the presence and in the absence of the model drugs are comparable. This comparison of the skin autofluorescence intensities verifies that the skin autofluorescence signal detected in the

green channel arises from the endogenous skin fluorophores, and not from signal noise introduced by the model drugs.

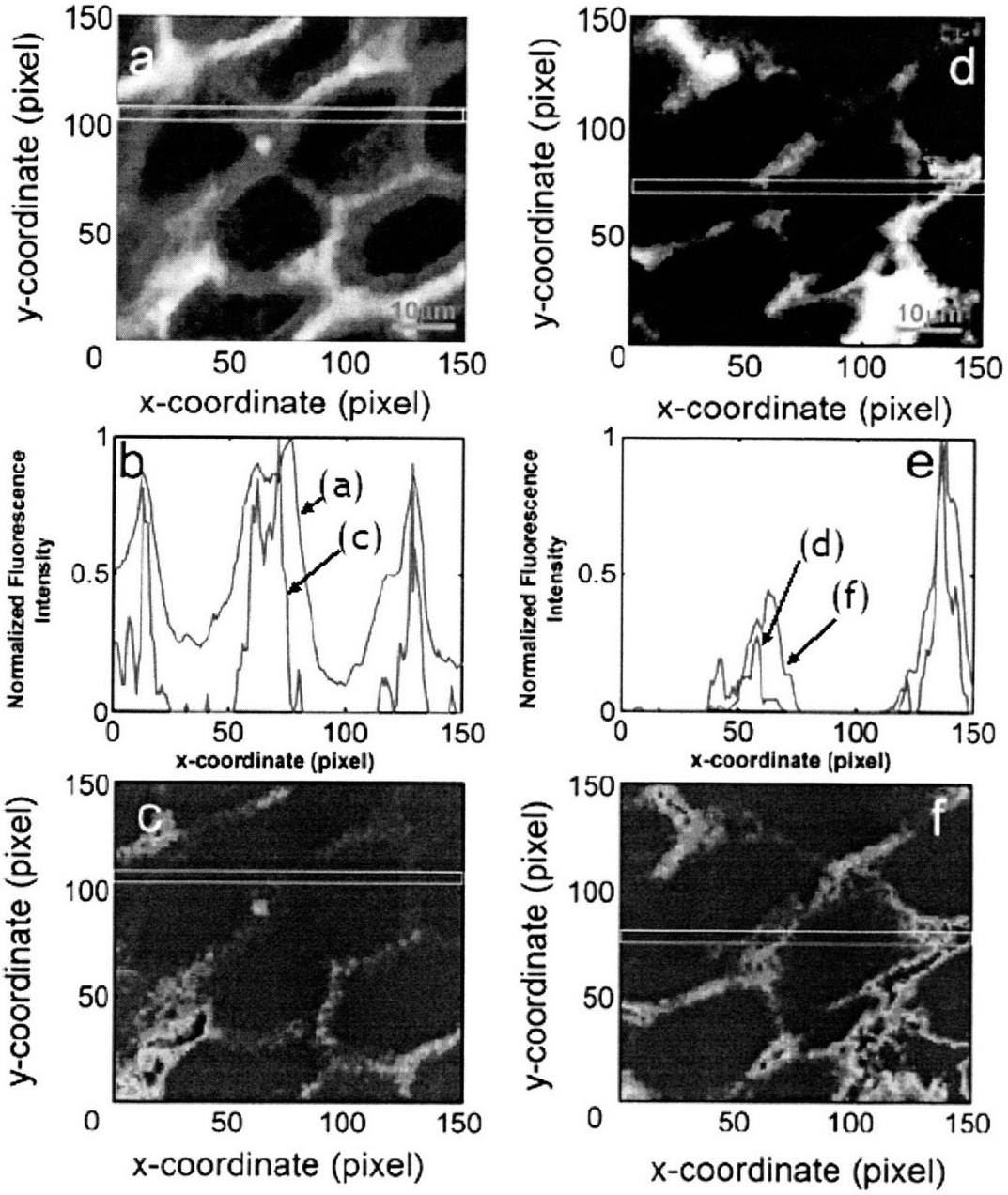

Fig. 2-10: Intensity profile analysis of the hydrophobic model drug (RBHE). For the control case, the image of the RBHE model drug spatial distribution, shown in (a), the image of the corresponding skin autofluorescence signal, shown in (c), and the intensity profile of the cross section marked in the images in (b). For the chemical enhancer case, the image of the model drug, shown in (d), the one of the skin autofluorescence in (f), and the intensity profiles in the marked cross section are shown in (e)

C Data Analysis

The probe intensity distribution with respect to SC structure is analyzed for RBHE-control and RBHE-enhancer in Fig. 2-10, and SRB-control, SRB-enhancer in Fig. 2-11. The figures shows distinctive structure of SC and is comprised of 150 × 150 pixels. In each figure, (a)-(c) are for control case and (d)-(f) are for enhancement case. (a) and (c) show the image from the red channel (probe distribution) and the one from green channel (SC structure). The intensity profiles of a cross section marked in (a) and (c) are shown in (b). These profiles show the distribution of probe with respect to SC structure. For enhancement case, dual channel images are shown in (d) and (f) and the intensity profiles at the cross section are shown in (e).

Discussion: Hydrophobic model drug (RBHE)

For the RBHE-control in Fig. 2-10(b), the model drug intensity spectrum (line A) envelopes the autofluorescence spectrum (line B). The wider model drug intensity spectrum peaks, relative to the referenced peak widths of the corresponding autofluorescence spectrum, indicates that the model drug transport extends beyond the intercellular region defined by the skin autofluorescence intensity spectrum and into the corneocyte structures. Compared with the zero intensity minima exhibited by the skin autofluorescence spectrum, the model drug intensity spectrum minima never approach zero. The model drug intensities detected within the corneocyte regions further corroborate the existence of intracorneocyte model drug penetration potentially driven by the model drug concentration gradient from the intercellular region into the corneocyte region. In the presence of oleic acid, however, RBHE becomes more localized to within the defined intercellular space. The intensity spectra shown in Fig. 2-10(e) indicate that the widths of the autofluorescence intensity peaks (located at x = 60 pixels and at x = 140 pixels) extend beyond the corresponding peak widths for the model drug intensity spectrum.

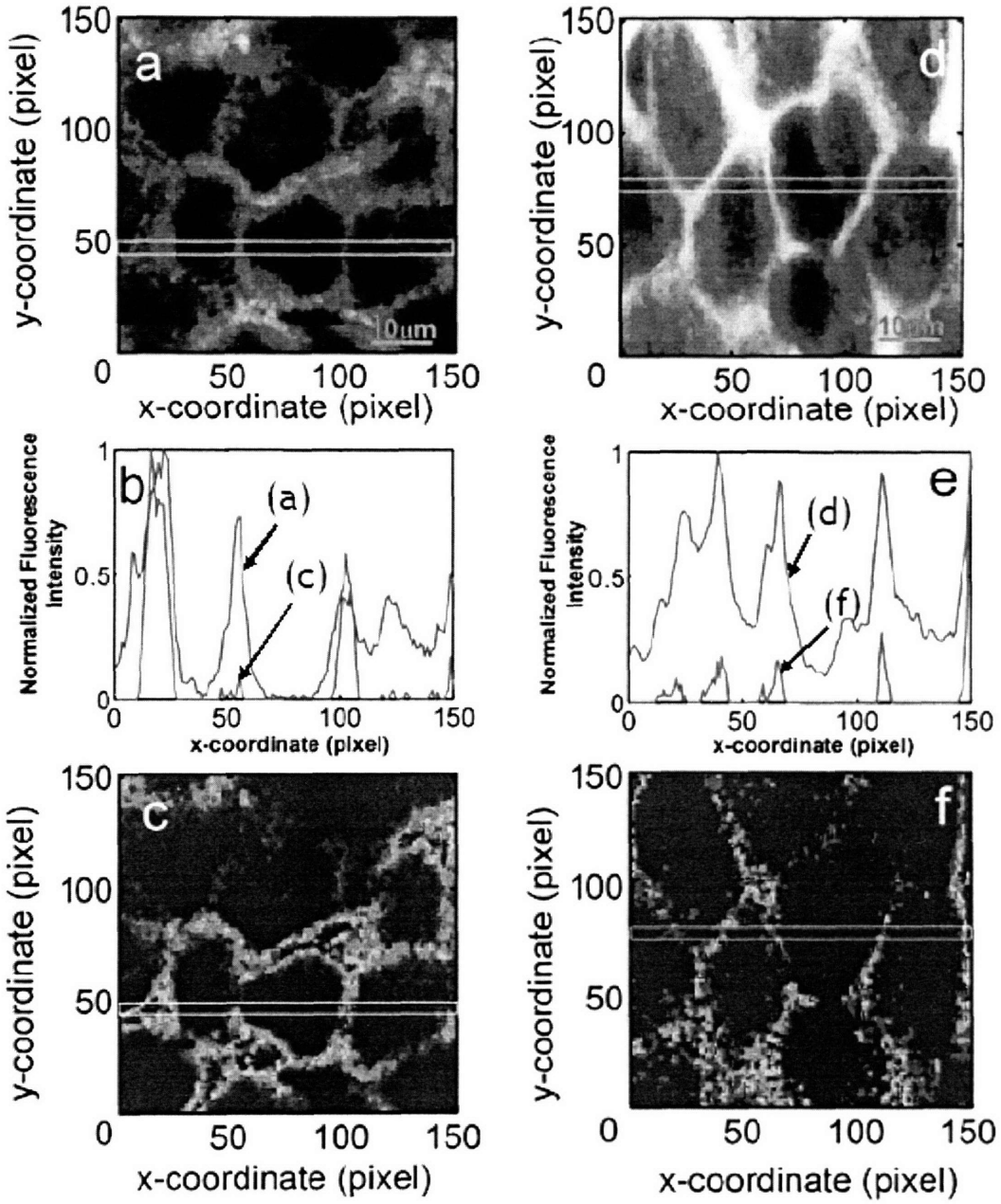

Fig. 2-11: Intensity profile analysis of the hydrophobic model drug (RBHE). For the control case, the image of the RBHE model drug spatial distribution, shown in (a), the image of the corresponding skin autofluorescence signal, shown in (c), and the intensity profile of the cross section marked in the images in (b). For the chemical enhancer case, the image of the model drug, shown in (d), the one of the skin autofluorescence in (f), and the intensity profiles in the marked cross section are shown in (e)

Discussion: Hydrophilic model drug (SRB)

Fig. 2-11(b) shows the SRB-control sample intensity spectrum (line A) at the cross section in Fig. 2(a), and the autofluorescence spectrum (line B) in Fig. 2(c). In Fig. 2(b), the SRB- control autofluorescence spectrum (line B) exhibits two major peaks at x = 21 pixels and at x = 103 pixels, with minor peaks at x = 56 pixels and at x = 150 pixels. These four peaks correspond to the positions of the intercellular regions marked by the peaks of autofluoresnce signal (Fig. 2-11c). The SRB model drug intensity spectrum peak widths are greater than those corresponding to the skin autofluorescence peaks at the four x-coordinates noted. This difference between the model drug intensity and the skin autofluorescence peak widths indicates that the model drug does penetrate into the corneocyte region, although not to the same extent as for the SRB-enhancer case (described below). The minima corresponding to the SRB control intensity spectrum in Fig. 2-11(b) do reach the zero intensity value as the spatial position approaches the corneocyte center and away from the intercellular region. The additional peak detected only for the model drug intensity at x = 120 pixels provides evidence of model drug penetration into the corneocyte region. The peak to peak region of the autofluorescence spectrum from x = 103 to 150 pixels outlines the outer bounds of a corneocyte. The model drug intensity peak at x = 120 pixels, as well as the nonzero model drug intensities detected within the corresponding corneocyte region, indicate model drug penetration within this corneocyte region. Compared with the differences between the hydrophobic model drug peak widths and their corresponding autofluorescence peak widths, the hydrophilic model drug control case displays less intracorneocyte diffusion. The oleic acid-induced increase in the penetration of the hydrophilic model drug (SRB) into the corneocyte region is observed in the spectra shown in Fig. 2-11(e), in which the model drug peak widths far exceed the autofluorescence peak widths that outline the boundary of the intercellular region. The oleic acid-induced increased partitioning of SRB into the SC intercellular region, which was quantified previously, increases the model drug concentration in the intercellular region. The drop in model drug intensity about the peak maximum reflects the concentration gradient driving SRB diffusion into the corneocytes. In contrast to its effect on the hydrophobic model drug localization to the intercellular region, the increased concentration of SRB in the intercellular region contributes to the

oleic acid-induced intracorneocyte penetration observed in Fig. 2-11(d), where the model drug intensity does not drop to zero in the corneocyte regions.

2.4.2. Conclusion

Based on the visual elucidation of transport pathways through the decomposition of the skin autofluorescence signals from the model drug fluorescence signal, oleic acid was observed to increase intracorneocyte penetration for the hydrophilic model drug and to localize hydrophobic model drug diffusion to either the intercellular region (Yu et al. 2003).

2.5. Tumor physiology study: microvasculature and leukocyte-endothelial interactions.

2.5.1. Introduction

Two-photon microscopy is widely used for in-vivo deep tissue imaging due to its greater penetration depth and lower phototoxicity (Centonze et al. 1998; Mohler et al. 1998; Mohler et al. 1998; Squirrell et al. 1999). In vivo physiological and pathphysiological studies at both the tissue and cellular levels are feasible in animal model (Jain et al. 2001). In collaboration with Dr. Tim Padera, Dr. Brian Stoll, and Prof. Rakesh Jain in Massachusetts General Hospital, we studied blood vessel and lymphatic structures in solid tumors (Padera et al. 2002). Angiogenesis is an important mechanism during tumor growth because tumors can not grow beyond a certain size without inducing the growth of blood vessels to increase the supply of nutrients and oxygen (Leunig et al. 1992). An understanding of how blood vessels in tumors are different from the ones in normal tissue is important. We applied two-photon microscopy to image blood vessels down to 300 μm deep from surface. The response of immune system to tumor can be further studied by quantifying the interaction of leukocyte and the blood vessel endothelium. HSTPM was used to monitor the rolling motion of leukocytes by imaging the flow of blood vessels located inside a solid tumor in real time (Kim et al. 1999).

A Animal model : dorsal skin-fold chamber

The preparation of dorsal skin-fold chamber can be found in the literature (Leunig et al. 1992). The back of a mouse was shaven and depilated and two mirror-image frames were mounted so as to fix the extended double layer of skin between the frames. One 15-mm-diameter layer of skin was excised leaving the striated muscle, subcutaneous tissue, and epidermis of the opposite side. The tissue was covered with a glass cover slip. Some chambers were implanted with different kinds of tumors to study their physiology.

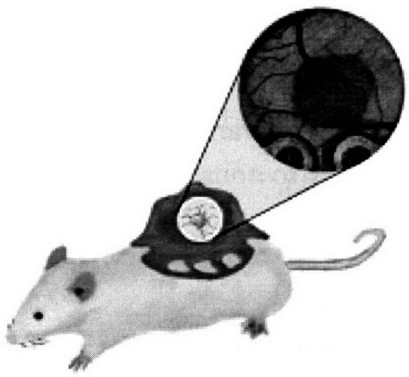

Fig. 2-12: Mice bearing dorsal skin-fold chamber.

B Imaging of tumor vasculature

We applied two-photon microscopy to image blood vessels in solid tumors in-vivo. The specimens were mouse dorsal-skin chambers. One chamber was implanted with T-241 fibrosarcoma to image tumor vasculature. Prior to imaging, the animal was anesthetized and given a 0.1-ml intravenous injection of 2.5 % 2×10^6 MW FITC-dextran (Molecular Probes, Eugene, OR) by tail vein cannulation for vascular density measurement. For imaging, the animal was fixed to a metal plate designed to stabilize the chamber.

Two-photon 3D imaging was performed in the imaging depth of up to 300 μm. The objective used is 25 × (LCI Plan-Neofluar 25×, NA 0.8, Zeiss, Thornwood, NY) with 200 μm × 200 μm image size. The input power was 100 mW. The frame rate is approximately 0.3 frames/s with 256 × 256 pixel images.

The images of vasculatures are presented in Fig. 2-13. The images from normal tissues are in (a), (b), (c) and the ones from solid tumors are in (d),(e), and (f). (a) and (d) is surface images acquired with epifluorescence microscopy. (b), (c) are 3D reconstructed image at 300 μm deep from normal tissue and (e), (f) are the one from solid tumors. Different from the ones from normal tissue, blood vessels from solid tumors exhibited higher density and tortuosity. The 3D images, obtained with two-photon microscopy, were used to calculate vascular volume fraction. The ratio of vessel volume to tissue volume in tumor tissues was 0.199 compared to 0.098 in normal tissue. This

quantification can be used to measure the effectiveness of various antiangiogenic agents as potential cancer treatments. Such an approach may prove invaluable for studying and accurately assessing the effectiveness of various antiangiogenic agents as potential cancer treatments (Jain 1999; Jain et al. 2001).

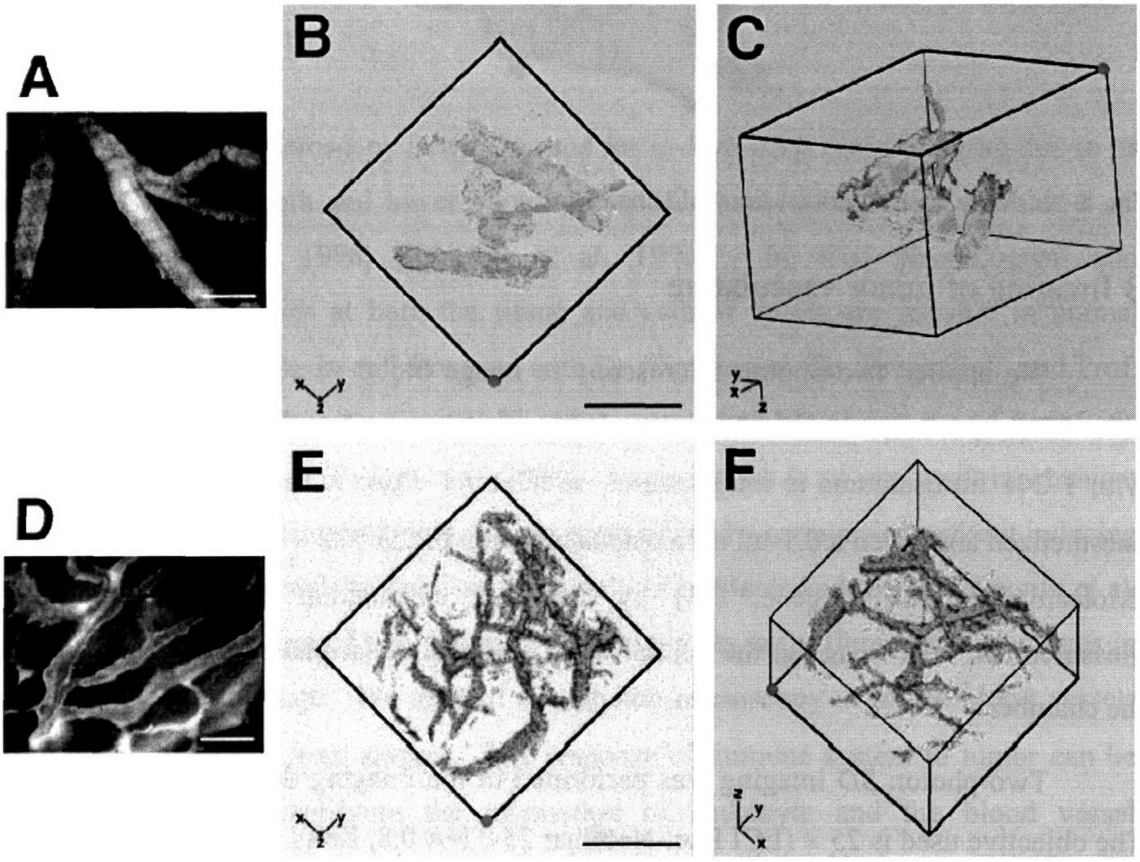

Fig. 2-13: Images of non-tumor-(A, B, C) and tumor-bearing mouse dorsal skin-(D, E, F). (A) Epifluorescence image of non-tumor-bearing dorsal skin shows normal vessel density and tortuosity. (B, C) two-photon images of non-tumor-bearing dorsal skin also show normal vessel density and tortuosity at the depth of 200 μm. The image shown in (B) represents the view looking down into the dorsal chamber from the surface of the chamber. The image in (C) is a 3D representation obtained by rotating the image in (B). The images were obtained using a 20 × objective and an imaging depth up to 300 μm. On the other hand, the images from tumor-bearing mouse dorsal skin shows high vessel density and tortured vascular structure.

C Monitoring leukocyte-endothelium (L-E) interaction

As the second experiment monitoring the physiology of tumor tissue, we monitored the blood flow in the vessels of tumor tissues with the high-speed two-photon

microscope. The specimens were mouse dorsal-fold chambers in which BA-HAN-1C rhabdomyosarcoma was implanted to monitor leukocyte–endothelium (L-E) interactions. Prior to imaging, the animal was anesthetized and given a 0.05 ml intravenous injection of 0.1% rhodamine 6-G (Sigma) for visualization of L-E interaction.

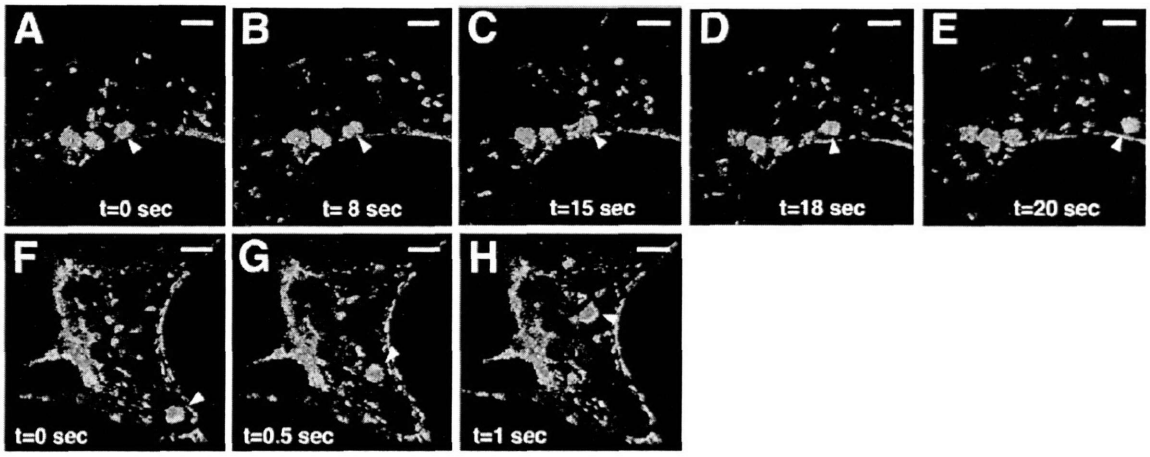

Fig. 2-14: Time sequence of images acquired using high-speed two-photon microscope showing L-E interaction in the dorsal skin-fold chamber. (A-E) Vessel in a non-tumor bearing chamber imaged at a depth of 150 μm below chamber window. The elapsed times are shown. The arrowhead follow a single leukocyte that had adhered to the vessel wall (A, B), released (C), and rolled along the vessel wall (D, E). (F-H) Vessel in BA-HAN-1C rhabdomyosarcoma growing in a dorsal skinfold chamber imaged at a depth of 200 μm below the chamber window. The elapsed times are shown. The arrowhead follows a single leukocyte traveling with the blood flow, not interacting with the vessel wall. The blood flow has an average velocity of 220·μm/sec. All scale bars represent 40 μ·m.

A 10 x objective was used. The imaging depth was approximately 150 μm below the surface. The frame rate was 13 frames per second with image size of 400 μm × 400 μm. A time lapse sequence of images is shown in Fig. 2-14. In the first time lapse image, a few leukocytes are attached on the wall. One flowing leukocyte is shown in the second time lapse.

The response of immune system to rhabdomyosarcoma was monitored by measuring the flux of leukocytes (16.4 ± 1.8 cells per 30 s) and the percentage of rolling cells (20.5 ± 6.5 % from 6 vessels of two animals). These quantities were not different from the case of normal tissues. This result indicates that the immune system does not response to the existence of rhabdomyosarcoma, because it does not produce cytokines

which stimulate endothelium. However, this scheme will be advantageous to find conditions of immune system response to tumors.

2.5.2. Conclusion

The combination of two-photon microscopy with animal models has excellent potential for the study of physiology. The capability of accessing cellular, tissue-level events in vivo can be used in understanding tumor angiogenesis and immune system reactions. We applied two-photon microscopy to image the tumor vasculature 300 μm deep from surface and found that tumor vessels are densely distributed and tortuous. Further, we applied high-speed two-photon microscope to monitor the L-E interaction in blood vessels of tumors (Padera et al. 2002).

Chapter 3

Multifocal multiphoton microscope based on multi-anode photomultiplier tube (MAPMT)

Multifocal multiphoton microscopy (MMM) is a new form of TPM with significantly improved data acquisition speed by parallelizing the imaging process. However, the suitability of MMM for imaging of thick tissue is in question because its sensitivity to the scattering of emission photons. The scattering of emission photons can affect images in terms of both resolution and contrast. In this chapter, we performed the first quantitative measurement of the effect of specimen scattering coefficient on emission photon point spread function (PSF) (Section 3.1). Based on the PSF measurement result, a new MMM system was designed for turbid tissue imaging based on the use of multi-anode photomultiplier tube (Section 3.2). Its performance is presented and is compared with the conventional CCD-based MMM. As an application, this system forms the basis of a 3D tissue cytometer that has been used for the systematic quantification of cellular and extracellular matrix states in tissues (Section 3.3).

3.1. Implications of tissue turbidity in MMM

3.1.1. Introduction

HSTPM is important to study cellular kinetic events such as calcium signaling, to sample a statistically significant volume of biological specimen as in characterizing transdermal drug delivery pathways (Yu et al. 2002), and to avoid physiological motion in clinical diagnostic applications. A number of designs have been developed to achieve the high frame rate in multiphoton microscopy (Bewersdorf et al. 1998; Buist et al. 1998; Fan et al. 1999; Kim et al. 1999). One of the most exciting approaches is multifocal multiphoton microscopy (MMM) (Bewersdorf et al. 1998; Buist et al. 1998) that achieves

a high frame rate by parallelizing the imaging process. In this configuration, a specimen is scanned with multiple excitation foci instead of a single focus of excitation light. The imaging speed is increased by the number of excitation foci with which the specimen is scanned. The emission photons generated from the foci are collected simultaneously at a spatially resolved multi-channel detector such as a charge coupled device (CCD) camera. In general, higher imaging speed can be achieved by using higher input power. However, this approach is limited since fluorescence generation can be saturated due to the finite lifetimes of fluorophores. In general, the fluorophores can only be cycled at rates less than the inverse of their lifetimes that are typically less than 100 MHz. The saturation level of input laser is dependent on the excitation cross section of the fluorophores and the optics and laser parameters and is typically less than 10 mW with typical fluorophores and objectives. Excitation at power level beyond saturation will results in the broadening the excitation point spread function lowering the resolution of the microscope. Scanning with multiple excitation foci has an advantage that imaging speed is increased, while the input power per focus can be kept within the saturation limit.

Although MMM is very effective for high speed imaging in thinner specimens, it is questionable whether it can achieve similar tissue imaging depth as in conventional TPM (also referred to as single focus multiphoton microscopy, SMM). This report aims to quantify this important factor. MMM imaging is sensitive to the variations in emission point spread function (PSF_{em}) due to emission photon scattering, which is different from TPM. The point spread functions (PSF_{tot}'s) of two systems (MMM and SMM) are different and can be expressed as: Equation Chapter 3 Section 1

$$\begin{aligned} PSF_{tot}^{MMM}(x_i, y_i, z_s) &= PSF_{em}(x_i, y_i, z_i = z_s) \iint PSF_{ex}(x_s, y_s, z_s) dx_s dy_s \\ PSF_{tot}^{SMM}(x_s, y_s, z_s) &= PSF_{ex}(x_s, y_s, z_s) \iint PSF_{em}(x_i, y_i, z_i = 0) dx_i dy_i \end{aligned} \tag{3-1}$$

PSF_{ex} and PSF_{em} are the intensity point spread functions of excitation light and emission light respectively. (x_s, y_s, z_s) is the coordinate in the sample plane (volume) and (x_i, y_i, z_i) is the coordinate in the image plane (volume). It is assumed that the image plane is telecentric to the sample plane with a magnification of one. In the PSF_{tot} of SMM, PSF_{em} is integrated over the detection area of a detector and the microscope spatial

response is only determined by PSF_{ex}. Physically, the detector collects all the emission photons reaching its detection area without any spatial information. In this configuration, a single focus of excitation light is generated in a specimen for two-photon excitation and the specimen is raster-scanned. An image is formed by the temporal encoding of the integrated signal with the known raster scanning pattern. For MMM imaging, the spatially resolved detector accumulates emission photons from a specimen during the scanning time of one frame. In the PSF_{tot} of MMM, PSF_{ex} is integrated over the scanning area and it is PSF_{em} that determines the spatial response of the microscope in the transverse plane and the product of PSF_{em} and PSF_{ex} in the axial direction. Therefore, image qualities like resolution and contrast are sensitive to the variation in PSF_{em} in the case of MMM.

The effect of photon scattering on image resolution and contrast in multiphoton microscopy has been investigated extensively with both Monte Carlo simulations (Blanca et al. 1998; Gan et al. 2000) and experiments (Ying et al. 1999; Dunn et al. 2000; Oheim et al. 2001; Beaurepaire et al. 2002; Dong et al. 2003). The previous studies have been based on SMM. Therefore, they focused on the scattering effect on PSF_{ex} (Blanca et al. 1998; Ying et al. 1999; Dunn et al. 2000; Gan et al. 2000; Dong et al. 2003) and the collection efficiency of the integrated emission photons (Dunn et al. 2000; Oheim et al. 2001; Beaurepaire et al. 2002) rather than the variation in PSF_{em} profile. The result of these studies can be summarized as: (1) the generation of two-photon fluorescence is contributed by only unscattered ballistic photons up to a few times of l_{ex}^{s}, because the quadratic dependence of two-photon fluorescence on excitation photon flux suppresses the contribution of the scattered excitation photons which are broadly distributed around the focus region. Therefore, the amount of two-photon fluorescence generated at the focus located at depth z, F(z), decays as:

$$F(z) \propto \exp(-2z/l_{ex}^{s}) \tag{3-2}$$

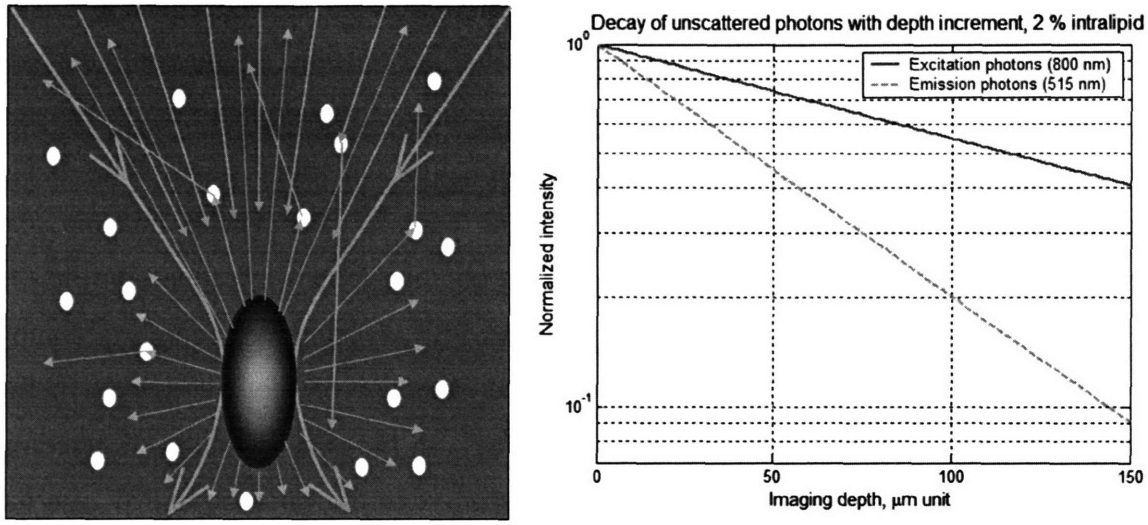

Fig. 3-1: Cartoon of photon scattering around two-photon excitation focus (a) excitation photon scattering reduces the amount of excitation photons arriving at the focus. Emission photons are also scattered before they are collected by detection optics and detectors. (b) Decay of unscattered photons with the increment of imaging depth in case of 2 % intralipid. Its mean free path length is 62.5 μm, 167 μm at emission (515 nm), excitation wavelength (800) respectively. It is noted that more scattering occurs to the shorter wavelength light (emission light).

Where l_{ex}^{s} is mean free path length at excitation wavelength. (2) Image resolution is not degraded due to scattering up to the depth of a few times of l_{ex}^{s}, because the FWHM of the PSF_{ex} is not affected. (3) For the same reason, image contrast is not degraded except due to shot noise limit. (4) The collection efficiency of emission photons can be maximized by enlarging the collection solid angle of the microscope system including the use of a high numerical aperture objective with a large field, large intermediate optical elements with large collection angles and a large area detector (Oheim et al. 2001).

The effect of photon scattering on PSF_{em} has not been studied because the SMM is not sensitive to its variations. However, it is important for MMM deep tissue imaging, because PSF_{em} is the primary factor in determining the shape of MMM PSF_{tot}. Importantly, tissue scattering may induce more variations in PSF_{em} than in PSF_{ex}, because PSF_{em} is linearly related with emission photon flux. This sensitivity of PSF_{em} on scattering effect is further compound by the fact that the emission photons in the

multiphoton microscope have shorter wavelengths than the excitation wavelength and have shorter mean free paths.

We quantify the scattering effect on PSF_{em} by measuring the PSF_{em} as a function of scattering length. From the PSF_{em} profile, we can deduce its full width at half maximum intensity (FWHM), the decay of its peak intensity, and the ratio of unscattered vs. scattered photon contributions. PSF_{em} FWHM provides the information about the scattering effect on image resolution. The decay of PSF_{em} peak intensity with the increase of scattering length represents the scattering effect on signal level. The ratio of unscattered vs. scattered photon intensity can quantify the scattering effect on image contrast.

3.1.2. Results and Discussion

A Resolution variation due to emission photon scattering

The effect of photon scattering on PSF_{em} can be obtained by measuring the PSF_{tot} of MMM (PSF_{tot}^{mmm}), because PSF_{tot}^{mmm} profile is mainly determined by PSF_{em} and the variations in PSF_{ex} due to photon scattering is well known. In order to measure the effect of emission photon scattering on image resolution, the variations in PSF_{tot}^{mmm} FWHM was acquired by the 3D imaging of a small fluorescent microsphere of 0.22 μm diameter as the point source (F8811, Molecular Probes, Eugene, OR) with a CCD camera (Pentamax, Princeton Instrument, Trenton, NJ). The specimen was a 3D block of sparsely distributed fluorescent latex microspheres which were immobilized in a media containing 2 % agarose gel (UltraPure Low Melting Point Argarose, Invitrogen, Carlsbad, CA). Intralipid emulsion (Liposyn III, Abbott Laboratories, North Chicago, IL) was added as scatterer at various concentrations of 0.5 %, 1 %, and 2 %. The scattering properties of its 2 % concentration are similar to the properties of typical biological tissue.

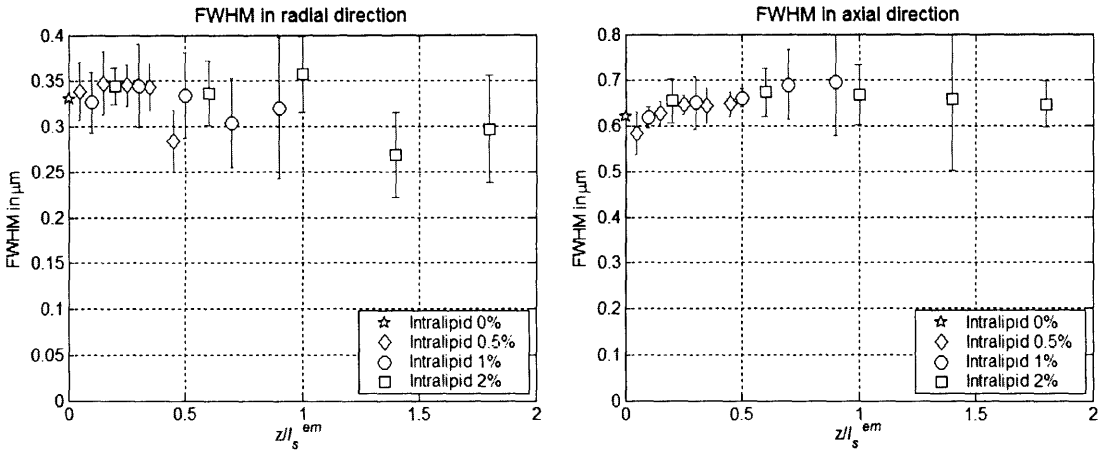

Fig. 3-2: Variations in PSF FWHM of MMM. FWHMs in transverse direction (a) and axial direction (b) are measured up to 2 times of mean free path length (l_{em}^{s} =62.5 μm) at emission wavelength (515 nm). There is no significant change in both transverse and axial directions. Objective used is 40 × with 1.2 NA. Input power level is approximately 5 – 10 mW at specimens. Acquisition time is 6.6 s per frame.

We measured the variation in PSF_{tot}^{MMM} FWHM as a function of imaging depth by imaging the specimens from the surface down to 125 μm deep at each scatterer concentration. The objective used in the experiment was 40 × water immersion with NA 1.2 (C-Apochromat 40x W Korr, Zeiss, Thornwood, NY). Each image had the field of view of 25 μm × 25 μm with 256 × 256 pixels. Therefore, the spatial resolution in the transverse direction was 0.1 μm. The total depth was subdivided into 5 sections each of which was 25 μm thick. For each section, images of 100 layers were acquired with axial resolution of 0.15 μm. The acquisition time was approximately 6.5 seconds per frame. Average values of PSF_{tot}^{mmm} FWHM for each section were obtained from at least 10 microspheres in each section. The imaging depth of various scatterer concentrations was normalized with l_{em}^{s} of 2 % scatterer concentration. Since the optical properties of intralipid emulsion vary depending on stocks, we measured them by using the multidistance frequency-domain method in collaboration with Prof. Fantini of the Department of Electrical Engineering and the Department of Bioengineering in Tufts University (Fantini et al. 1994). The reduced scattering coefficient, μ_s' was obtained in terms of the amplitude and the phase slopes versus source detector separation. The mean

free path length, l_s was obtained by assuming that it has the same anisotropy (g) as literature, $l_s = (1-g)/\mu_s'$. The optical properties of 2 % intralipid emulsion were similar to the literature(Dunn et al. 2000), (l_{ex}^s=167 μm, l_{em}^s=62.5 μm). The measurement of PSF_{tot}^{MMM} FWHM variations with the increment of imaging depth is presented in Fig. 3-2. The theoretical FWHMs are 0.26 μm, 0.56 μm in transverse and axial directions respectively with the finite size of the latex sphere taken into account. In the sample of 0 % scatterer concentration, the measured values are within 30 % of theoretical values demonstrating that the microscope system behaves theoretically. The measurement shows no significant change of PSF_{tot}^{MMM} FWHM in either transverse or axial direction for higher scatterer concentrations. Since PSF_{ex} is not changed due to scattering, this result allows us to conclude that the scattering of emission photons doesn't affect the imaging resolution up to the imaging depth of 2 l_{em}^s for MMM imaging.

B Signal decay due to photon scattering

The quantification of PSF_{em} peak intensity decay and the scattered photon distribution are more conveniently performed in a fluorescent dye solution mixed with intralipid emulsion as scatterer. The fluorescent dye solution was 233 μM fluorescein (F1300, Molecular Probes, Eugene, OR) dissolved in water and its pH was adjusted to 8.0 with sodium hydroxide. To measure PSF_{em} peak intensity decay, excitation light was focused into the solution to generate multi-photon fluorescence at its focus and the emission photons were collected by the CCD camera (Pentamax, Princeton Instrument, Trenton, NJ). The acquired image is a convolution of the PSF_{ex} and the PSF_{em}, $PSF_{tot}=PSF_{ex} \otimes PSF_{em}$. Since the scattering effect on PSF_{ex} is well known, the effect on PSF_{em} can be easily extracted. The decay of peak intensity was measured as the focus of excitation light moves into the specimen from the surface. The emission photons, collected only at the correct pixels, were considered as the signal whereas the emission photons, collected at the incorrect pixels due to scattering, were counted as background. With the magnification of 40 ×, each pixel of the CCD camera covered the area of 0.56 μm × 0.56 μm in the sample plane. The signal decay was also measured with a PMT for

the comparison with the one acquired with the CCD camera. The signal acquired with the PMT is considered as the maximum signal available for detectors, because the PMT collects all the emission photon arriving at its large detection area. The normalized decay curves are presented in Fig. 3-3(a).

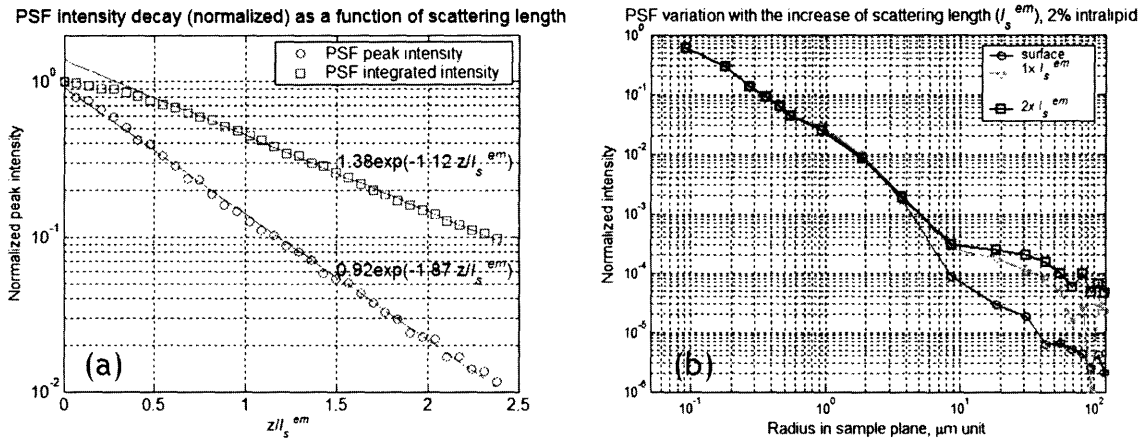

Fig. 3-3: Intensity decay with the increase of scattering length (a): peak intensity of PSF and PSF intensity integrated over the image plane. Peak intensity decays faster than the integrated intensity due to emission photon scattering. Variations in PSF profiles with the increase of scattering length (b): PSF is measured up to 100 μm radius from peak location. Intensity in the tail of PSF (> 25 μm) is monitored to increase due to scattering of emission photons.

The signals collected by both the PMT and the CCD camera both decay exponentially, $I(z) = \exp(-c\,z/l_{em}^{s})$. The signal collected with the PMT decays slower with decay coefficient, c as 1.04, compared with the one from the CCD whose coefficient, c is 1.87. This difference is expected, because the PMT collects more scattered emission photons than the CCD camera. Therefore, the difference between two signals can be considered as an additional signal loss specific to MMM. The signal decay is the combined effect of both excitation and emission photon scattering. It is known that only ballistic unscattered excitation photons contribute to the generation of fluorescence. The signal decay due to excitation photons only is $I_{ex}(z) = \exp(-0.75\,z/l_{em}^{s})$, $[=\exp(-2\,z/l_{ex}^{s})]$ in this configuration (excitation light at 800 nm and emission light at 515 nm). The difference in decay slope is the difference in the collection efficiency of emission photons. The decay constant of the signal, c of 1.87 is equivalent to the case when only unscattered ballistic emission photons are assumed to be collected as signal. In case of the signal

from the PMT, the decay constant due to emission photon scattering is approximately 0.29 which is significant smaller than 1.12 for the CCD case. Specifically, at a depth of two emission scattering length, the CCD signal is almost an order of magnitude below that of the PMT signal.

Emission PSF contains a broad scattered emission photon contribution

Since the peak signal intensity decreases as a function of scattering length while the PSF_{em} FWHM shows no significant scattering dependence, the scattered photons must have a broad distribution and a small intensity relative to central unscattered photon peak. This distribution has not been previously measured experimentally due to its low amplitude. In principle, the CCD image of the two-photon induced fluorescence focus contains this information. However, the relatively lower SNR of the CCD signal precludes a direct measurement. The measurement configuration instead utilized a higher SNR PMT detector placed behind a pinhole aperture placed in the image plane. A series of pinhole aperture with sizes ranging from 0.7 μm to 100 μm in radius in the sample plane were used with the resolution of about 2 - 10 μm (PxxS, SM1D12R, Thorlabs, Newton, NJ). In this configuration, we measured the integrated intensity deposited within a specific radius from the center of the PSF_{tot}. The mathematical relationship between the PSF_{tot} and this radially integrated intensity profile, $I(r_o,z)$ is

$$I(r_o,z) = \int_{r=0}^{r=r_o} PSF_{tot}(r,z)\, dA \tag{3-3}$$

The normalized PSF_{tot} at various depths with 2 % scatterer concentration are presented in Fig. 3-3(b). Within the resolution of this measurement, the PSF_{tot} profiles in the solutions with different scatterer concentrations were similar up to 2 μm radius which is approximately 10 times the PSF_{em} FWHM. However, the amplitude of PSF_{tot} in the range of more than 2 μm in radius was observed to increase with increasing scattering length. Since the variation in PSF_{ex} due to scattering is negligible, this spatially broad, low amplitude intensity distribution is composed of scattered emission photons. FWHM of the additional PSF_{tot} is approximately 40 μm at the depth of $2\times l_{em}^{s}$ which is 100 times larger than FWHM of PSF_{tot} and it increases roughly linearly with scattering length. This result indicates that the scattered emission photons are distributed spatially in more than

100 times of PSF_{em} FWHM. The wide distribution of scattered photons implies that most of scattered emission photons become background noise by being collected at the incorrect pixels. In MMM, scattering of emission photons degrades image contrast in two ways: (1) signal is reduced very fast because scattered emission photons are not collected in the appropriate pixels. (2) Background noise is also decreased but not as fast as the decay of signal with the contribution of scattered emission photons. Using the measured PSF_{tot}, the effect of contrast reduction can be clearly observed in a numerical simulation (Fig. 3-4).

The original image is an array of 10 μm diameter circles which are separated by 40 μm each other. The measured PSF_{tot} as a function of scattering length is applied to the original image by convolution. Fig. 3-4(a), (b) are images on the surface and 150 μm ($2.4 \times l_{em}^{s}$) deep from the surface respectively. The deterioration of image contrast is clearly seen in Fig. 3-4(b). It is noted that the background around the center circle has higher intensity than that around the circle in the corners. This is because the center background region accumulates scattered signals from the surrounding circles. The contribution of background intensity (I_{BG}) to SNR is plotted compared with the SNR of signal only (due to signal fluctuation) in Fig. 3-4(c).

$$SNR = \frac{S}{\sqrt{S + I_{BG}^{\ 2}}} \tag{3-4}$$

It is clear that SNR decreases due to the effect of background.

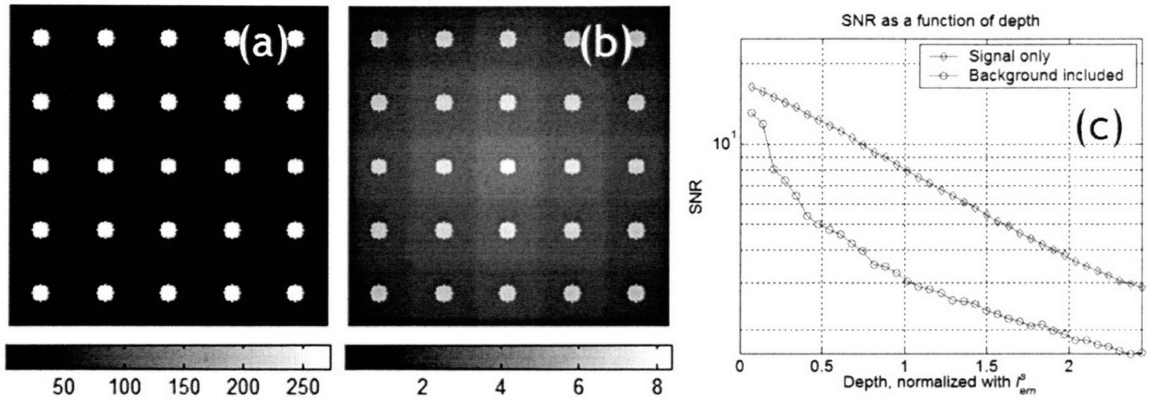

Fig. 3-4: Simulation of the effect of emission photon scattering on image contrast: measured PSF profiles are used in the simulation. The original image is circles of 10 μm diameter arranged with 40 μm separation distance. (a) is the image on the surface and (b) is the image at 2.4 times scattering length at emission wavelength. Background noise decays less than signal with the increase of scattering length. Background intensity around the center circle increases due to background accumulation from other circles around. Signal to noise ratio (SNR) with the background noise included is lower than the SNR with signal fluctuation only, (c).

The system sensitivity to emission photon scattering can be characterized by the detector effective area which is defined as the area in the sample plane covered by the detector. The larger the effective area of the detector, the better the detector can collect scattered photons. Since microscopes are telecentric systems, the effective area of a detector is proportional to its detection area with magnification M as the constant. For a microscope with magnification M, the effective linear dimension of the detector, L_E is related to its physical linear dimension L_D by $L_E = L_D/M$. For a PMT with the detection area of 10 mm diameter and a 40 × magnification microscope system, L_E is approximately 250 μm. This dimension is significantly larger than the FWHM of the scattered photon distribution which is approximately 100 μm. Therefore SMM using a PMT detector is sensitive to only the integrated total emitted signal but not the changes in PSF_{em} shape due to scattering. On the other hand, in a multi-channel detector such as CCD, each pixel works as an individual detector. The effective area of the detector is very small: for a CCD camera with 20 μm × 20 μm pixel size and a 40 × magnification, L_E becomes 0.5 μm × 0.5 μm. Therefore, the CCD camera is sensitive to emission photon scattering, because the effective area of the CCD camera is small compared to the FWHM of the scattered emission photon distribution.

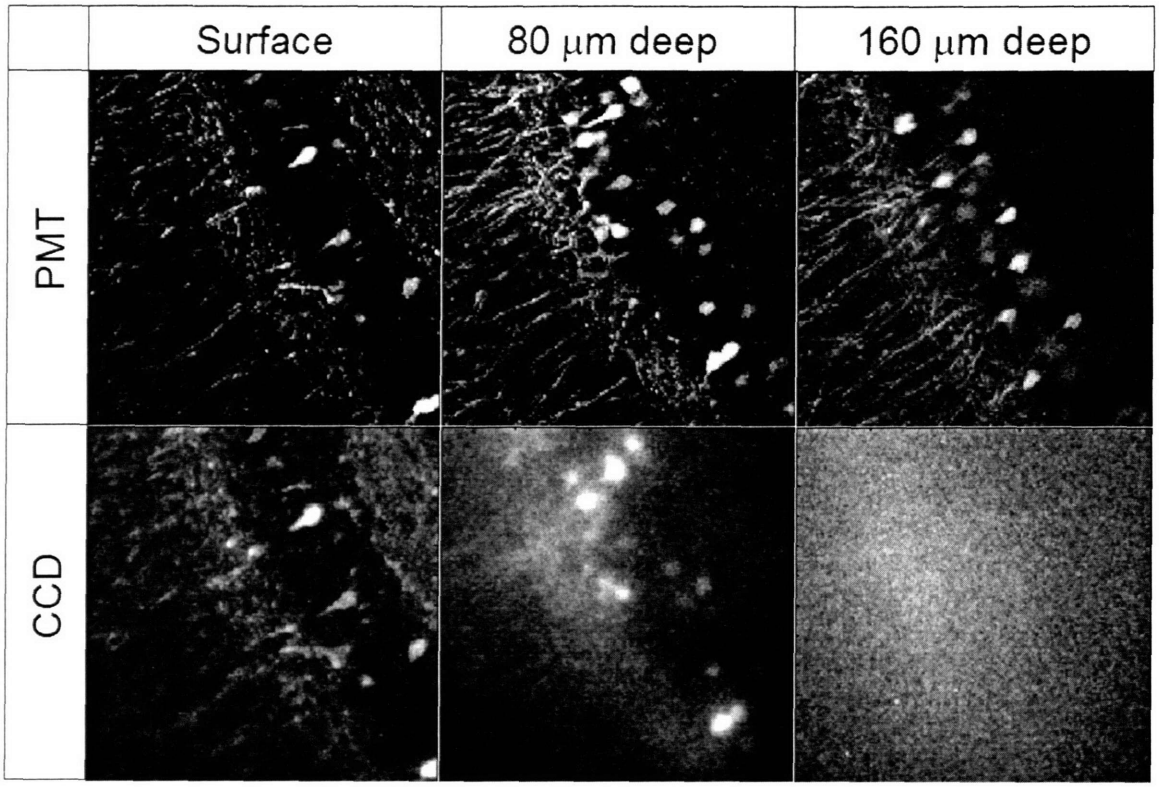

Fig. 3-5: Comparison of SMM and MMM in turbid brain tissue imaging: images of gfp expressing neurons at 10 μm deep, 80 μm deep, and 160 μm deep from the surface. Images from SMM keep good contrast up to 160 μm deep with neurons visible. Neurons are not quite visible at 160 μm deep, because images from MMM lose contrast quickly due to emission photon scattering. Image size is 160 μm × 160 μm deep.

Scattering effect on biological tissue imaging

As the verification of scattering effect on MMM imaging, we imaged highly scattering biological tissues using both SMM and MMM. The specimen was an ex-vivo brain tissue section with neurons expressing green fluorescent protein (GFP). Thy1-GFP transgenic mice(Feng et al. 2000) were deeply anesthetized with 2.5% Avertin (0.025 ml/g i.p.) and transcardially perfused with PBS, followed by 4% paraformaldehyde. Brains were dissected and placed overnight in cold 4% paraformaldehyde. 1-mm thick coronal sections were taken by vibrotome, mounted and coverslipped on microscope slides using adhesive silicone isolators (JTR20-A2-1.0, Grace Bio-Labs, Bend, OR).

The specimen was scanned with a single focus of excitation light and the emission photons were collected with both a CCD camera and a PMT. The image acquired with the CCD camera is equivalent to the one in MMM. 3D images were acquired up to the

depth of 240 μm from the surface and the degradation of image quality was compared. The objective used was 20 × water immersion with 0.95 NA (XLUMPLFL20XW, Olympus, Melville, NY). The input laser power was increased from 30 mW on the surface to 300 mW at 240 μm deep to maintain constant detected photon level in the detector. The wavelength of excitation laser was 890 nm. The acquisition time was 2.5 seconds per frame with 160 × 160 pixels. Its field of view was 110 μm × 110 μm.

Neurons imaged at different depths with SMM and MMM configurations are presented in Fig. 3-5. On the surface, both images show good contrast. At 160 μm deep, dendrites and cell bodies are clearly visible in the images from SMM, although signal level decreases. In the image from MMM, morphological structure is no longer visible due to contrast loss.

3.1.3. Conclusion

In conclusion, MMM may not be the ideal configuration for deep imaging in turbid tissue specimen. In MMM, image quality is affected by the degradation in the point spread function of the emission photons. We found that the image resolution is not changed up to 2 l_{em}^{s} which is mostly determined by the unscattered photon peak. However, image contrast is seriously degraded: only unscattered emission photons are collected as signal and scattered emission photons become background noise due to its broad spatial distribution. This fast loss of contrast in MMM is demonstrated in tissue imaging. Finally, up to $2l_{em}^{s}$, the FWHM of the scattered photon distribution is on the order of 40 μm. The effective detector dimension should be significantly large for high sensitivity imaging.

3.2. Multifocal multiphoton microscope based on MAPMT

3.2.1. Introduction

Multifocal multiphoton microscope (MMM) requires the use of spatial resolved detectors such as a charge couple device (CCD) camera and results in significant degradation of its ability for deep tissue imaging (Bewersdorf et al. 1998; Buist et al. 1998). We have recently shown that MMM signal is reduced fast with increasing imaging depth due to emission photons scattering, because only ballistic unscattered photons contribute as signal and scattered photons contribute to a wide background whose FWHM is approximately 40 μm at the imaging depth of $2\times l_{em}^{s}$ (Kim et al. 2005). To circumvent this limitation, we seek to create a new MMM design that can achieve significantly superior performance in thick tissue imaging. The major limitation of CCD-based MMM system lies in its small pixel area. For conventional wide field imaging, a large number of CCD pixels are needed to maintain good resolution while covering a good size field of view. A 100 μm size image will require about 10^7 pixels to be imaged at full optical resolution (300 nm). The situation is very different for MMM imaging. Since typical femtosecond light source can only provide at maximum 2-4 watts of optical power and typically about 20-100 mW are required at each focus to generate efficient two-photon excitation in thick tissues. MMM system can realistically only effectively scan about 20-200 foci in parallel within tissue specimens. Since these foci are raster scanned across the specimen, the image resolution is determined by the point spread function of the microscope and is not sensitive to the detector pixelation. In particular, MMM system can be designed with photon detectors containing only as many elements as the excitation foci. The need for fewer elements allows the use of detectors with significantly larger pixel area which is beneficial in collecting scattered emission photons. MAPMTs are excellent detectors for this purpose.

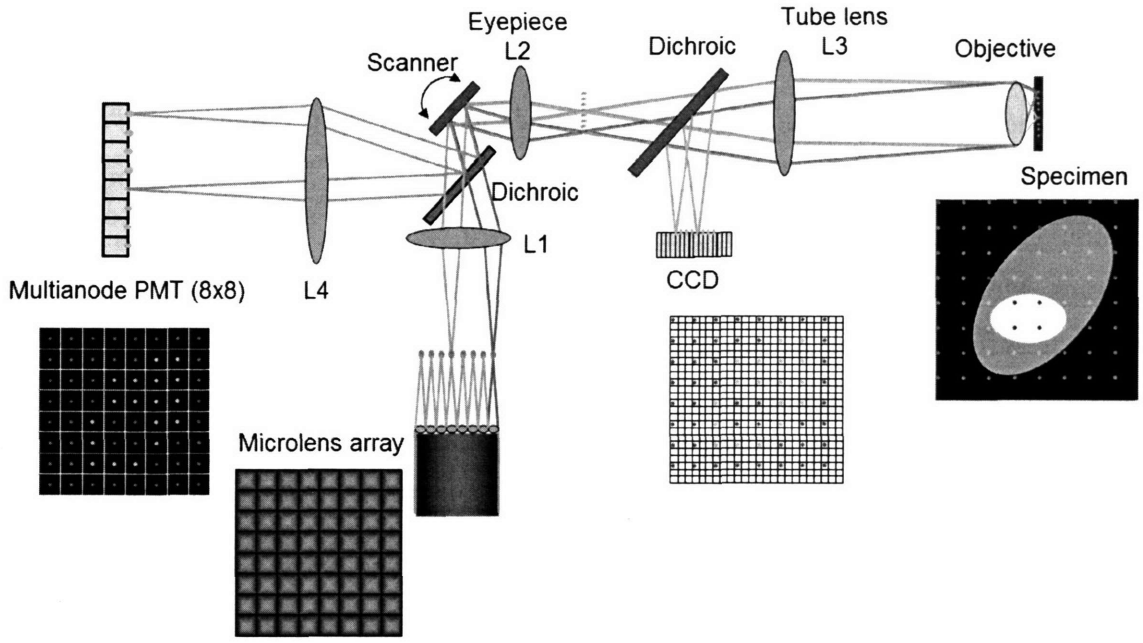

Fig. 3-6: Schematic of multifocal multiphoton microscope based on MAPMT. Excitation beam (expanded) comes from bottom of this figure and illuminate a square microlens array. The microlens array splits the excitation beam into 8 x 8 multiple beams (beam-lets). In this figure, only two beam-lets are ray-traced. A specimen is scanned with an 8 x 8 array of excitation foci. The sample area that each excitation focus covers becomes small. The emission beam-lets are either collected by CCD or MAPMT. CCD integrates signal during the scanning of a single frame. MAPMT which has only the same number of pixels as excitation beamlets, integrate signal of 8 x 8 pixels synchronized with the scanning.

The new system uses a MAPMT instead of a CCD camera as detector. The MAPMT is similar to conventional PMTs with a good quantum efficiency (over 20% in the blue/green spectral range), negligible read noise and minimal dark noise with cooling. MAPMT has a cathode and dynode chain with optimized geometry to ensure that the spatial distribution of photons on the cathode is reproduced faithfully as electrons distribution at the anode. The anode of the multi-anode PMT are divided rectilinearly into its elements providing spatial resolution for the simultaneously collection of signals from multiple locations. In our implementation, a MAPMT, which has an array of 8 × 8 pixels (H7546, Hamamatsu, Bridgewater, NJ) is used.

3.2.2. Instrument

The schematic of the microscope is shown in Fig. 3-6. The light source used is a Ti-Sapphire (Ti-Sa) laser (Tsunami, Spectra-Physics, Mountain View, CA) pumped by a continuous wave, diode-pumped, frequency-doubled Nd:YVO_4 laser (Millenia, Spectra-Physics, Mountain View, CA). It generates approximately 2 W at 800 nm wavelength which is sufficient for most MMM applications. The excitation beam from the laser is expanded and then illuminates a microlens array (1000-17-S-A, Adaptive Optics, Cambridge, MA) which is an array of 12 × 12 square microlenses that are 1 mm × 1 mm in size and 17 mm in focal length. We adjust the degree of beam expansion such that an array of 8 × 8 beam-lets is produced after the microlens array. The beam-lets are collimated after L1 and reflected onto an x-y scanner mirror (6220, Cambridge Technology, Cambridge MA) which is positioned in the focal plane of L1. In this configuration, the beam-lets overlap each other on the scanner mirror surface and are reflected similarly by the rotation of the scanner mirror. After the scanner, the beam-lets enter a microscope (BX51, Olympus, Melville, NY) via a modified side port. A combination of L2 and L3 expands the beam-lets to fill the back aperture of the objective in order to use the full numerical aperture (NA) of the objective. The scanning mirror is in the telecentric plane of the back aperture of an objective lens so that the beamlets are stationary on its back aperture independent of the motion of the scanner mirror. The objective lens generates the 8 × 8 focus array of excitation light in the sample plane in the specimen. The scanner mirror moves the array of excitation foci in the sample plane in a raster pattern to cover the whole sample plane. The objective used in this system is a 20 × water immersion lens with 0.95 NA (XLUMPLFL20XW, Olympus, Melville, NY). The excitation foci are separated each other by 45 μm so that the scanning area of each focus is 45 μm × 45 μm. The frame size is 360 μm × 360 μm by scanning with the array of 8 × 8 foci. The frame rate to generate images of 320 × 320 pixels becomes approximately 19 frames per second with the pixel dwell time of 33 μs.

Emission photons are generated at the array of excitation foci in the specimen and are collected by the same objective lens forming an array of emission beam-lets. In case

of CCD-based MMM, the emission beam-lets are reflected on a long-pass dichroic mirror (650dcxxr, Chroma Technology, Brattleboro, VT) and imaged on a CCD camera (PentaMax, Princeton Instruments, Trenton, NJ) with a lens (L3). The CCD camera integrates emission photons during the scanning time of each frame to generate an image. In case of MAPMT, the emission beam-lets travel back to the scanner mirror retracing the excitation paths. The emission beam-lets are reflected by the scanner mirror. The emission beam-lets are de-scanned and their propagation directions remain stationary irrespective of the movement of the scanner. The emission beam-lets are reflected by a long-pass dichroic mirror (650dcxxr, Chroma Technology, Brattleboro, VT) and are focused after lens (L4). A short-pass filter (E700SP, Chroma Technology, Brattleboro, VT) blocks any strayed excitation light. The focused emission beam-lets are collected at the center of corresponding channels of a MAPMT (H7546, Hamamatsu, Bridgewater, NJ). The emission photons coming from the array of excitation foci are collected by a MAPMT. An image is formed by the temporal encoding of the integrated signal with the known raster scanning pattern.

The pair of L2 and L4 magnifies the array of emission foci so that individual emission beam-lets are focused at the center of corresponding elements of the MAPMT. Further, since the emission beam-lets are descanned, they remain stationary. Since the emission beam-lets have to go through more optical elements, additional loss of emission photons occurs. The transmission efficiency is approximately 0.7. The signals from the MAPMT are collected by a stack of four multi-channel photon counter card (mCPhC) (Buehler et al. 2005) which has 64 channels for simultaneous signal collection. The detail electronic design of mCPhC has been previously published (Buehler et al. 2005). Each mCPhC has 18 channels photon counter circuits and a digital interface to a computer. The mCPhC is designed to be expandable so that 64 channels are readily implemented by using 4 cards in parallel. The mCPhC has 32-bit parallel interface with a computer for high-speed data transfer. Currently, the speed is limited by the speed of the computer PCI bus. Transfer rate can be more than a hundred frames (320 × 320 pixels, 16 bit images) per second.

Since the scattered emission photons have the spatial distribution of 40 μm as its FWHM at the imaging depth of $2 \times l_{em}^{s}$, the sensitivity of the microscope is partly determined by the effective detector area, the area in the sample plane from which a detector collects emission photons. Since microscopes are telecentric systems, the effective detector area is linearly related with the detector size in the image plane. With a magnification, M, and a linear dimension of detector, L_D, the linear dimension of effective detector area (L_E) is $L_E=L_D/M$. In general, the larger the effective detector area, the more effective the detector can collect scattered emission photons. In the case of using a 20 × magnification objective, a 10 mm diameter standard PMT has an effective detector area of 500 μm diameter that is significantly larger than the width of the scattered emission photon distribution. Therefore, standard PMTs have good collection efficiency of scattered emission photons and allow very effective deep tissue imaging. In the case of spatially resolved detector, each pixel should be treated as an individual detection element. For a CCD camera with 20 μm × 20 μm pixels, each pixel has an effective detector area of 1 μm × 1 μm for 20 × magnifications. Therefore, the CCD-based MMM system cannot utilize these scattered emission photons which are distributed uniformly throughout the image contributing to the background noise. The current MAPMT-based MMM design, the effective detector area of each channel is 45 μm × 45 μm. Therefore, the MAPMT can collect significantly more scattered emission photons into the correct channels than the CCD camera, because its effective detector area is comparable with the width of the scattered photon distribution.

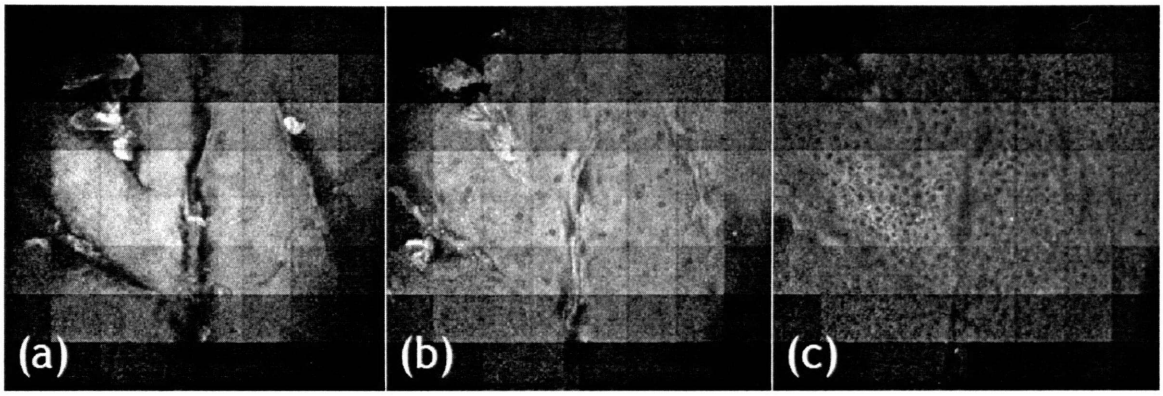

Fig. 3-7: Human skin image acquired with MAPMT-based MMM. Epidermal layer was imaged. From left to right, imaging depth goes deeper. Stratum corneum layer (a), stratum granular (b), and basal layer (c) are shown. Cells are visible with its autofluorescence. Image size: 360 um x 360 um, input power: 7 mW per focus, objective: 20 ×, imaging speed: 2.5 frames/s with 320 x 320 pixels.

3.2.3. Results and discussion

As a demonstration of the sensitivity of the new system, we imaged ex-vivo human skin in 3D. Imaging dermal structure based on autofluorescence is one of the most challenging deep tissue imaging task (Masters et al. 1997; So et al. 1998). Further, endogenous fluorophores have low quantum yield and low extinction coefficients compared with typical exogenous fluorescent labels (So et al. 2000). The dermal structure has a layered structure with significantly different indices of refraction resulting in significant spherical aberration (Dong et al. 2003). The specimen was cadaver skin from PennState Milton S. Hershey Medical Center (Hershey, PA). It was delivered in formalin. For imaging, it was mounted and coverslipped on microscope slides using adhesive silicone isolators (JTR20-A2-1.0, Grace Bio-Labs, Bend, OR). Typical multiphoton imaging of dermal structure without photodamage has a typical pixel rate of 15 KHz (So et al. 1998; Masters et al. 2004) with 15 mW input power. In this study, we use input power of 7 mW per focus at the specimen. The excitation wavelength is set at 800 nm. The objective used is 20 × water immersion with 0.95 NA (XLUMPLFL20XW, Olympus, Melville, NY). We could achieve a frame rate of 2.5 fps for a 320 × 320 pixel image (4 KHz pixel rate) that is 10 times faster than the published images. We imaged the epidermis down to the basal cell layer using this MAPMT-based MMM.

Representive layers from the stratum corneum, stratum granular, and the basal layer are shown in Fig. 3-7. The signal from these layers are mostly due to the fluorescence of NAD(P)H inside the cell. We can see that MAPMT-based MMM has equivalent sensitivity as the conventional multiphoton microscopy but with significantly increased imaging speed. The intensity of the image is not uniform: the intensity is high in the center and becomes dim in the corner of the image. This is because the intensity of excitation beam has Gaussian spatial distribution so that the beamlets made from center part of the expanded beam have higher intensity than the beamlets made from the side part.

In addition to demonstrate the efficacy in tissue imaging, we seek to better quantify and compare the system performance of CCD-based and MAPMT-based MMM in turbid medium. Using both type of detectors in MMM geometry, we measured the signal decay as a function of scattering length. As the imaging depth increases, the signal is decreased due to scattering of both excitation photons and emission photons. The signal decay is measured by imaging 4 μm diameter fluorescent latex microspheres (F8858, Molecular Probes, Eugene, OR) immobilized in 3D by 2 % argarose gel (UltraPure Low Melting Point Argarose, Invitrogen, Carlsbad, CA). Intralipid emulsion (Liposyn III, Abbott Laboratories, North Chicago, IL) is added to the sample as scatterer in various concentration of 0.5 to 2 %. Intralipid emulsion of 2 % volume concentration is known to have similar scattering properties to those of tissues: mean free path length (l^s) of scattering is 80 μm, 168 μm at the wavelength of emission (605 nm), and excitation (800 nm) respectively. The scattering properties of these intralipid solution are verified by diffusive wave measurements (Fantini et al. 1994). Peak intensity of the sphere image was considered as signal in the measurement and the decay of peak intensity as a function of the imaging depth is measured at each concentration. The signal decay is further acquired with a conventional single-focus multiphoton microscopy (SMM) as a reference which should have the best performance in deep tissue imaging. Signal decays in the three systems are measured down to a depth of 180 μm which is equivalent to $2.25 \times l^s_{em}$ (Fig. 3-8).

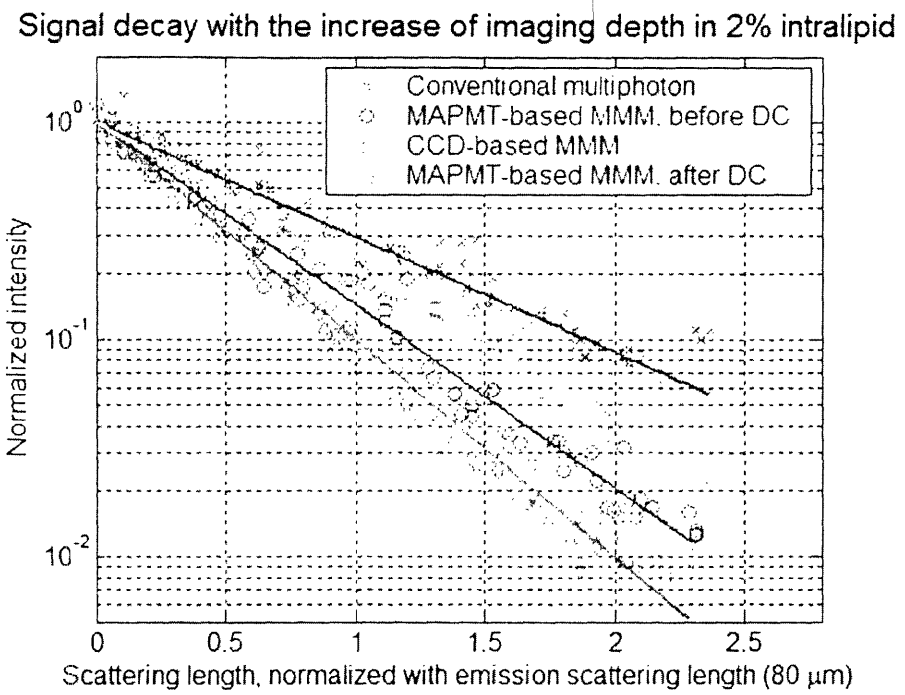

Fig. 3-8: Signal decay with the increase of imaging depth was measured with SMM, CCD-based MMM, and MAPMT-based MMM. The specimen was sparsely distributed 4μm red spheres (605 nm) in 2 % intralipid. Signal decay is due to scattering of both excitation and emission photons. Decay due to excitation photon scattering is the same for all the systems. Difference in the decay is because the difference in the collection efficiency of emission photons of the systems. Scatterer: 2% intralipid emulsion, the mean free path length at emission wavelength is 80 um. Objective: 20 ×. The signal decay is expressed an exponential function, . The decay coefficient, c is 1.22, 1.87, 2.30 in case of the SMM, MAPMT-based MMM, and CCD-based MMM respectively.

The signal decay is expressed an exponential function, $S(z) = \exp(-c\,z/l_{em}^{s})$. The decay coefficient, c was 1.22, 1.87, 2.30 in case of SMM, MAPMT-based MMM, and CCD-based MMM respectively. The decay rate from SMM was the lowest as expected. The decay was the combined effect of both excitation and emission photon scattering. Since the effect of excitation photon scattering is the same, the difference in decay coefficient is due to the effect of emission photon scattering. The decay coefficient, c from MAPMT-based MMM (1.87) is lower than the one from CCD-based MMM (2.30). However, c of MAPMT-based MMM was still higher than c of SMM. It is consistent with the fact that the spatial distribution of scattered emission photons had FWHM over 40 μm and was wider than the effective detector area of the MAPMT (45 μm × 45 μm) so that some portion of the scattered emission photons were collected in the neighboring

channels. The photon intensity collected in the neighboring pixels of the MAPMT was approximately twice the signal collected at the correct pixel at the depth of $2 \times l_{em}^{s}$.

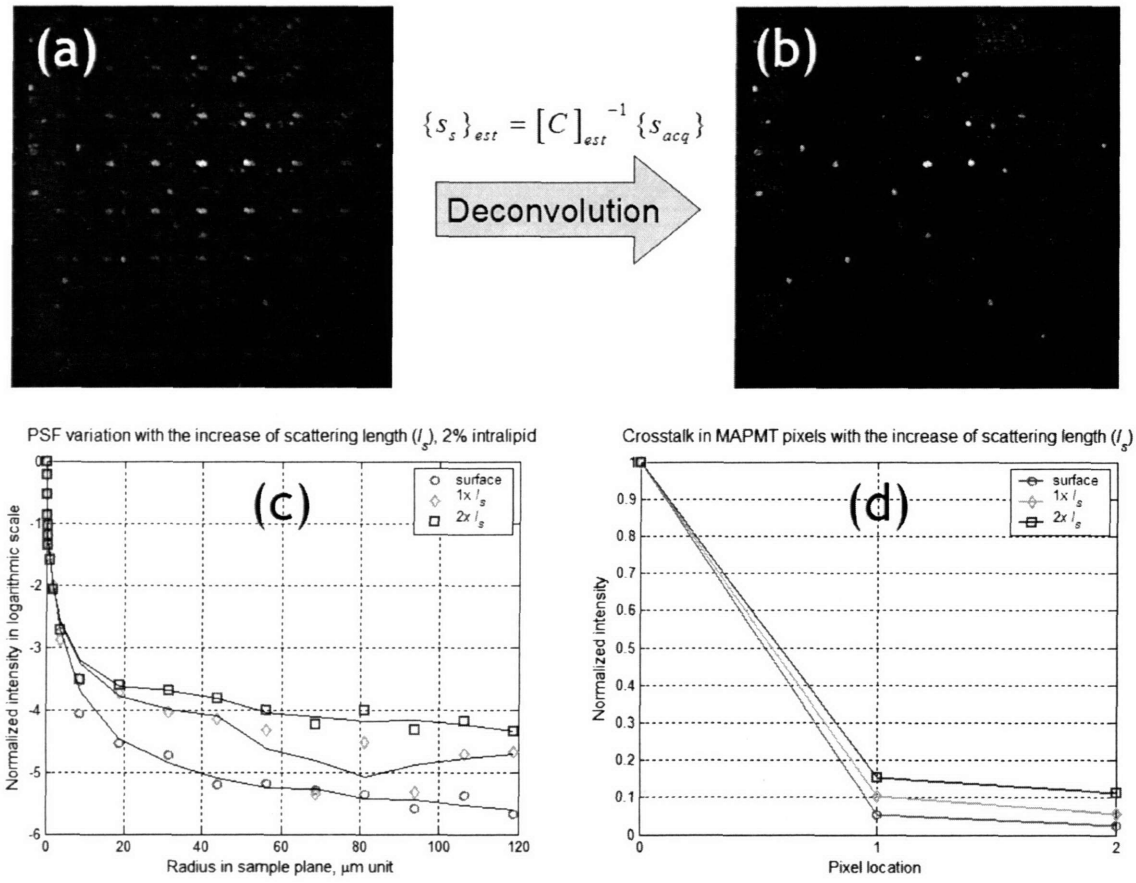

Fig. 3-9: Effect of emission photon scattering on images acquired with MAPMT-based MMM. (a) The image of spheres at 150 μm deep from the surface. Ghost images appear with the scattered emission photons collected in neighboring pixels of the MAPMT, (b) image after the deconvolution process, (c) Variation of PSF due to emission photon scattering, the increase of intensity in the tail is the effect of emission photon scattering (d) Crosstalk in the pixels of the MAPMT, it is calculated by integrating the PSF over the effective detector area of individual pixels of MAPMT.

Although a significant portion of the scattered emission photons are still distributed outside the correct pixels in MAPMT-based MMM, these photons can be effectively restored to the correct pixels based on post-acquisition image processing. Note that the photons acquired at each pixel are temporally encoded and are organized to form an image based on the known scanner position as a function of time. This is exactly how images are formed in a conventional multiphoton or confocal microscope. A

primary image is formed by photons acquired at the correct pixels corresponding to the fluorophore distribution in that portion of specimen. It should be noted that the scattered photons in the neighboring pixels are also similarly temporally encoded. Therefore, secondary "ghost" images are formed in the areas of the image covered by the neighboring pixels. As an example, Fig. 3-9(a) is an image of spheres at 150 μm deep (equivalently 1.9 × l_{em}^{s}) from the surface in 2 % intralipid emulsion. The fact that the primary image at one pixel is "copied" into neighboring pixel, the spatial distribution of the scattered photons provides critical information for the reassignment of these scattered photons back to the correct pixel. Note that this temporally encoded information is not available in a CCD-based MMM system where the temporal information is lost during the integration process of the CCD. The study of emission photon scattering on PSF_{em} showed that the scattered emission photons form additional intensity distribution around the PSF_{em}, which is formed with ballistic unscattered emission photons. Its distribution is broad with its FWHM of 40 μm range at the imaging depth of 2 × l_{s}^{em}. The variation in PSF with the increase of scattering length is shown in Fig. 3-9(c). This level of crosstalk among pixels of the MAPMT can be calculated with the spatial integration of PSF_{em} over the detector areas of individual pixels of the MAPMT. Fig. 3-9(d) shows the result of spatial integration. Horizontal axis is the pixel location and vertical axis is normalized intensity with respect to the value in the correct pixel (pixel 0). It is noted that the relative intensity in the neighboring pixels (pixel 1 and 2) increases with the increase of scattering length. In the design of the MAPMT-based MMM, the signals of 8 × 8 pixels are collected together each time so that the signal vector of those pixels which are acquired together, $\{S_{acq}\}$ (64 × 1) is the product of crosstalk matrix, [C] (64 × 64) and the source pixel signal vector in the sample plane, $\{S_s\}$ (64 × 1), $\{S_{acq}\} = [C] \times \{S_s\}$. The crosstalk matrix, [C] is constructed based on the crosstalk measurement based on quantifying PSF_{em} which is a function of emission scattering length. Since [C] is constructed by integrating PSF_{em}, the deconvolution here may be simple and may not be much sensitive to noise. In the real measurement, the information of PSF variation is not available, because the effect of emission photon scattering varies depending on the specimens. Therefore, [C] is roughly estimated by measuring the intensity ratio of the

real image to the ghost images as a function of imaging depth, $[C]_{est}$. The signal vector of pixels in the sample plane, $\{S_s\}_{est}$ is calculated by the product of the inverse transform of $[C]_{est}$ and the acquired pixel vector, $\{S_{acq}\}$.

$$\{S_s\}_{est} = [C]_{est} \times \{S_{acq}\} \tag{3-5}$$

The restored image is presented in Fig. 3-9(b). We measured the signal decay of a depth sequence of restored images and found that the decay coefficient, c is significantly reduced to 1.58 after the deconvolution algorithm (Fig. 3-8) because the scattered emission photon can now be corrected reassigned. We can clearly see that the ghost images are almost completely eliminated. Restoration algorithms can be further refined such as by adding maximum likelihood estimation to minimize image structural overlap between neighboring pixels. This process may also better handle the effect of tissue heterogeneity on [C]. Nonetheless, this simple deconvolution approach improves very effectively the performance of MAPMT-based MMM and allows this system to perform within a factor of two compared with conventional multiphoton microscope.

We further compared the performance comparison of the two MMM systems in the imaging of biological tissues. The specimen was an ex-vivo brain tissue section with neurons expressing green fluorescent protein (GFP). Thy1-GFP transgenic mice (Feng et al. 2000) were deeply anesthetized with 2.5% Avertin (0.025 ml/g i.p.) and transcardially perfused with PBS, followed by 4% paraformaldehyde. Brains were dissected and placed overnight in cold 4% paraformaldehyde. 1-mm thick coronal sections were taken by vibrotome, mounted and coverslipped on microscope slides using adhesive silicone isolators (JTR20-A2-1.0, Grace Bio-Labs, Bend, OR). The specimen was imaged in 3D with both CCD-based MMM and a MAPMT-based MMM. The objective used was 20 × water immersion with NA 0.95 (XLUMPLFL20XW, Olympus, Melville, NY). The input laser power was 300 mW at 890 nm wavelength. The frame rate was 0.3 frames per second with 320 × 320 pixels. The slow frame rate was set in order to collect enough emission photons up to 120 μm deep. The total imaging depth was 120 μm with 1.5 μm depth increment. Representative images are shown in Fig. 3-10.

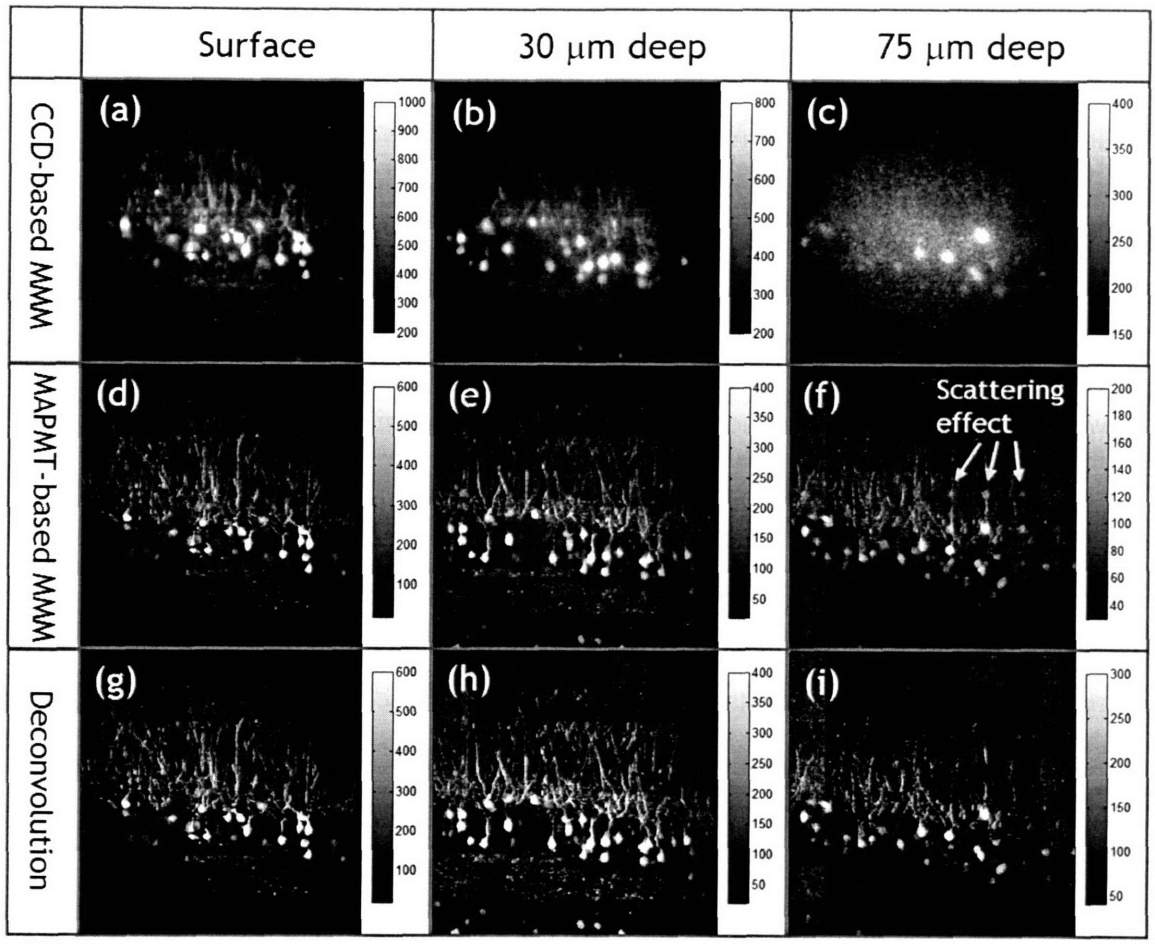

Fig. 3-10: Neuron images acquired with CCD-based MMM (a-c) and MAPMT-based MMM (d-f) at different depth locations (surface, 30 um, and 75 um deep). The images with at For images with MAPMT-based MMM, a deconvolution algorithm was applied to remove the effect of emission photon scattering (g-i). Objective: 20 × water immersion with NA 0.95, input laser power: 300 mW at 890 nm wavelength, frame rate is 0.3 frames per second with 320 × 320 pixels.

The first row images are from CCD-based MMM at surface, 30 μm, and 75 μm deep (a-c). The second and third row images are the ones from MAPMT-based MMM, raw images (d-f) and the ones after the decovolution processing (g-i). On the surface, the dendritic structures of neurons are visible in all images. However, the image from CCD-based MMM does not provide as good contrast of neurons as MAPMT-based MMM. This is because some of the emission photons that are initially forward propagating into the tissue are eventually back scattered. These back scattered photons are acquired in the incorrect pixels of the CCD and degrades the image SNR. Starting at about 30 μm, background noise increases and thin dendrite structure becomes invisible in CCD-based

MMM images. On the other hand, in the images from MAPMT-based MMM, dendrites are still visible due to lower background noise and higher SNR. In the image of 75 μm deep from MAPMT-based MMM, ghost images of a bright cell body appear in the neighboring pixels (f). The ghost images are restored to the original image after the deconvolution process is applied (i). And also it is noted that the intensity of neurons are increased in the deconvolved image (i).

As the first design of MAPMT-based MMM, this system performed satisfactory. However, additional improvements of this system are possible. First, since the MAPMT is positioned in the image plane, the location of each excitation focus corresponds to the center position of the matching pixel of the MAPMT. The effective detector area is scales quadratically with the separation of the foci. Therefore, with wider foci separation, the MAPMT has higher collection efficiency for scattered emission photons. In the current configuration, the excitation foci are separated each other by 45 μm so that the effective detector area for each channel of the MAPMT is 45 μm × 45 μm. The size of imaging field with 8 × 8 foci becomes 360 μm × 360 μm. As the excitation foci are separated more, the system becomes less sensitive to the scattering of emission photons. The maximum separation of excitation foci is limited by either the field of view of the objective or apertures of other collection optics. The 20 × water immersion objective used has the field of view of 1000 μm in diameter. This will allow us to position the foci as far apart as almost 100 μm.

Second, a major disadvantage of MAPMT-based MMM design compared with a CCD-based MMM design is that the signals are de-scanned. In the de-scanned configuration, emission photons are processed by more optical elements including the scanner mirror before they are collected at the MAPMT suffering more optical loss at each reflection. Further, the de-scanned geometry also has a longer optical path contributed to the loss of some scattered photons due to the finite aperture of the optics. We found that the signal collection efficiency is approximately 70 % due to additional optical elements. We are currently designing a MAPMT-based MMM system in a non-de-scanned geometry and can potentially recover this loss.

Third, the MAPMT are not manufactured in the most efficient cathode material with current quantum efficiency of about 20 % compared to 80% quantum efficiency of the CCD camera. However, MAPMT has very low noise. It has 20 dark counts per second without cooling and can be several orders of magnitude lower with cooling. Since the MAPMT has a readout rate of approximately 20 KHz, the typical dark count per pixel is less than 1×10^{-3}. Therefore, for very low photon count situation, i.e. dim sample or high frame rate, the MAPMT system can have superior performance. Finally, the production of MAPMTs with higher sensitivity cathode materials such as GaAsP are being considered by the manufacturer and this can bring the quantum efficiency up to about 40-50%.

Fourth, the photon sensitivity of each channel is not equal and can vary up to 50%. This effect is further compounded by the Gaussian geometry of the excitation beam which results higher excitation efficiency at the center pixels verses the edge region. This problem has been solved previously using multiple reflecting beam splitter to generate equal intensity beam-lets (Nielsen et al. 2001). The MAPMT-based MMM system can be further improved by utilizing this type of beam splitter with additional flat field correction algorithm to remove inherent sensitivity non-uniformity of the MAPMT.

Fifth, there is also cross talk between neighboring pixels of MAPMT. The typical crosstalk is minimal about 2% when the photons are collected at the center of each pixel. However, this cross talk can be removed by post-processing of the image similar to ghost image removal discussed previously.

Finally, in MMM imaging, higher power laser is required. Assuming that input power of 2 mW is needed for each excitation focus for efficient imaging on the sample surface with efficient pulse compression, the generation of 64 excitation foci requires 128 mW input power. In the imaging of turbid tissue specimens, more input power is required to compensate the signal loss due to excitation photon scattering. In case of a tissue specimen whose mean free path length is 160 μm at excitation wavelength, the input power of 8 mW and 24 mW are required to image at 100 and 200 μm deep respectively, assuming that signal level is decreased only due to excitation photon scattering and there is no change in collection efficiency of emission photons. Practically

there is a significant loss in excitation power delivery via all the optical elements. Typically the power loss is factor of 3. Therefore, the required power is 24 and 72 mW for 100 and 200 μm deep imaging. Therefore, over 1500 and 4500 mW are needed for 64 foci imaging. Therefore, more power is needed either to increase imaging speed or to image deeper. Therefore, the current power of Ti-Sapphire laser is limitation for MMM imaging and further increase in imaging speed by the use of even more foci.

3.2.4. Conclusion

In conclusion, a high-speed multifocal multiphoton microscopy is developed based on MAPMT. The imaging speed is increased by 64 times by scanning the specimen with the 8 × 8 array of excitation foci and by acquiring signal from those foci simultaneously with a MAPMT which have 8 × 8 channels. The system has very low noise by collecting signal in photon counting mode. MAPMT-based MMM system is optimized for high-speed turbid imaging of thick tissues because it is significantly less sensitive to the effect of emission photon scattering as compared with CCD-based system. Also application of a simple deconvolution algorithm lowered the effect of emission photon scattering further. The high sensitivity of the system was demonstrated in the imaging of ex-vivo human skin based on weak endogenous fluorophores. We further compared the performance of MAPMT- and CCD-based MMM in the imaging of tissue phantoms and GFP expressing neuronal structures in mouse brain slices. We clearly demonstrate that the performance of MAPMT-based MMM is greatly superior to CCD-based MMM.

3.3. Three-dimensional tissue cytometer

3.3.1. Introduction

Traditional cytometry (Darzynkiewicz et al. 1999; Steiner et al. 2000; Rieseberg et al. 2001; Tarnok et al. 2002; Ecker et al. 2004; Gerstner et al. 2004) can quantify minute differences between cellular population based on high throughput optical analysis of cellular states. Unlike other analytical methods, such as fluorescence spectroscopy (Muller et al. 2003) that measures only the averaged properties of the population, cytometry quantifies the state of individual cells. By rapidly measuring properties of individual cells from a population containing thousands to millions of cells, cytometry not only measures the average of cellular properties but also their exact statistical distribution. Therefore, a large population of cells from a specimen can be categorized into subpopulations based on their parametric distributions. Minor cell populations of different properties can be identified in a large population of other cells. Cytometry can be classified into two categories, flow cytometry (Rieseberg et al. 2001) and image cytometry (Darzynkiewicz et al. 1999; Tarnok et al. 2002) depending on measurement methods. Flow cytometry measures the properties of cells carried through the detection region in a fluid stream based on their optical characteristics such as fluorescence, light scattering, and light absorption. Flow cytometry quantifies properties such as cell size based on the magnitude of light scattering, membrane potential, and intracellular pH, and calcium based on environmental sensitive fluorescent probes, and the quantity of cellular components such as DNA and surface receptors based on organelle specific fluorescent labels. Flow cytometry with the throughput up to 10,000 cells/s has been demonstrated. Flow cytometry has been used for rare event detection down to the frequency of $1/10^7$ (Rieseberg et al. 2001). Further, cell sorting methods implemented with flow cytometry enables physical selection of a specific cellular subpopulation for further analysis and clonal propagation. Therefore, the combination of flow cytometry and cell sorting method is now an indispensable tool in immunology, molecular and cell biology, cytogenetics, and the human genome project. However, there are some limitations in

flow cytometry. (1) Specimens have to be prepared in fluidic suspension. Therefore, most of morphological information of cells and structural information of tissue are lost. (2) Time sequential study is almost impossible, because the specimen won't be in the same condition once it has been examined by flow cytometry.

Image cytometry has been recently introduced as a complementary method for flow cytometry. In image cytometry, individual cells are prepared in 2D culture plates and imaged by either wide field or laser scanning microscopy. Although the throughput rate of this method is relatively low, hundreds to thousands cells per second, it has several unique advantages. (1) Detailed cellular morphological and structural information can be assayed. (2) Individual cells of interest can be relocated so that they can be further analyzed. One key example is the ability of this method to monitor the temporal evolution of a cellular subpopulation. (3) Image cytometry also provides protein distribution information such as the membrane verses cytosolic distribution of receptors. (4) Image cytometry can be applied to tissue specimens when they are prepared as thin histological sections (Steiner et al. 2000; Ecker et al. 2004; Gerstner et al. 2004). For example, the spatial distribution of leukocytes in lymph nodes was measured and can potentially quantify effectiveness of different therapies (Gerstner et al. 2004). The phenotypes and quantities of tissue-infiltrating leukocytes were further characterized to monitor the response of immune system to transplants and therapies (Ecker et al. 2004).

The behavior of cells in multicellular organisms such as tissues is different from single cells (Davies 2001). The cells become specialized, acquiring distinct functions that contribute to the survival of the organism. The behavior of individual cells is integrated with that of similar cells, so that they act together in a regulated fashion. This coordinated behavior is possible with cell-cell and cell-extracellular matrix (ECM) interaction. ECM is composed of a gel formed from a number of matrix proteins. Matrix proteins are tightly bound to form extensive network of insoluble fibers. Cells are connected to ECM via their membrane receptors. The integrins act as mediator through which the mechanical network of the cytoskeleton can be connected to that of ECM. This integration of cytoskeleton and ECM is important for both – cells use their integrins to 'sense' the arrangement of the matrix and align their internal cytoskeleton appropriately. Reciprocally, tension generated by cells' cytoskeletons and communicated

to the matrix via integrins can organize the laying down of new matrix fibers along lines of force. In this way, tissue architecture can adapt to the mechanical demands made of it. In addition to mechanical force transduction, ECM also has other critical tissue functions such as serving as an important reservoir of cytokines and other signaling molecules and as controllable pathway of cellular movement. Therefore, it is important to study cellular behaviors in the native context of their ECM. In addition to cell-matrix interaction, cell-cell interactions are also crucial in regulating cell functions. Cell-cell interactions are either lost or altered when cells are grown in culture or dissociated from their native tissue environment. The physiology of pancreatic islets is an example of where cellular behavior in culture and in their native environment are very different (Bennett et al. 1996). Bennett et al. used two-photon microscopy to monitor cells redox activity inside in intact pancreatic islets. Cell redox activity is monitored by their NAD(P)H level. Previous research on cells grown as 2D cultures shows significant cell-cell variations in NAD(P)H level change in response to external glucose levels. This 2D culture experiments result in metabolic models of glucose metabolism based on step-wise recruitment of individual cells. However when Bennett et al. imaged cells within intact islets they found significantly more homogeneous glucose response suggesting that the step-wise model based on 2D culture results may not be relevant to the actual physiological insulin response in the pancreas of animal or people. This difference is clearly important for the design of pharmaceuticals for diabetes treatment.

We introduce a 3D tissue cytometer based on a high-speed multiphoton microscopy. It extends traditional image cytometry by providing the ability to quantify the 3D cellular and extracellular matrix morphological states in their native tissue environment. Thick tissue specimens can be imaged in 3D with penetration depth of a few hundred micrometers by using multiphoton microscopy (Denk et al. 1990; So et al. 2000). Optical sectioning of thick tissue allows 3D structures of tissue structures to be measured with high fidelity without mechanical perturbation. Further, multiphoton microscopy induces little phototoxicity to specimens with the confinement of excitation to only the focus. Therefore, in vivo 3D tissue cytometry is possible in tissues or engineered tissue constructs. The main obstacle in applying multiphoton microscopy for tissue cytometry is the limited speed of typical TPM system but this difficulty has been

circumvented by the introduction of high speed multiphoton microscopes. We designed an instrument that can assay the tissue volume of 3 mm × 3 mm × 100 μm (width, height, and depth) with 1 μm^3 resolution within 2 hours. If the tissue volume contains tightly packed, stratified cellular layers, this instrument samples approximate 100-200 cells per second (Kim et al. 1999; Kim et al. 2005). Therefore, 3D tissue cytometer can be used to screen a large population of cells inside intact tissues where one million cells can be quantified within 2 hours. In histology and tissue examination with image cytometry, tissue specimens need to be sliced very thin in order to be imaged. Slicing always generates distortion in the structure of tissue specimens (Tarnok et al. 2002). Another feature of 3D image cytometry is that it can avoid the artifact of slicing by imaging directly inside tissues up to couple hundred micrometers deep. With the progress of fluorescence probe technology, tissue structures and protein expression distributions can be labeled in the tissues of animal models based on technologies such as fluorescence in situ hybridization technology. Further, advanced genetic engineering allows the creation of transgenic animals that can express fluorescent sensors triggered by specific genetic events. One example is Recombomice (Hendricks et al. 2004) which carry fluorescent markers for homologous mitotic recombination events.

3.3.2. System characterization

The throughput of the cytometry system is critical to sample large tissue volume and cell population within a reasonable time period. The throughput rate is determined depending on the size of field of view in the microscope system and the imaging speed. The bigger the field of view is, the larger tissue area can be sampled. Therefore, the objective of lower magnifications is preferred. However, it is also critical to use the objective of a high numerical aperture (NA) to achieve micron scale resolution and to maximize the collection of emission signal. We designed two tissue cytometer both based on HSTPM, one is a single focus system while a second one is based on MMM design. In the single focus system, a 25 × water immersion, NA 0.8 (LCI Plan-Neofluar 25 ×, NA 0.8, Zeiss, Thornwood, NY) is used and the field of view is approximately 200 μm × 200 μm. And the imaging speed is 13 frames per second. In multifocal

multiphoton microscope, a 20 × water immersion, NA 0.95 objective (XLUMPLFL20XW, Olympus, Melville, NY) is used and the field of view is 270 μm × 270 μm. And the imaging speed is approximately 19 frames per second. Assuming that the average volume of single cells is 8000 μm^3 (20 μm × 20 μm × 20 μm) and the tissue specimen is imaged up to 100 μm deep from the surface ,each imaging section contains approximately 500, 911 cells for single-focus and multifocal system respectively. The throughput rate becomes 58, 145 cells per second for the single-focus, multifocal system respectively with 100 image layers per section (1 μm depth increment).

Since the frame size is about a few hundred micrometers square limited by the field of view of the objective, a computer-controlled high-speed specimen stage is needed to sample a larger sample area. A computer-controlled specimen translation stage (H101, Prior Scientific, Rockland, MA) is used for the precise movement of a specimen in case of wide section imaging to screen a large cell population. It is driven by step motors in 3 axes and its resolution is ±3 μm. It is controlled from a computer via the serial port. Its response time is approximately 0.5 sec (depending on the computer speed due to delay time from computer and the travel distance). Significant improvement of this 3D tissue cytometer will be possible with a higher bandwidth stage.

3.3.3. Procedures and Results

A Rare cell detection in 2D and 3D cell culture

We characterized the performance of this instrument in quantifying the rare cell population in 2D and 3D specimens in vitro. Two populations of cells with distinct fluorescent labels were mixed at ratios from 1/1 down to $1/10^5$. The specimens were prepared either as 2D tissue cultures or as 3D artificial tissues by growing in collagen scaffolds. The measured population ratios, which were obtained with an image analysis of the 3D image stacks, agreed well with the expected ratios.

3D and 2D Cell Culture Preparation

3D specimens of cell mixtures were prepared with help of Michael Previte. NIH 3T3 mouse fibroblast cells were grown in collage scaffolds to mimic tissue environment with cell spread in 3D. Collagen scaffold (O'Brien et al. 2005) has been used extensively as biomaterial in tissue engineering. Their porous structure serves as an analog of the extracellular matrix (ECM) and acts as a physical support structure and as an insoluble regulator of biological activity that directs cellular processes such as migration, contraction, and division. Two groups of cells were grown. One group was stained with green CellTracker dye (C2925, Molecular probes, Eugene, OR) and the other group was not stained. The CellTracker dye was chosen because its permanence in live cells through multiple divisions. For CellTracker labeling, CellTracker dye was diluted to 10 μM in serum free media. Medium of culture dishes containing about two million cells was removed and the dye solution was added. The specimens were incubated at 37 °C for 45 minutes with the dye solution and then the solution was replaced with culture medium. After the replacement, the dishes were incubated for another 30 minutes. Afterwards, both labeled and unlabeled cells were trypsinized from the dishes and cell densities were measured with hemocytometer (1483, Hausser scientific, Horsham PA). The stained cells were mixed with unstained (control) cells at ratios from 1/1, 1/10, down to $1/10^5$. The final concentration of the cells mixtures were adjusted to 2 million cells per milliliter. 25 μL of cell mixtures were seeded onto collagen scaffolds of 15 mm × 15 mm. Prior to the seeding, the collagen scaffolds were incubated in culture medium for 6 hours so that the medium became in equilibrium in the scaffolds. The collagen scaffolds were dried out slightly for 0.5 hour in the incubator in order to absorb an additional 25 μL solution of the cell mixture. Medium was added to the collagen scaffolds after 1 hour and the collagen scaffolds were incubated for 12 hours allowing the cells to migrate inside the scaffolds. The collagen scaffolds containing the cell mixtures were subsequently fixed with buffered zinc formalin (Z-fix, Anatech LTD, Battle Creek, MI). The cells were fixed in this experiment to prevent cell division that might occur at different rates for stained and un-stained cells. After fixation, all cell nuclei were stained with Hoechst (33342, Molecular probes, Eugene, OR). The Hoechst stock (10 mg/ml) was diluted to final concentration of 1/2000 times in PBS solution. The concentration of

Hoechst dye was chosen to approximately equalize the intensities of Hoechst and CellTracker. The scaffolds were incubated at 37 °C for 10 minutes with Hoechst solution and washed with PBS. The scaffolds were placed on microscope glass slides and sealed with silicone isolators (JTR20-A2-1.0, Grace Bio-Labs, Bend, OR).

The 2D specimens of cell mixtures were prepared by Molly S. Stitt in the laboratory of Prof. Bevin P. Engelward in biological engineering, MIT (Stitt 2001). 3T3 mouse fibroblast cells were transfected with plasmids of pCX Yellow and pCX Cyan consisting of the coding regions for Enhanced Yellow Fluorescent protein (EYFP) and Enhanced Cyan Fluorescent protein (ECFP) from Clontech (Palo Alto, CA) under the control of the pCX (chicken beta actin) promoter. 3T3 cells were lipofected with the plasmids using LipofectAMINE-Plus (Invitrogen, Carlsbad CA). EYFP and ECFP cells were grown separately. EYFP and ECFP cell stocks were trysinized, counted, and mixed at different dilution ratios. Cell mixtures were cultured on the glass slide (354111, BD Biosceinces, San Jose, CA) for 24 hours. The specimens were rinsed with PBS and then sealed with coverslip glasses before imaging. These cells were not fixed before 2D imaging, because the imaging could be performed at higher speed and cell division was not a major issue.

Data acquisition and analysis

As a demonstration that the 3D tissue cytometer can quantitatively categories subpopulations of cells based on their fluorescence properties, two cell subpopulations were mixed at ratios from 1/1 to $1/10^5$ are imaged with 3D tissue cytometer. The goal of this experiment is to test whether the 3D tissue cytometer can detect a rare cell subpopulation in a pool of the other subpopulation. We had further prepared 2D and 3D cell cultures to investigate the performance in both cases.

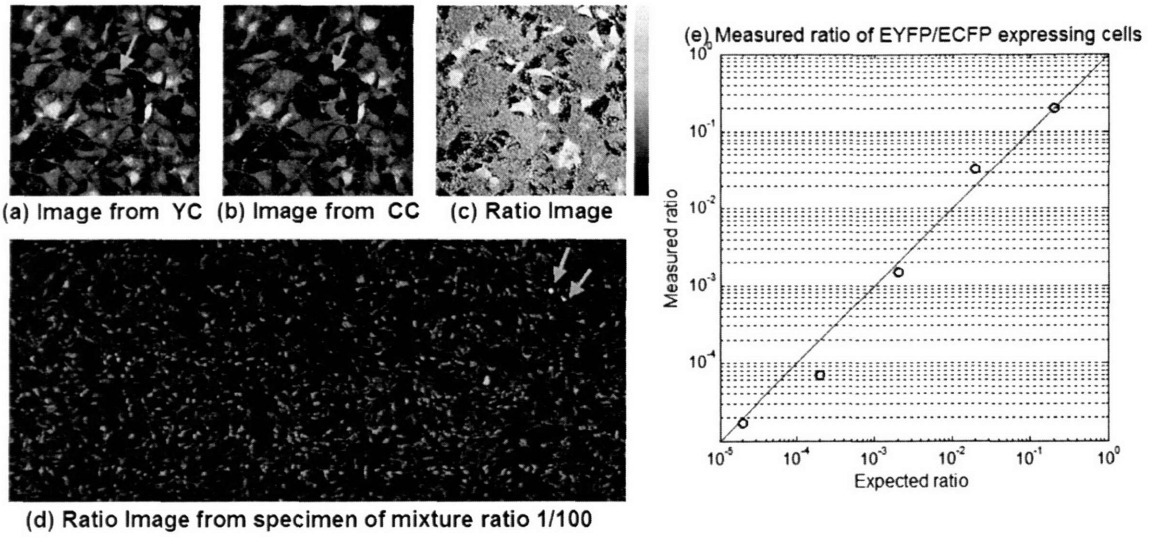

Fig. 3-11: Cell counting in the mixture of two subpopulations (ECFP, EYFP expressing cells) in 2D. (a-c) are images of mixture ratio 1/10 specimen from yellow channel (YC), cyan channel (CC), and from ratio analysis each. The cell pointed with an arrow is an EYFP cell which appears only in YC. It appears as a high ratio in the ratio image. (d) is ratio image of cell mixture 1/100. Only two EYFP cells were found. (e) shows that measured ratios agree well with expected ratios.

In the 2D case, two subpopulations cells expressing EYFP and ECFP were mixed at the known ratios from 1/1 down to $1/10^5$. These proteins were chosen with the consideration that both colors can be simultaneously excited with a single excitation wavelength and that the emission spectra of two fluorescent proteins could be easily distinguishable. We performed this experiment in the single focus tissue cytometer system. Excitation wavelength was set at 910 nm. A 25 × objective lens (LCI Plan-Neofluar 25 ×, NA 0.8, Zeiss, Thornwood, NY) was used. Although the specimens were monolayer cells, we chose to image 10 layers in the depth direction with a separation of 2 μm. Since the high numerical aperture objective has a narrow depth of focus on the order of microns, imaging a small volume stack ensures that the cell layer remained in focus within this image stack eliminating any artifacts from imperfect leveling of the specimen. In order to achieve reasonable statistical accuracy, we aimed to detect at least 10 rare cells at each mixture ratio. Since these specimens were composed of monolayer cells, the throughput rate is much lower as compared to that of 3D case in which multiple cell layers would be screened.

For the distinction of two fluorescent colors, two channel detectors were prepared using a dichroic mirror and two barrier filters, one long pass (for yellow color, referred as yellow channel, YC) and short pass (for cyan color, referred as cyan channel, CC) each. For the distinction between ECFP and EYFP, a dichroic mirror with 495 nm cutting wavelength (495DCXR, Chroma Technology, Brattleboro, NH), a long pass filter with 500 nm (E490SP, Chroma Technology, Brattleboro, NH), and a short pass filter with 490nm (E490SP, Chroma Technology, Brattleboro, NH) were used. Fig. 3-11(a) and (b) are representative images from the yellow and the cyan spectral channel (YC, CC) respectively. The mixture ratio of EYFP cells to ECFP cells was 1/10. Cells with both EYFP and ECFP appeared in YC since there was significant bleed through of the cyan emission into YC. On the other hand, in CC, only cells with ECFP showed up (Fig. 3-11b). For the clearer distinction, ratio images were constructed by combining two images according to equation (1).

$$I_R = \left(\frac{I_{YC} - I_{CC}}{I_{YC} + I_{CC}} \right) \tag{3-6}$$

I_R represents the pixel value of ratio images. I_{CC} and I_{YC} denote pixel values of CC and YC images respectively. Fig. 3-11(c) is the ratio image which was constructed with Fig. 3-11(a) and Fig. 3-11(b). To remove noise, ratio images were masked with a binary mask resulting from thresholding the yellow channel image. The threshold was chosen based on noise level of the image. Pixel values of the ratio images were always between –1 and +1 by the definition of equation (3-1). Given the fluorescent proteins' spectral properties, cells with EYFP had pixel values in the range of 0.95, and the pixel values of cells with ECFP were in the range of 0.5. Fig. 3-11(d) was the ratio image of specimen with mixture $1/10^3$ where only 2 cells expressing EYFP appeared. Specimens of other mixture ratios were imaged and the results were plotted in Fig. 3-11(e). The x-axis was the expected ratio and the y-axis was the measured ratio. The linearity of the relationship demonstrates the accuracy of this system. For the precise statistical analysis, the specimens of pure yellow cells only, pure cyan cells only, and cells of no fluorophores are needed as control specimens to verify the criterion used here. For example, the analysis of the pure yellow cell specimen will tell how well the criterion

judges correctly and misjudges. However, the linear relationship of expected ratios and obtained ratios tells that the criterion used in the analysis works well.

Similar characterization experiments were performed in 3D. Two subpopulations of cells were prepared where one subpopulation was unlabeled and the other minor subpopulation was labeled with CellTracker Green. Both cell subpopulations were stained with Hoechst such that their nuclei could be visualized to be counted. The specimens were imaged in 3D with the multifocal 3D tissue cytometry system operating at 30 frames per second. The imaging was done with the help of Karsten Bahlmann in our group. The excitation wavelength was 800 nm. The objective used was a 20 × water-immersion with NA 0.95 (XLUMPLFL20XW, Olympus, Melville, NY). The input power was 670 mW. The size of image was approximately 270 μm × 270 μm containing 192 × 192 pixels. For 3D imaging, 50 layers were imaged in each section with a 2 μm depth increment. This depth range covered about 3 to 4 layers of cells. The specimens were imaged with 2 color channels, a blue channel (BC) and a green channel (GC) utilizing the dichroic mirror with its cutting wavelength at 500 nm (500DCXR, Chroma technology, Brattleboro, VT). Barrier filters were not used to collect the maximum emission signal. The acquired data was analyzed to measure the composition ratio of two subpopulations by counting the number of cells of each type. The image analysis was performed with the help of Tim Ragan in our group. The cell counting algorithm is written in MatLab (MathWorks, Natick, MA). Analyzed results were presented in Fig. 3-12. Fig. 3-12(a) is a representative 3D image of 1/1 ratio specimens. One population of cells that was stained only with Hoechst showed blue emission in their nuclei. The other cells, which were stained also with CellTracker green, had both blue and green emission in their nuclei and only green emission in their cytoplasm. We focused our analysis on the intensity ratio of green to blue channel ($I_R = I_{GC}/I_{BC}$) in the nuclei both to count the total cell population and to distinguish the two subpopulations. Focusing our analysis on the nucleus portion of these images was very effective for the following reasons. (a) The intensity at nuclei was high in general so that it was easy to discriminate from background noise. (b) Nuclei were generally round and can be readily discriminated from other objects based on shape analysis. (c) Nuclei were well separated each other. Distribution of intensity ratios at nuclei is presented in Fig. 3-12(b). I_R

values of nuclei in unlabeled cells were approximately 3/10. On the other hand, the I_R values of the labeled cells were higher than 4.6/10. Therefore, I_R of 4.6/10 is used to discriminate two different cell populations ($I_{RO} = 0.46$).

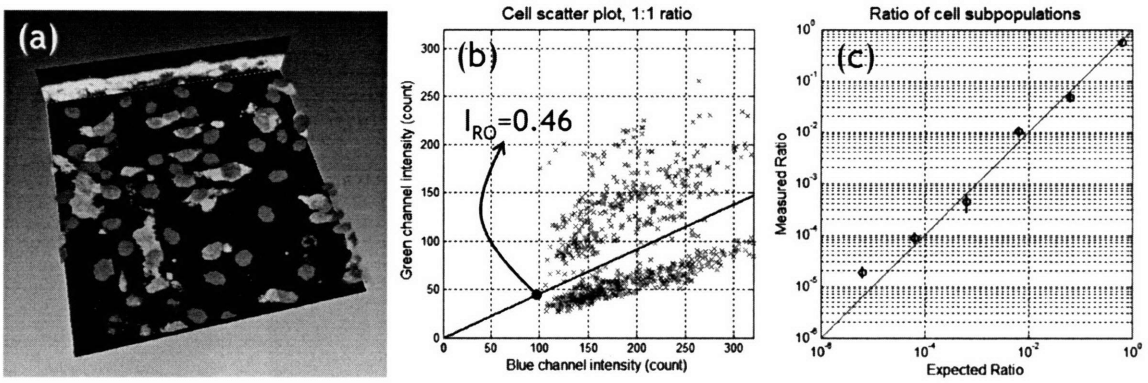

Fig. 3-12: Cell counting in the mixture of two subpopulations in 3D. One group of cells was stained with Hoechst only and the other group was stained with both CellTracker green and Hoechst. Cells were grown in collagen scaffolds to generate 3D cell blocks. (a) is 3D image of 1/1 ratio specimens. Nuclei stained with Hoechst are shown as blue color and the cells stained with CellTracker green also are shown to express green color in their bodies. (b) is cell scatter plot from 1:1 ratio specimens. Two subpopulations are clearly distinguished by the difference in intensity ratio. (c) is the result of cell counting from specimens of different mixture ratios up to $1/10^5$. Measured ratios agree quite well with the expected ratios.

3D segmentation and cell counting algorithm

The basic algorithm for both discriminating and counting cells in two subpopulations is described below.

(1) Conversion of a blue channel (BC) image at one layer to a binary black and white (BW) image based on thresholding: The BC image maps the nucli distributions of both cell population resulted from Hoechst label. The pixels, which have higher intensity than the threshold in the BC image, were assigned with value 1 in the BC-BW image. Other pixels in the BC image were assigned with value 0. The average intensity of the nuclei in the focal plane was approximately 160 and the background noise is less than 10. I_{thresh} was set at 100 so that only the nuclei in the focal plane were captured in the BC-BW image ($I_{thresh} = 100$).

$$\begin{aligned} IM_{BC}^{BW}(ir,ic) &= 1, \quad IM_{BC}(ir,ic) \geq I_{thresh} \\ IM_{BC}^{BW}(ir,ic) &= 0, \quad IM_{BC}(ir,ic) < I_{thresh} \end{aligned} \tag{3-7}$$

(2) Conversion of the green channel (GC) image in the same layer to the BW image. GC image was masked with the BC-BW image. The intensity ratio (I_R) of each pixel was measured in the valid pixels. The pixels which have the higher I_R than I_{RO}, were assigned with value 1, and the pixels, which have lower I_R than I_{RO}, were assigned with value 0 (Fig. 2b).

$$\begin{aligned}
&\text{For pixels } IM_{BC}^{BW}(ir,ic)=1\\
&IM_{GC}^{BW}(ir,ic)=1,\quad \frac{IM_{GC}(ir,ic)}{IM_{BC}(ir,ic)}\geq I_R\\
&IM_{GC}^{BW}(ir,ic)=0,\quad \frac{IM_{GC}(ir,ic)}{IM_{BC}(ir,ic)}< I_R\\
&\text{For pixels } IM_{BC}^{BW}(ir,ic)=0\\
&IM_{GC}^{BW}(ir,ic)=0
\end{aligned} \tag{3-8}$$

(3) Noise reduction with a series of erosion and dilation operations: Erosion operation is logically 'AND' operation among a pixel to be processed and its neighboring pixels. If the value of any neighboring pixel is 0, then the value of the processed pixel becomes 0. The value of the processed pixel becomes 1 only if the values of all the neighboring pixels including the one processed are 1. Therefore, erosion operation can remove noise. Dilation operation is logically 'OR' operation among a pixel and its neighbors. In order to remove noise in BW images, erosion was performed with a disk shape structuring element. Then the size of nuclei shrinks as well as noise was removed. Then, dilation with the same structuring element, which was used in erosion, was performed to restore nuclei sizes.

$$\begin{aligned}
IM1_{BC}^{BW} &= \text{dilation}(\text{erosion}(IM_{BC}^{BW}))\\
IM1_{GC}^{BW} &= \text{dilation}(\text{erosion}(IM_{GC}^{BW}))
\end{aligned} \tag{3-9}$$

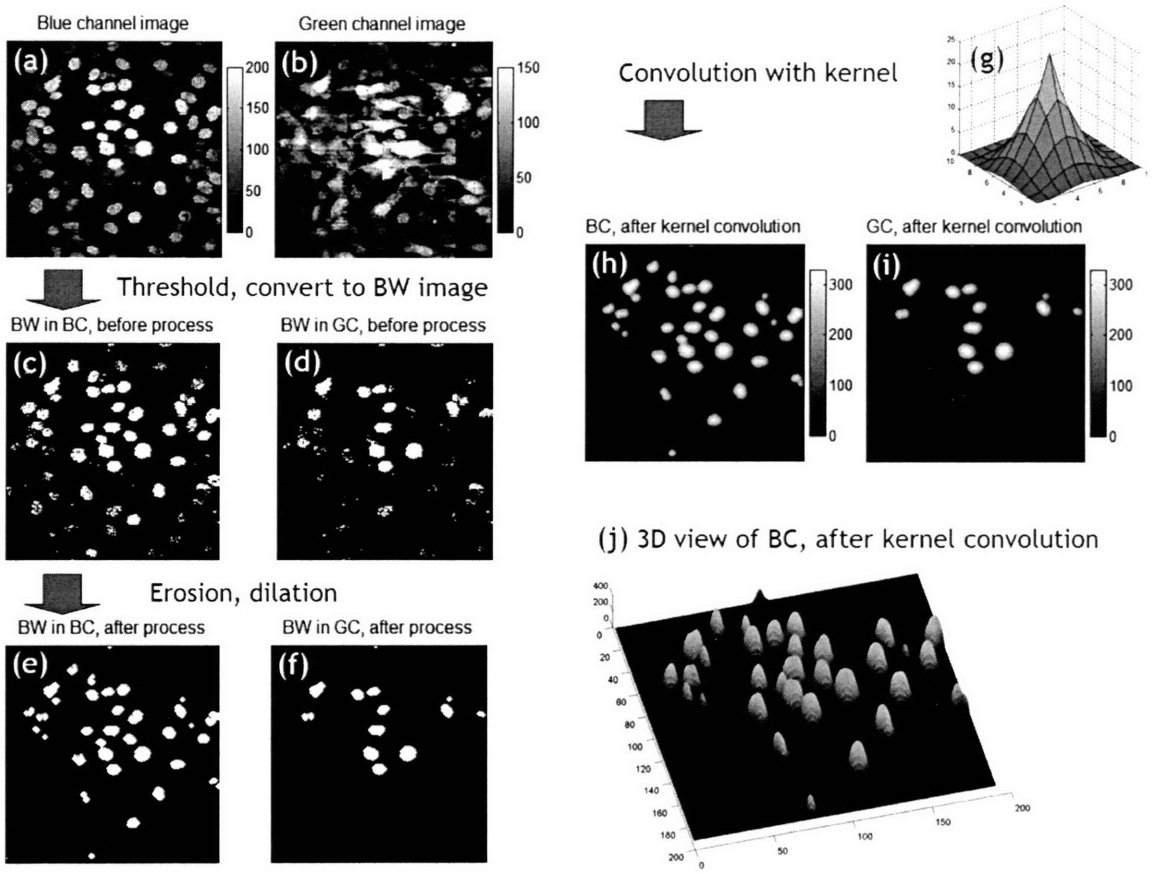

Fig. 3-13: Algorithm for discriminating and counting cell populations, (a) and (b) are raw images, blue channel (BC) and green channel (GC). These images are converted to BW images (c, d) with thresholding on BC images and measuring the intensity ratio in individual pixels. Noise is removed by erosion and dilation operation (e, f). These BW images are convolved with a kernel image (g) to measure locations of nuclei and to count them (h, i). (j) is 3D view of the convolved image (h).

(4) Convolution with a cone shape kernel: In order to find the locations of nuclei, the BW images ($IM1_{BC}^{BW}, IM1_{GC}^{BW}$) was convolved with a kernel which has a cone shape of intensity distribution with the highest intensity at the center. It was noted that convolution operation tends to make the image blurry. Here we assumed that nuclei are separated each other. Also we chose the kernel size smaller than the average size of nucleus in order to reduce the blurring effect.

$$IM1_{BC} = IM1_{BC}^{BW} \otimes IM_K$$
$$IM1_{GC} = IM1_{GC}^{BW} \otimes IM_K \qquad (3\text{-}10)$$

(5) The locations of nuclei were identified after peak finding and masking: After convolution with the kernel image, the images have peak intensities at the center locations of individual nuclei. Maximum finding operation was performed to find the highest peak location. Then an area around the highest peak location was masked with a disk. The area of masking disk was set to be equivalent to the size of nuclei (approximately 17 μm in diameter). Then the next maximum finding operation gave the location of next highest peak (location of next nucleus). The operation of masking with a disk and maximum finding was continued until the peak value is less than a certain value.

(6) The above operation (1-5) was performed in each layer. The continuity of nuclei in the images of several layers was checked by measuring the separation distance among the locations found in the 3D image stack. If two locations are within a certain distance, then they are assumed to belong to the same nucleus and the plane containing the highest intensity value was considered to be the central location of nucleus in 3D.

Counting of control cells, CellTracker stained cells was performed for each data set. Each 3D section of 270 μm × 270 μm × 100 μm contained approximately 70 cells on average. Fig. 3-13(b) is the scatter plot of individual cells from the specimens of 1/1 population ratio. Marks in the plot represent individual cells counted in the analysis. It is clear that two subpopulations are well separated by discriminating with I_R. The intensity ratios from the control cells were well lined up at the ratio of 3/10. Although the I_Rs from the cells, which were stained with both Hoechst and CellTracker green, varied quite a lot, they were all above the I_Rs from control cells. The analysis of cell counting and discrimination was performed in the images from specimens of different population ratios from 1/1 up to $1/10^5$ and the results are presented in Fig. 3-13(c). The measured ratios with image analysis were consistent with the expected ratios.

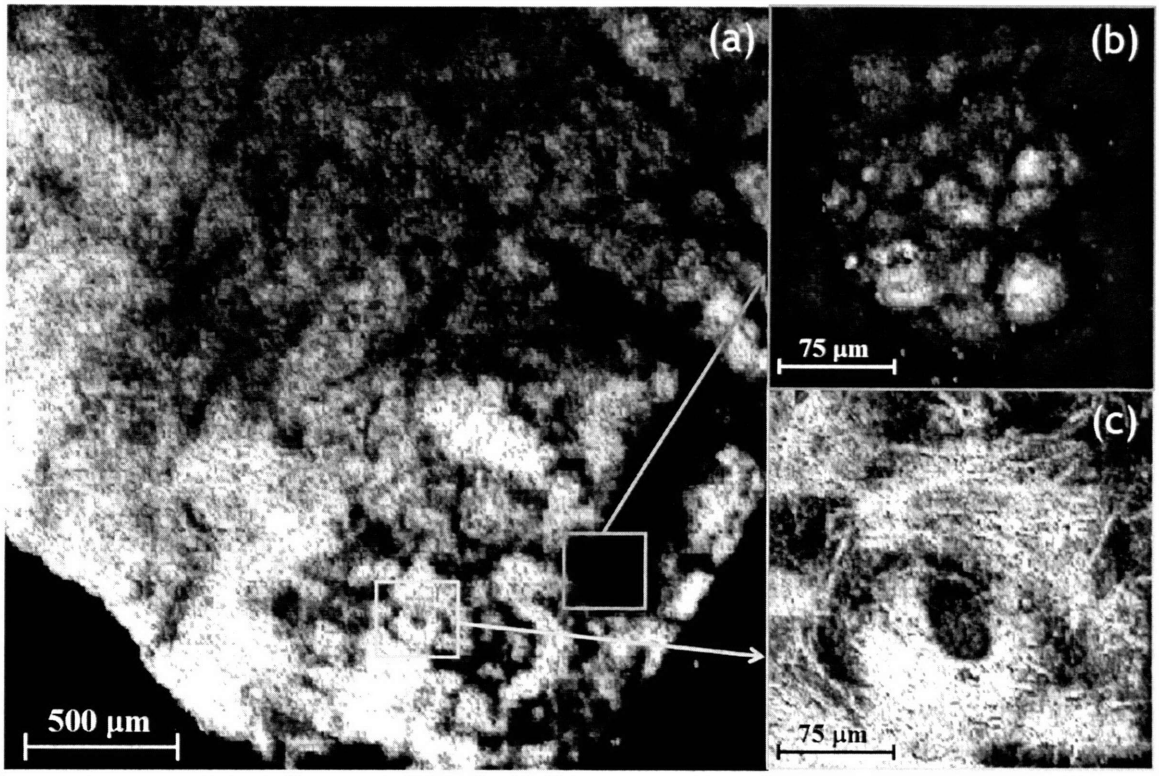

Fig. 3-14: Large section image of ex-vivo human skin in dermal layer. Images are acquired with the high-speed multiphoton microscopy based on polygonal scanner running at 13 frames per second. Collagen and elastin fibers are shown based on their autofluorescence. The size of images is 2.5 mm × 2.5 mm in (a). (b) and (c) are zoomed image from boxed regions of (a). (b) is the image of hair follicle, a cell cluster at the bottom of hair follicle are shown based on their autofluorescence (NAD(P)H). (c) is an image of sweat gland.

B Rare cell detection in ex vivo tissue

The unique capability of this 3D tissue cytometer is to quantify cellular and extracellular matrix states in a complex tissue environment. As a demonstration of this system to quantify tissue structure, an ex-vivo human skin sample was imaged based on its autofluorescence with a single-focus tissue cytometer. The objective used in this experiment was 40 × water immersion (Fluar, NA 1.3, oil; Zeiss, Thornwood, NY). A large section of 2.5 mm × 2.5 mm × 67 μm was imaged. Since the field of view of the microscope is 100 μm × 100 μm only, the large section imaging was performed by moving the specimen with the computer-controlled sample stage, once the 3D imaging of one section is completed. For each section, 50 layers were imaged up to 67 μm deep below the surface. A stitching algorithm was applied to join these images stacks together

to form a large scale tissue image with a subcellular resolution. Fig. 3-14(a) shows the large section image acquired at 67 μm deep bellow the surface. The structure observed in the images corresponds to second harmonic generation and autofluorescent signals from collagen and elastin fibers that are major components of dermal layer. In addition to the extracelluar matrix components, the 3-D tissue cytometry could further image cell clusters at the base of the skin hair follicles (Fig. 3-14b) and in the sebaceous gland of the skin (Fig. 3-14c). This study represents one of the worse imaging conditions that 3D image cytometry may encounter due to the low endogenous signal and the high turbidity of the tissue; we expect most other tissue cytometry studies, which use exogenous fluorophores or fluorescent proteins, will be much easier.

C Detection of recombinant cells

As a demonstration of rare cell detection in situ, we applied the 3D tissue cytometer to study homologous mitotic recombination. Homologous mitotic recombination is a mechanism of DNA repair. In case there is a DNA strand containing damaged regions during replication, it is repaired by replacing the damaged one with a homologous copy of the undamaged strand. This process is beneficial in general because it repairs DNA lesions of many types very accurately. However, it is also risky because significant portion of human genome is comprised of repeated sequence so that the recombination at wrong portion of the DNA is possible. Homologous mitotic recombination is particularly important in carcinogenesis when some cells carry one mutant copy of a tumor suppressor allele and one wild type. In this case, mitotic recombination can incur the loss of wild type allele and promotes for cancer development. Therefore, it is critical to study the mechanism of mitotic recombination and the effect of genetic and environmental factors.

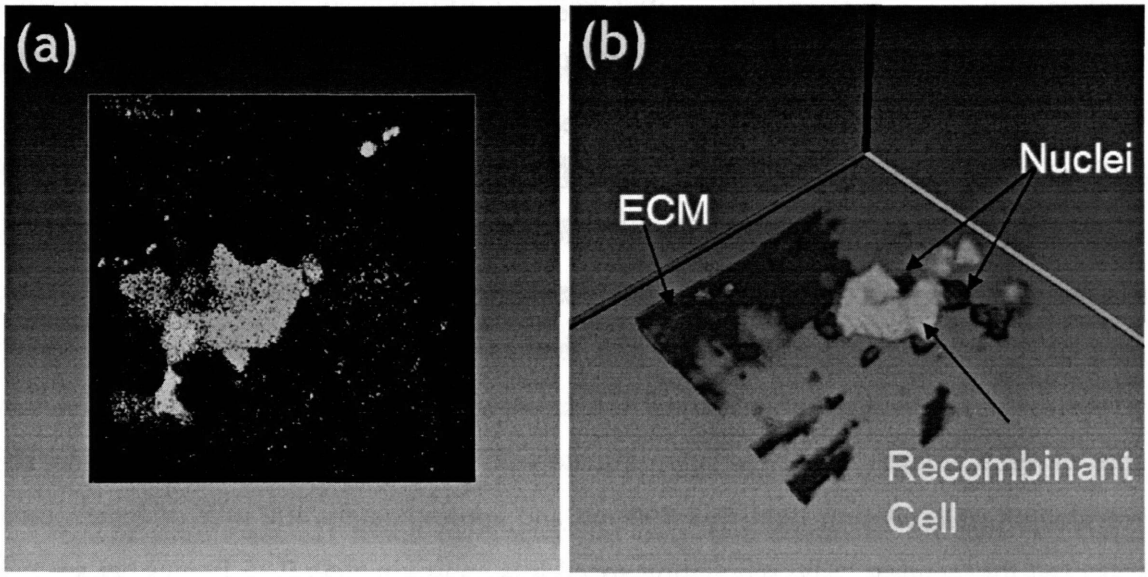

Fig. 3-15: Images of a recombinant cell found in a pancreas tissue from recombomice: trangenic mice which carry EYFP fluorescent markers to detect mitotic recombination event in situ. The tissue is scanned with 3D image cytometer. (a) is a 2D image and (b) is a 3D image reconstructed. Nuclei which are stained with Hoechst appear as blue in the image and the recombinant cell express EYFP (green color) in cytoplasm.

Recombomouse and Tissue Preparation

The development of Recombomouse is previously described in the literature (Hendricks et al. 2004). Cells in these transgenic mice express enhanced yellow fluorescent protein (EYFP) when they undergo mitotic recombination. The natural rate of mitotic recombination is approximate between $1/10^6$ and $1/10^5$ for these mice. The marker is comprised of two truncated enhanced yellow fluorescent protein (eyfp) cassettes, each carrying a different deletion within the EYFP coding sequence. Recombination between the truncated eyfp cassettes can restore full length EYFP, resulting fluorescent phenotype. This mouse line has potential to be used as a sensor for the study of environmental and genetic factors.

3D image cytometry can be used to identify recombinant cells in situ for the study the mechanism of mitotic recombination. It would provide information about the relative susceptibility of different cell types within various organs. In order to study mitotic recombination in situ, a transgenic mice was developed where the recombination of a

particular allele results in the expression of enhanced yellow fluorescent protein (EYFP) in recombinant cells (Hendricks et al. 2003). In this experiment, tissue specimens were freshly excised from the pancreas of a selected transgenic mouse. The excised tissue specimen was further stained in Hoechst/PBS solution for 10 minutes and was placed under a microscopic slide. The tissue specimen was quantified in 3D using the multifocal 3D tissue cytometer. The objective used was 20 × water-immersion with 0.95 NA. Two detector channels were implemented for dual color imaging using a dichroic mirror whose cutting wavelength is 500 nm (DCXR, Chroma technology, Brattleboro, VT). The size of each image stack was approximately 270 μm × 270 μm × 100 μm. The wavelength of excitation light was 890 nm and approximately 400 mW of input power was used for imaging. The acquisition speed was approximately 0.25 frames per second. In our experiments, recombinant cells expressing EYFP were detected and a 3D image of the recombinant cell and its tissue microenvironment is presented in Fig. 3-15. The nucleus of the recombinant cells is shown as blue and its cytoplasm is shown as green. It shows the possibility of detection of rare recombinant cells in tissue based on high throughput 3D tissue cytometry for the first time. It is not completely clear that the detected cells are really recombinant cells. Further analysis is required to verify such as spectrum measurement of fluorescent light or genetic analysis of the cells. Ongoing studies are underway to quantify recombination frequency in various cell and tissue types

D Discussion

Although the 3D tissue cytometer showed a possibility of screening cells inside tissue in situ, its performance can be significantly enhanced by further instrument improvement. First the imaging speed of the multifocal 3D tissue cytometer can be further improved. Currently the speed limitation is from the power limit of available laser light sources. Since multiple foci of excitation light scan specimen in parallel, more input power is required.

We used microlens array to split the excitation light into multiple beams. The excitation light has a Gaussian intensity distribution so that the multiple beams have different intensities (the one from center part of the microlens array has the higher

intensity than the one generated from edge part). Further, the microlens array is rectilinear and the excitation beam has a round shape so that the light illuminating the outside of the square profile is not used. Therefore, there is a significantly waste of excitation light (about 30%). The future addition of a beam splitter can generate multiple beams of uniform powers and improve transmission efficiency (Nielsen et al. 2001).

The MAPMTs used in the current set up has an acceptable quantum efficiency of 20%. This is because the photocathode material in MAPMTs is not optimized. Currently, GaAsP photocathode material can achieve higher QE up to 40% and may be available in the future generations of MAPMT.

The multifocal 3D tissue cytometer has only two channels. A new 3D tissue cytometer with multiple channels for spectral imaging can be easily implemented by modifying the current multifocal 3D tissue cytometer. Multicolor multiphoton microscopy, which is based on MAPMT, was already implemented (Buehler et al. 2005). Multiple color imaging can be implemented by generating a 1D vector of multiple foci instead of the array and by dispersing the emission light with either a grating or a prism and by collecting with multiple channels of MAPMT (Discussed in Section 4.2).

In the analysis of 3D discrimination and counting of cell populations, a very simple algorithm was used. This algorithm works only in case nuclei are well separated each other and there are not much variation in their size and shape. More advanced image processing algorithm needs to be applied in the analysis of real tissue images where nuclei size and shape variation may be significantly larger.

3.3.5 Conclusion

The development of high throughput 3D tissue cytometry first allows the study of cellular and tissue morphological and biological states in situ with subcellular resolution. This technique will significantly expand the scope of cytometry studies to the biomedical problems where cell-tissue interactions are critical.

The high-speed multiphoton microscope with a computer-controlled specimen stage has been adapted as the 3D tissue cytometer. It still retains the advantages of a standard multiphoton microscope: (1) It can images thick specimens in 3D up to few

hundred micrometer deep from the surface, (2) It can images specimen with less photodamage and with subcellular resolution. Its throughput rate is up to approximately 140 cells per second. Therefore, it can be used in the studies which need to investigate a large population of cells in vivo. The wide area image of human skins shows its capability of imaging highly turbid tissue specimens at a high speed based on autofluorescence of tissue components. 2D and 3D cultures of mixed cell populations demonstrates that capability of this system to detect rare cells quantitatively. We showed that cell mixtures of various ratios from 1/10 to $1/10^5$ can be accurately quantified. Rare recombinant cells were detected in tissue specimens using 3D tissue cytometer from Recombomice which carry genetic based fluorescent markers.

3D tissue image cytometry is a new technology. As a new technology, its potential for biomedical research is still far from fully explored. In the short term, we have identified a number of immediate applications. We are exploring the application of 3D tissue image cytometry to study two aspects of cancer biology. The first aspect is cancer progression. The process of how cancer cells extravasate through blood vessel walls and expand to form metastatic cancer at distant organs is far from completely understood. We are exploiting 3D tissue image cytometry to explore questions such as the distribution of these cancer cells on the organ level and the spatial relationship of these metastatic cancer cells with the organ vasculature. This technology further allows us to study the time course of cancer cell clearance rate from the vascular system and provides temporal information on the growth rate of the metastatic tumors. Other interesting areas of application include neural biology where we are exploring the potential application of this technology to quantify neuronal connectivity as a function of animal development, stem cell research where we are mapping stem cell distribution in organs and examining the process of adult stem cell division in animals, and tissue engineering where we are examining cellular differentiation and organ formation in situ.

In addition to these immediate applications, we believe that 3D tissue image cytometry is critical to modernize histopathology. While histology is a clinical gold standard, it is far from a quantitative science. Unlike cytology where automation and quantitative is making significant progress as in automated Pap test, there are little parallel efforts in the quantification of histological data. The lack of major attempts in

the quantification of histological data is partially due the fact that image classification and recognition in complex tissue setting is significantly more challenging computationally than in cell cultures. Another problem lies in many data base driven classification algorithms requires a large quantity of tissue images data as training sets which is not readily available today. However, with the advent of 3D tissue image cytometry, a large quantity of tissue digital images can now be readily acquired. Clearly, the next step lies in developing efficient recognition and classification algorithms needed to extract diagnostic information from these images.

Finally, with the quantification of histology, one may envision that tissue physiology and pathology can be better understood through modern genomic and proteomic analysis. Combining high through 3D tissue image cytometry with the ability to map gene and protein expression profiles, physiological models may be developed based on the underlying molecular and cellular process. These physiological models may allow us to understand how tissue structure is affected genetic and protein expression variations. An early example of this type of analysis may be found in areas such as cancer development. Cancer is a disease which has a very strong spatial component to its etiology (Liotta et al. 2001). Cancer cells can invade the stroma of the surrounding tissue and recruit non-malignant cells to differentiate and support the growing tumor. The arrangement of normal tissue boundaries becomes pathogenic as the expression profiles of the surrounding cells are altered by cell signaling from the malignant cells (Gohongi et al. 1999; Knezevic et al. 2001; Leethanakul et al. 2003). The application of 3D tissue image cytometry to simultaneously map tissue morphology, gene and protein expression patterns may allow us to better understand this important pathological process.

Chapter 4

Incorporating complementary modalities with two-photon microscopy

TPM provides the spatial distribution of fluorophores in tissues. Confocal reflected imaging provides complementary structural information based on refractive index variations in tissue. Combining TPM and confocal reflected imaging provides a novel approach to study tissue structure and biochemistry. Further, the ability of two-photon microscope to investigate biochemical microenvironment in cells and tissues can be significantly enhanced by the incorporation of emission spectral resolved imaging. A multi-color multiphoton microscopy has been developed that captures the emission spectrum from each pixels in the three dimensional imaging volume of the specimen.

4.1. Two-photon fluorescence and confocal reflected light imaging of thick tissues

4.1.1. Introduction

An assessment of tissue physiological states requires morphological information with sub-cellular details which is traditionally acquired from histological sections of excised tissue. Much of the cellular biochemical information is lost during this surgical and fixation processes. Clinically, the biopsy procedure is also undesirable due to its invasive nature. The development of a non-invasive optical technology that can acquire both cellular structural and biochemical signals from within deep tissue will bring major advances in clinical diagnosis technology (Masters et al. 1998). The technology of two-photon excitation has opened a window of opportunity for developing non-invasive medical diagnostic tools capable of monitoring biochemical states of thick tissue (So et al.

2000)s. Using cellular endogenous chromophores, 3- nicotinamide-adenine dinucleotide phosphate (NAD(P)H), the cellular metabolic rates in living human skin were determined (Masters et al. 1997). Although important functional information can be obtained from the fluorescence spectroscopy of endogenous chromophores, these chromophores are rather poor contrast enhancing agent for mapping cellular morphology (So et al. 2000). First, most endogenous chromophores are confined to the cellular cytoplasm which prevents the visualization of other cellular organelles. Second, there is significant variability in the distribution and the quantum yield of endogenous chromophores which depends on tissue biochemistry so that it prevents consistent comparison of cellular morphology (So et al. 2000). On the other hand, the deep tissue cellular morphology has been imaged with excellent subcellular resolution using reflected light confocal microscopy (Rajadhyaksha et al. 1995). In reflected light microscopy, the image contrast originates from the index of refraction differences of the cellular structures. The organelle boundaries with significant index differences such as the plasma membrane and the nucleus envelop can be consistently visualized. A combination of morphological and functional information is required for a thorough tissue study. This report describes the development of a new microscope which is capable of simultaneously collecting both two-photon fluorescence and confocal reflected light signals. Promising biomedical applications include the non-invasive diagnosis of skin cancer and the study of wound healing.

In reflected light mode, confocal microscope have been very successful in imaging thick, highly scattering tissues. Reflected light confocal systems have a comparable penetration depth as two-photon fluorescence system and provide complementary structural information. This confocal principle has been exploited in a real-time, slit scanning, confocal microscope that is used clinically for optical biopsy and diagnostics in ophthalmology. The tandem-scanning confocal microscope, which operates in real-time, was developed by Petran and co-workers to image optical sections of thick, highly scattering biological materials (Petran et al. 1968). Corcuff and co-workers have adapted the tandem scanning confocal microscope for in vivo skin imaging (Corcuff et al. 1993). Another implementation of reflected light scanning laser confocal

microscope has been successful developed for video rate imaging of skin in vivo (Corcuff et al. 1993; Rajadhyaksha et al. 1995).

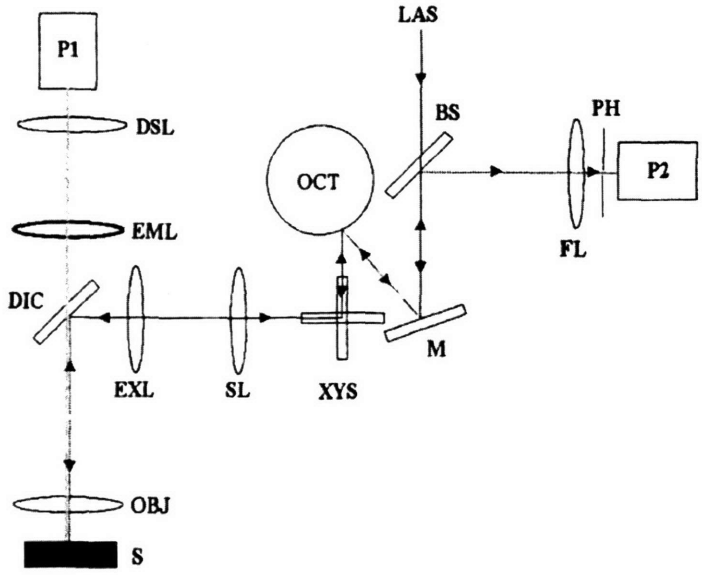

Fig. 4-1: Partial schematic of the proposed deep tissue microscope including an octagonal mirror system for fast scanning and a reflected confocal beam path: S - sample, OBJ - objective, DIC - dichroic mirror, EXL -excitation tube lens, SL - scan lens, XYS - x-yscanner, M - mirror, OCT - octagonal mirror scanner, BS - beamsplitter, FL - focusing lens, PH - pinhole aperture, LAS - laser light source, EML - emission tube lens, DSL - de-scan lens, P1 - fluorescence PMT, P2 - confocal PMT. Thin black doted lines denote infrared excitation and reflected light signal. Thick gray solid lines denote fluorescence signal.

4.1.2. Design of a two-photon fluorescence and confocal reflected light deep tissue microscope

Confocal reflected light imaging can be easily incorporated in the existing two-photon microscope with no loss in detection sensitivity of the fluorescence signal. In the original two-photon microscope design, the infrared photons reflected by the sample are rejected and lost at the dichroic mirror. An additional confocal detection path can be added onto the excitation beam path to gather and retain these reflected infrared excitation photons (Fig. 4-1). The reflected photons collected by the objective are collimated by the excitation tube lens and the scan lens combination. The collimated beam is de-scanned by being sent backwards through the x-y scanner and the octagonal

mirror. This stationary beam can then be focused by a lens through a confocal pinhole aperture onto a fast silicon photodiode (PDA5O, Thom Labs, Newton, NJ). After this system has been optimized, a high sensitivity avalanche photodiode (Advanced Photonics, Camarillo, CA) will be used. The photodiode used has an internal transimpedance amplifier with a maximum gain of 2×10^6 V/A. The voltage output is send into a 16 bit, 10 kHz analog-to-digital converter (DAQCard-Al-16XE-lO, National Instrument, Austin, TX) in the control computer. The data acquisition of the single photon counting circuitry for the fluorescence signal and the A/D converter for the reflected light signal are synchronized by a custom interface circuit. Note that the two-photon fluorescence system is unaffected by this addition except for a factor of two loss in the excitation power at the input beam splitter. This loss can be easily compensated by increasing the initial power of the laser beam.

4.1.3. Results and discussion

Simultaneous two-photon fluorescence and confocal reflected light imaging were performed on two samples. The first one is comprised of 15 μm fluorescent latex spheres (Molecular Probes, Eugene, OR) immobilized in agraose gel (Fig. 4-2). Images were taken both at a plane passing through the sphere center and at a plane 6 μm above. The images obtained are as expected. In the two-photon image, signal is observed throughout the interior of sphere corresponding to the expected chromophore distribution. In the confocal image, signal is seen at the boundary between the sphere and the gel where there is a significant change in the index of refraction. Strong signal is also observed at the center of the sphere which seems to result from the lens effect of the sphere. The defocusing of both two-photon and confocal images as the focal plane moves by 6 μm from the sphere center is expected from the depth discrimination capability of both the two-photon and the confocal imaging methods.

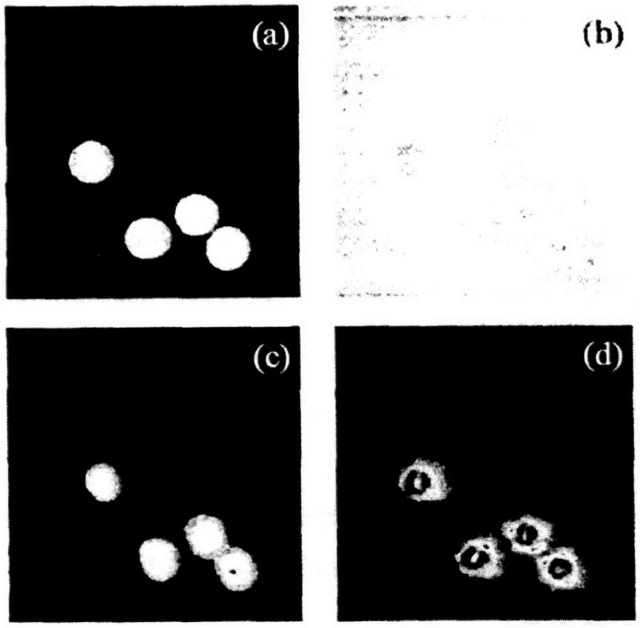

Fig. 4-2: Simultaneous two-photon fluorescence and confocal reflected light images of 15 1um latex spheres. (a) and (b) are two-photon and confocal images of the spheres with the sample plane positioned at the center of the spheres. (c) and (d) are two-photon and confocal images of the spheres with the sample plane positioned at the top of the sphere (about 6 μm above the center)

Frozen human skin tissue was imaged using both two-photon fluorescence and confocal reflected light imaging (Fig. 4-3). The freeze-thaw process has caused some degradation of the tissue structure but two-photon imaging has resolved fibrous structures possibly corresponds to elastin or collagen structures at a depth of about 100 μm below the skin surface. Dramatically different structures were observed simultaneously using confocal reflected light imaging. While the physiological origin of the structures remains to be verified by histology, it is clear that confocal imaging provides an important complementary view.

4.1.4. Conclusion

We have demonstrated that simultaneous two-photon fluorescence and reflected light confocal imaging can be achieved in deep tissue and has potential to provide important complementary information.

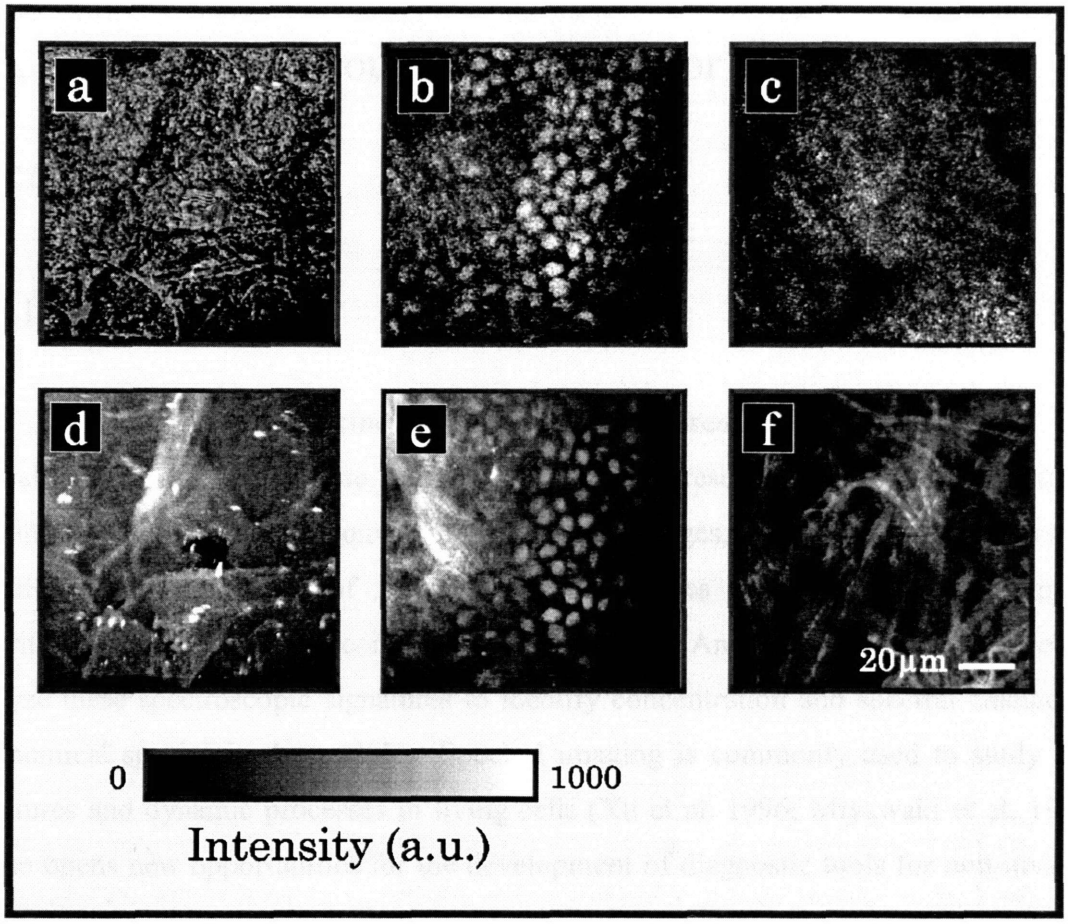

Fig. 4-3: Simultaneous confocal reflected (a) - (c) and two-photon fluorescence (d) – (f) images of frozen human skin. Stratum corneum layer in (a) and (d), basal cell layer in (b) and (e), and dermal layer in (c) and (f).

4.2. Single-photon counting multi-color two-photon microscope

4.2.1. Introduction

In biology and medicine, spectroscopic measurement can be combined with optical microscopy to generate images with spatially-resolved biochemical functional information. In contrast to conventional intensity images, spectral imaging allows the quantitative determination of spectroscopic signatures of objects. Chemometric algorithm such as principal component analysis(J. J. Andrew 1998) can be used to analyze these spectroscopic signatures to identify concentration and spectral changes of biochemical species in the sample. Spectral imaging is commonly used to study both structures and dynamic processes in living cells (Xu et al. 1996; Miyawaki et al. 1999). It also opens new opportunities for the development of diagnostic tools for non-invasive tissue studies and may assist in the identification of malignant cells and the determination of surgical margin (Gillenwater et al. 1998). Active research in spectral imaging development reflects the scientific and clinical potential of this approach. This paper describes the development of a spectrometer with single-photon counting sensitivity based on multi-anode photomultiplier tubes. The incorporation of the spectrometer into the multi-photon microscope is suitable for highly-sensitive, spectrally-resolved, three-dimensional imaging of cell and tissue specimens.

A Spectral imaging techniques

The design goals of a high-performance multi-photon spectral imager for deep tissue specimens are single-photon sensitivity, maximum light throughput (collection efficiency), adequate spectral resolution to distinguish chromophores (a few nanometers), and high-speed data acquisition. The components that directly affect the performance of the instrument are the spectral-resolving devices, photodetectors, and their readout

electronics. Spectrally-resolved imaging aims to record a multi-dimensional data set in which each voxel (volume-element) is defined by its spatial location (x, y, z) and its spectral signature (λ). Such a data set is often referred to as an image cube, a hyper cube, or a λ-stack (analogous to a z-stack of x-y image planes). Since photodetectors are at best two-dimensional, the acquisition of an image cube requires scanning in position and/or in wavelength. Consequently, image cubes are built progressively in two ways. 1) An image cube is generated by sequentially recording a series of two-dimensional wide field images at both different spectral bands and different depths. 2) The entire emission spectrum is acquired for a single spatial point or a line; and the image cube is then completed by sequential spatial scanning. As described subsequently each method has its unique advantages and disadvantages.

B Spectral-resolving devices

The two approaches for image cube generation require different spectral-resolving devices: band-pass devices and spectral dispersive devices. Band-pass devices include band-pass filter wheels, or electrically tunable filters. The typical spectral dispersive devices are prisms and gratings. Mechanical filter wheels are the most common band-pass devices. A complete spectral data set is recorded by mechanically placing filters of different pass bands into the imaging light path. The spectral resolution and transmission efficiency is determined by the filter type used. Typical efficiencies of holographic bandpass filters are approximately 70-80 %. Since the filters are exchanged mechanically, the data acquisition is slow and strictly sequential in terms of wavelength scanning. Electrically tunable filters such as liquid-crystal tunable filters (LCTF), or acoustic-optical tunable filters (AOTF) are alternative band-pass devices that provide fast (micro- to milliseconds) and random switching through a sequence of wavelengths (E. S. Wachman 1996; H. R. Morris 1996). A typical LCTF employs a stack of polarizers and birefringent liquid crystal plates that act as voltage-tunable retarders. The transmission efficiency of LCTFs is approximately 40% accross the VIS and near-IR spectral range but can drop to a few percent in the near-UV. AOTFs are solid state electro-optical devices and apply radio frequency (RF) acoustic waves in dielectric materials to diffract one (or a few) specific wavelengths of light. The performance characteristics of AOTFs

is comparable to that of LCTFs, *i.e.* AOTFs have transmission efficiencies of approximately 40 % (VIS to near IR), pass bands of a few nanometers, and sub-millisecond switching speed. Spectrally dispersive devices spread out spatially the spectral components of the incident light. Due to their higher dispersive power, gratings are used more frequently than prisms. Spectrographs are grating-based devices and provide a full spectrum at their exit ports. Commercially available gratings cover the spectral range from soft X-rays to IR. Gratings typically provide spectral resolutions well below 0.1 nm, and transmission efficiencies of more than 80 % at the peak wavelength. Since multi-photon microscopes typically generate an image by raster scanning a single excitation spot, the use of spectrally dispersive devices is more appropriate for this type of microscopy. Incorporating single band-pass devices in multi-photon microscopes is relatively wasteful in terms of photon collection efficiency because out-of-band photons are attenuated and discarded. In contrast, parallel, spectrally dispersive devices are more efficient because the entire spectrum from the excitation volume is recorded with a minimal loss of photons. Therefore, a spectrograph with a holographic grating is used as spectral resolving device in our multi-color multi-photon fluorescence microscope.

C Photodetectors

The selection of an appropriate photodetector is critical. Typical selection criteria are spectral range, quantum efficiency (QE), electronic noise level, readout speed, single versus array detectors, and cost. Commonly used detectors are photomultiplier tubes (PMTs), avalanche photodiodes (APDs), charge coupled device (CCD) cameras, and intensified CCDs (ICCDs). Particularly promising detectors for imaging spectroscopy in multi-photon microscopes are multi-channel derivatives of standard PMTs and APDs: the multi-anode PMT and the multi-pixel APD. Table I summarizes the characteristic performance of the various detectors mentioned above.

	mA - PMT	CCD	ICCD	mP - APD
QE	~ 25 %	~ 80 %	~ 40 %	~ 50 %
λ – Range	UV - NIR	VIS – IR	UV – VIS	VIS - IR
Noise	Low	Low	High	High
Sensitivity	Single photon	Few photons	Single photon	Several photons
Speed	Fast	Slow	Slow	Fast
Cost	$,$$$.-	$$,$$$.-	$$,$$$.-	$,$$$.-

Table 4-1: Typical performance characteristics of four types of photodetectors: multi-anode PMT (mA-PMT), charge coupled device (CCD) cameras, intensified CCDs (ICCD), and multi-pixel avalanche photodiodes (mP-APDs). QE: quantum efficiency.

CCD cameras have become the detectors of choice in standard spectrometers and high-speed imagers including the multifocal multiphoton imaging microsope (J. Bewersdorf 1998). Back-thinned CCDs can achieve QE > 70% for photons in the near-UV to near-IR spectral range. Note that front-illuminated CCDs generally provide QE ≈ 30-40% and have low UV sensitivity. Due to the lack of internal gain and the presence of readout noise in the output circuitry, CCD cameras are not single-photon sensitive. Alternatively, intensified CCDs can achieve single-photon sensitivity using appropriate 2-D intensifier tubes (*e.g.* micro-channel plates) in front of the standard CCD chip. The QE is approximately 40% and limited by intensifier cathode sensitivity. The major noise sources of ICCDs are the electronic noise from the intensifier tube and the multiplicative noise from the amplification processes. ICCD cameras are relatively expensive. Recently CCDs with 'on-chip multiplication' have been available with high QE (90 % in visible range) and high-speed readout speed (10 MHz). Signals are amplified before readout stage so that the effect of readout noise is eliminated. While these cameras are similar to ICCDs, these have a much higher quantum efficiency. In principle, both ICCDs and CCDs with on-chip multiplication are excellent detectors for spectrally-resolved imaging applications. Unfortunately, both type of CCD systems are quite expensive.

PMTs are the most commonly used detectors due to their high sensitivity and relatively low costs. PMTs are single photon sensitive. The internal PMT gain is on the order of 10^6. The minimal detectable light level for PMTs is determined by their dark current which is typically at the pico- and femto-ampere level at room and cryogenic temperature, respectively. Typical PMTs have broad dynamic range and remain linear over eight orders of magnitude. The use of PMTs at high photon rate is limited by dynode loading and damage. When operated in their most sensitive spectral domain, *i.e.* the blue/green wavelength regime, PMTs provide fairly good quantum efficiencies of 20-40%. However, for wavelengths above 600 nm, their efficiencies can drop below 1%. Traditional PMTs are single pixel devices. Multi-anode PMTs have been developed where the anode of a standard PMT is subdivided into an array of separate sensitive areas (multi-pixels). Compared with their single-anode counterparts, multi-anode PMTs show very similar performance in terms of spectral sensitivity and readout speed, but they exhibit slightly higher dark count rates and there is crosstalk (2%) between adjacent anodes according to the specification from the manufacturer. Multi-anode PMTs are single-photon sensitive. With these features, several spectral imagers have been developed based on multi-anode PMTs (Pan et al. 2001; Becker et al. 2002; Dickinson et al. 2002; T. Haraguchi 2002). The comparison of these systems is in the next section.

For higher sensitivity detection in the VIS and NIR range, avalanche photodiodes (APDs) with silicon-based cathodes are excellent. Throughout the visible range they have quantum efficiencies of about 70%. The drawbacks of APDs are their high cost and failure rate. In addition, commercial multi-pixel APDs cannot be manufactured with sufficiently low noise to achieve single photon sensitivity. Based on Table I, we conclude that multi-anode PMTs provide all the necessary performance to achieve the best balance between sensitivity, readout speed, and cost for spectrally resolved multi-photon imaging. The current drawback of multi-anode PMTs are their lower quantum efficiency of about 20%, although new multi-anode PMTs with photocathodes approaching quantum efficiencies of 40% are being developed according to the manufacturer.

D Detector readout electronics

Readout electronics for APDs and PMTs can be classified into two categories: analog detection and pulse counting devices. The output signal from the light-exposed detectors is a sequence of current pulses generated by the incident photons. Since these current pulses have finite duration, on the order of nanoseconds, significant overlap of the current pulses occurs when the signal level is high. In this case, analog detection is appropriate and the integrated current output is measured. At low light intensity, that is, when the incident photons generate well-separated current pulses, the pulse counting method is appropriate. The number of output pulses is strictly proportional to the amount of incident light. Furthermore, the detector noise can be effectively discriminated and readout is not affected by multiplicative noise. Thus, pulse counting has advantages in terms of signal-to-noise ratio (SNR) and stability over the analog pulse-averaging approach. Recently, analog readout electronics have been developed for multi-anode PMTs and have been incorporated into multi-photon fluorescence microscopes for a broad range of biomedical applications (Pan et al. 2001; Dickinson et al. 2002; T. Haraguchi 2002). However, the performance of these devices may be further optimized with the increase of detection sensitivity using single-photon counting scheme, the minimization of dead time in signal acquisition, the increase of data transfer rate to the host computer (C. Buehler 2002).

We chose to implement single-photon-counting readout electronics for multi-anode PMTs to optimize the performance of the spectrally resolved microscope for many biomedical applications where the signal level is typically low. Using advanced high-speed electronic components (broadband GHz amplifiers, re-configurable logic), we developed a multi-channel photon counting card (mC-PhCC) allowing fully parallel single-photon counting across all its channels. Rate-matching 'first-in-first-out' (FIFO) data buffers serve as temporary on-board data storage queues to account for the different clock rate of the data acquisition computer. The mC-PhCC is especially designed for efficient readout of multi-channel PMTs. For each detection channel, the signal remains linear for photon rates up to 10^8 counts per second (cps). Correspondingly, the high-speed data interface provides ample bandwidth to transfer λ-stacks of 16 spectral channel,

256×256 pixel images with 12-bit dynamic range at 30 frames per second to the host computer.

The essential building blocks of the mC-PhCC are field programmable gate arrays (FPGA). These re-configurable logic devices offer both hardware speed and software flexibility. In contrast to standard electronic components, the functionality of FPGAs is defined, and thus modifiable, by programming. State-of-the-art manufacturing processes of FPGAs support true system-on-chip (SOC) designs, *i.e.* the implementation of a complete electronic system on a single chip. The SOC platform can incorporate microprocessor(s), memory blocks (*e.g.* dual ported RAM), and various pre-defined I/O modules (*c.f.* intellectual properties: IPs) that allow the FPGA to connect directly to common interfaces including PCI, USB, CAN, and most recently, high-speed serial links.

Another implementation of single-photon counting spectral-resolved imager using multi-anode PMTs has been reported (P. Tinnefeld 2001; Becker et al. 2002). This excellent system features spectral resolution with time-correlated single photon counting (TCSPC) circuitry. As a comparison, the TCSPC system can provide pico-second precision lifetime information to complement spectral measurement. However, since there is only a single channel of time-correlated single photon counting circuit implemented, photons arriving at different spectral channel within the electronic dead time of the detection circuit are rejected. In contrast, the mC-PhCC system is fully parallelized and can detect photons arriving simultaneously at multiple spectral channels. The photon detection speed of mC-PhCC system is only limited by the dead time of each individual channels which is approximately 80 nanoseconds. The dead time can be eliminated by alternating two photon counters in each channel.

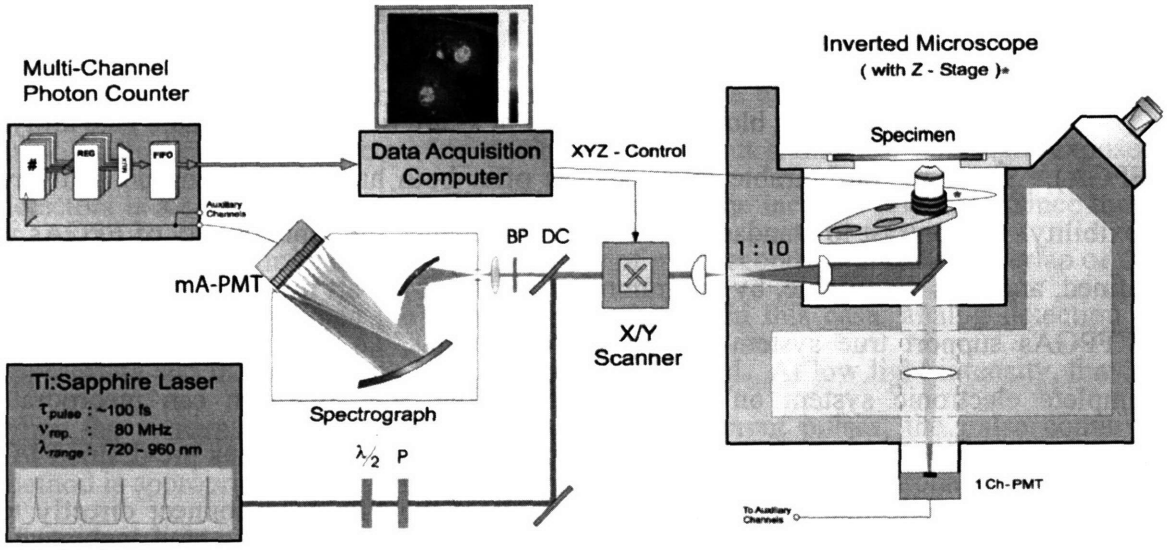

Fig. 4-4: Schematic diagram of the multi-color multi-photon fluorescence microscope. M : mirror, DC : dichroic mirror, BP : band-pass filter, λ/2 : half-wave plate, P : polarizer, mA-PMT : multi-anode PMT

4.2.2. Experimental apparatus and description

A Experimental setup

The schematic of the multi-color multi-photon fluorescence microscope is shown in Fig. 4-4. The excitation light source is a mode-locked titanium-sapphire pulsed laser with about 100 femtosecond pulse width (Mira 900, Coherent Inc., Palo Alto, CA). The excitation wavelength (λ_{ex}) is tunable from 700 nm to 960 nm. Both the polarization and the power of excitation light at the specimen are controlled by a half wave plate (λ/2) and a Glan-Thomson polarizer (P). Typically, tissue imaging is conducted with an average laser power of about 3 to 30 mW at the sample plane. A computer-controlled galvanometric x-y scanner (6350, Cambridge Technology, Watertown, MA) deflects (raster-scans) the laser beam across the specimen. The excitation beam is coupled into an inverted microscope (Axiovert 100TV, Zeiss Inc., Thornwood, NY) via a modified epi-luminescence light path. A 1:10 beam expander ensures that the beam overfills the objective's back aperture to achieve diffraction limited focusing. Imaging at different depths is accomplished using a piezo-driven objective translator which moves the

microscope objective perpendicular to imaging plane (P-721.00; Physik Instrumente, Waldbronn, Germany).

The generated fluorescence light is collected by the same objective. To ensure a spatially and angularly stationary emission beam at the entrance port of the spectrometer the fluorescence beam is de-scanned by sending it back through the microscope's excitation light path and the x-y scanner mirrors. After the scanner the emitted light passes a dichroic mirror (DC; 675DCSX, Chroma Technology Inc., Brattleboro, VT), and the residual excitation light is blocked by a barrier filter (BP; ESP650, Chroma Technology, Brattleboro, VT). The spectral dispersion of the fluorescence signal is achieved via a spectrograph (77400, ORIEL Instruments, Stratford, CT). A holographic grating (77414, ORIEL Instruments, Stratford, CT) blazed at 400 nm is used, and its efficiency is 85 % at the blaze wavelength. The grating's 600 line/mm ruling provides sub-nanometer resolution. Since it is more important to maximize the optical throughput, and since the limited number of PMT channels does not requires the full spectral resolution of the grating, the grating surface is only partially illuminated by the emission light. At the output focal plane of the spectrograph, the spectral width of emitted light spans approximately 330 nm. Its center wavelength is adjustable by rotating the grating via a micrometer. The fluorescence spectrum is detected by a 16-anode PMT (R59000U-00-L16, Hamamatsu, Bridgewater, NY), mounted onto a socket assembly with an integrated voltage divider network (E6736, Hamamatsu, Bridgewater, NY). The biasing voltage used is 800 V. Direct coupling of the PMT to the spectrograph provides a spectral resolution of 10 nm over a wavelength range of 160 nm. Higher spectral resolution can be achieved by the insertion of relay optics or the incorporation of a 32-anode PMT array (H7260, Hamamatsu, Bridgewater, NY). The sixteen analog signals from the multi-anode PMT are read out by the mC-PhCC which is described in detail in the next section.

B The multi-channel photon counting card

The design of the multi-channel photon-counting card (mC-PhCC) is shown schematically in Fig. 4-5. The base-module of the mC-PhCC incorporates eighteen

independent photon-counting channels, deep on-board buffers for short-term data storage, and two alternative high-speed interfaces to the host computer (SUB-D, GigaStar). The building blocks of the photon-counting channels are the high-speed amplifier/discriminator stages, the pulse-shaping circuitries ('one-shot'), the pulse counters (#), and their associated hold registers (REG). A set of TTL signals provide full control of the mC-PhCC, in particular, the synchronization of the data acquisition and readout procedure with the pixel-to-pixel movement of the scanner. Furthermore, the modular design of the mC-PhCC allows extending the number of channels for PMTs of more anodes.

All input channels are 50 Ohm terminated to minimize signal reflection. Typical photon-induced PMT signals are pulse trains with approximately five nanosecond pulse duration and pulse peak voltages in the tens of mV-range. The PMT signal is pre-amplified by a monolithic broadband amplifier (MAR8, Mini-Circuits, Brooklyn, NY). Both the amplifier's low noise figure and its high gain (23dB at 1 GHz) allow for precise discrimination of photon-induced pulses by a comparator with single threshold level (MAX999, Maxim Integrated Products Sunnyvale, CA). The threshold can be adjusted by a 25-turn potentiometer ($\Delta V \approx 1$ Volt). Typically, the voltage difference between the comparator's differential input pins is set to be approximately 60 mV. The duration of the discriminated photon-pulses varies significantly as a result of the PMTs broad pulse height distribution. To account for the occasionally occurring runt pulses, and their unpredicted effects on digital logic gates, each comparator output triggers a 'one-shot' pulser that generates a (well-defined) pulse of 4 ns width. The 'amplifier/discriminator/one-shot' circuitries exhibit no cross-talk and can cope with periodic pulses at rates exceeding 100 MHz. To minimize the number of components, the 'one-shot' pulsers are implemented in the FPGAs.

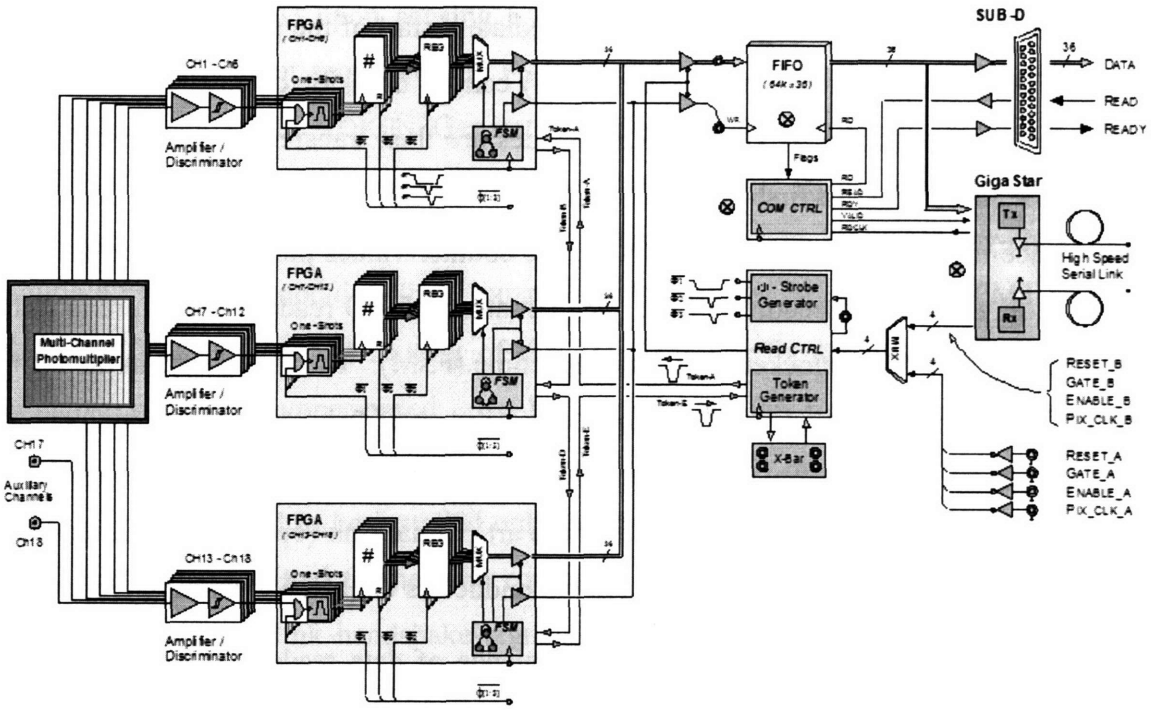

Fig. 4-5: Schematic diagram of the multi-channel photon counter card (mC-PhCC). Photon pulse signals from the multi-anode PMT are recorded by 18 photon counting channels. Each channel comprises of amplifier/discriminator, one-shot, counter(#), and hold register (REG). Collected data are transferred to the temporary data storage (FIFO) in channel sequence and then transferred to the host computer either via either a parallel link (SUB-D) or high speed serial link (GigaStar). The signals RESET, GATE, ENABLE, PIX_CLK are driven by the host computer and allow the scanner to be synchronized with the data acquisition and readout procedure of the mC-PhCC. A detailed description of the mC-PhCC is given in text.

The digital circuitry of the mC-PhCC is based on field-programmable gate arrays (FPGA). The actual FPGA (XCS30XL, Xilinx, San Jose, CA) has been selected primarily for its large number of global clock lines (eight), and its cost effectiveness. The global lines are low skew routing resources (< 2 ns) and thus ideally suited for designing high-speed counters (#) running above 125 MHz. The dynamic range of the eighteen counters is set to 12 bit, but it can be easily adjusted (re-configured) to accommodate other experimental requirements. Typically, the measured fluorescence signal barely exceeds a few hundred photon counts per pixel (256 × 256 pixel image acquired for 7 s), thus, 12-bit counters are adequate for most fluorescence applications. The design of the eighteen photon counters is split into three identical FPGAs. Each FPGA comprises six 'one-shot' pulsers that drive the clock inputs of six 12-bit counters. To reduce the dead-time of the mC-PhCC, the counter values are all copied in parallel to intermediate 18-bit

data registers (REG), allowing for almost immediate restart of the photon counters. The six supplementary REG-bits (high bits: 13 - 18) can be used for channel identification. Using three 3:1 multiplexers (MUX) REG-values are then transferred sequentially to a deep 64k × 36-bit 'first-in-first-out' data buffer (FIFO: CY7C4285V, Cypress, San Jose, CA). Since the width of the FIFO is 36-bit, the counter values plus their IDs are stored pair-wise in a channel-ascending order. The counter-to-FIFO readout procedure is fully controlled by a 40 MHz-clocked finite state machine (FSM). The data stored in the FIFO queues can be transferred to the host computer via two alternative high-speed communication interfaces: a simple, parallel link with ribbon cables for short-range (≈3 m) data transfer, and a gigabit, 'state of the art', serial link (optical or electrical) for wide range data transfer (GigaStar, Inova Semiconductors GmbH, München, Germany).

This section describes in detail the sequence of data readout in the mC-PhCC. Again, the mC-PhCC is fully controlled via the four TTL signals reset, enable, gate, and PIX-CLK (pixel clock). They are provided by the host computer either via separate connectors (c.f. postfix '_A') or via the high-speed serial link (c.f. postfix '_B'). The mC-PhCC data readout sequence is trigged by PIX-CLK (rising edge & enable = '1') and encompasses 1) immediate disabling of all counters, 2) simultaneous copying of all counter values into their individual hold registers (REG), 3) resetting and re-enabling all counters, 4) transferring the REG-values to the FIFO, and 5) signaling the end of the readout sequence to the host computer by asserting data ready (RDY and VALID). Steps 1) through 3) are driven via the three Φ-strobes Φ1, Φ2 and Φ3 which are generated synchronously with PIX-CLK. The Φ-strobe sequence requires about 30 ns to complete. Note that photon counting is inhibited only during the activity interval of the Φ-strobes. Thus, the dead-time of photon counting between successive data acquisition intervals is approximately 30 ns. The typical photon integration time between successive readouts, i.e. the pixel dwell time, is on the order of 10 μs. Therefore, the duty cycle of our instrument is approximately 99.7%. Next, the data transfer from the REGs to the FIFO is mediated by means of a TOKEN (25 ns pulse), i.e. only the TOKEN-receiving FPGA is allowed to transfer its six REG-values to the FIFO. The TOKEN network connects the three FPGAs in a ring-like architecture (c.f. TOKEN_A through TOKEN_E). The initial 'TOKEN_A' is generated by the readout sequence controller (Read-CTRL: XC9536XL,

Xilinx, San Jose, CA) upon sensing a transition of the pixel clock (PIX-CLK). Upon completing its readout sequence, the FSM in the FPGA passes the TOKEN to the next FPGA (or back to the TOKEN Generator). The TOKEN mediated readout process is optimized for speed (no wait-states). The readout cycle of all eighteen channels is completed within 300 ns. Moreover, the TOKEN-concept allows daisy-chaining of multiple mC-PhCC modules, thus, expanding the number of accessible PMT channels (≥ 128). The card-to-card routing of the TOKEN is performed via the X-bar labeled circuitry, a simple jumper-based cross-bar. Note that the figure designates electrical card-to-card connections by bold circles, and all star ($\otimes$) designated components (e.g. FIFO, GigaStar) need to be installed only on the first mC-PhCC module. In step 5, the FIFO data is transmitted to the host computer using either of the two link interfaces. Both, the necessary link handshake signals (READ, READY) and the FIFO read-strobe (RD) are provided by the communication controller chip COM CTRL (XC9536XL, Xilinx, San Jose, CA).

4.2.3. Experimental result and discussion

C Instrument calibration

The discrimination levels for each photon channel are adjusted individually to maximize detection sensitivity while minimizing dark noise. At optimal threshold level, the average dark noise level is approximately 60 counts per second at room temperature which is within the specification provided by the manufacturer, and all channels have uniform sensitivity within 5 % tolerance. The dark noise level is an exponential function of temperature and can be reduced significantly by detector cooling. The spectral range covered by the 16 channels was measured with a series of bandpass filters and white light illumination. For direct coupling of the spectrograph and the PMT we set the spectral range to be approximately 100 nm. The spectral band is found to be linear with channel number. The wavelength range covered by each channel is approximately 7 nm. However, the spectral range can be modified by changing the magnification of the image formed in front to the PMT via relay optics inserted between the spectrograph and the

PMT. The detection efficiency of our instrument is determined mainly by that of the spectrograph and the PMT cathode. The calibration of spectral efficiency is accomplished by using a series of reference fluorophores: POPOP, fluorescein, and rhodamine that jointly span the blue to near infrared spectral range. We further measured the signal loss due to additional de-scanning. Compared to the signal obtained from 'non-descanned' detectors the de-scanned signal is reduced by about 25-30%. The de-scanning losses can be reduced by anti-reflection coating of all optical components in the emission path.

D Spectral imaging of microspheres

In order to demonstrate the spectral resolving capability of our instrument, we imaged a mixture of microspheres that differ in both sizes and spectra. Red, blue and green latex sphere with respective sizes of 1 μm, 2 μm, and 4 μm were used (Molecular Probes, Eugene, OR). The power of the excitation light at the specimen was 5 mW. The images were recorded by means of a Zeiss Fluar 40× oil immersion objective with 1.25 N.A. The image size is $120 \times 120\ \mu m^2$. The spectral range was tuned to span from 448 to 550 nm. Fig. 4-3 shows a representative three-dimensional image cube consisting of sixteen two-dimensional images each at a different spectral band. The spectrally-decomposed images were recorded simultaneously (acquisition time 2.6 s), and no electronic cross talk has been observed between the spectral channels. As shown in Fig. 4-6 (a) and (c), the spheres can be easily distinguished via both the size difference and the spectral information. The 2 μm beads appear only in the 'deep-blue' channels (*c.f.* Fig. 4-6 (a)'s first 3-4 images), the 4 μm beads can be seen throughout the 'blue-green' range (middle 8-9 images), and the 1 μm beads become visible in the 'yellow-red' wavelength regime (last 6-7 images). The spectra obtained from these spheres are comparable to those obtained from standard solution fluorometry. The distinction of fluorophores with greater spectral overlap can be accomplished based on chemometric techniques.[1]

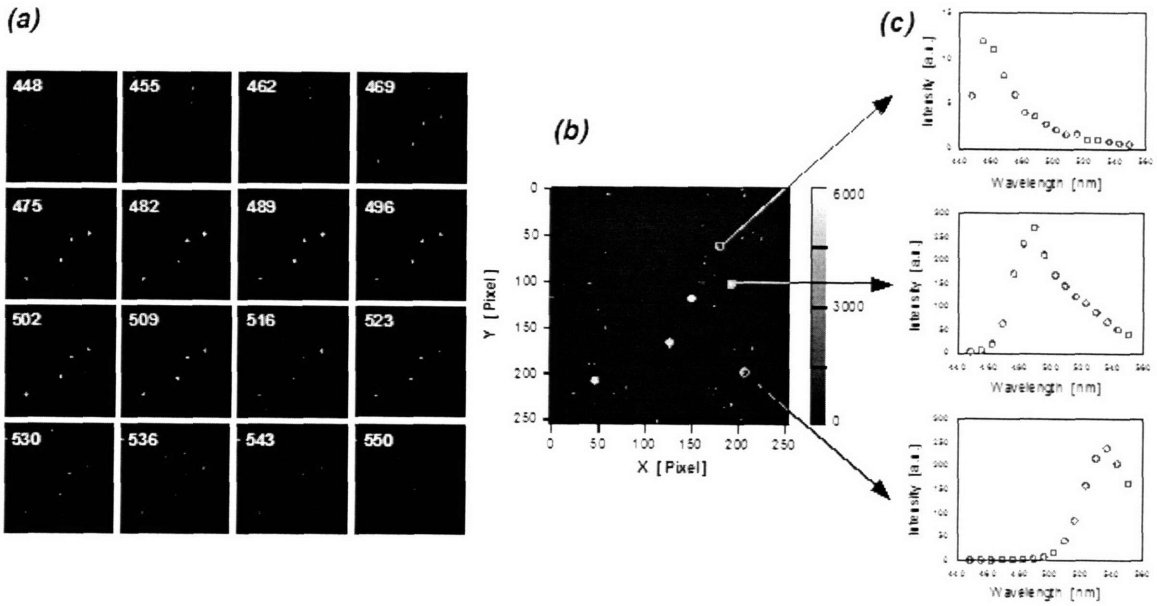

Fig. 4-6: Fluorescence images of *three* different color microspheres. The beads are 1, 2, and 4 μm in diameter with emission peaks at 535, 490, and 455 nm, respectively. The experimental settings are: excitation wavelength: 780 nm, power at the specimen: 5 mW, spectrum range: 100 nm, spectral resolution: 7 nm, acquisition time: 2.6 s. The color (gray level) bar represents intensity. **(a)** Images recorded from individual spectral channels **(b)** An intensity image in which signals from all 16 spectral channels are summed **(c)** Representative spectra of spheres: each of the three fluorescence spectra is derived from a small area around an arbitrary chosen microsphere.

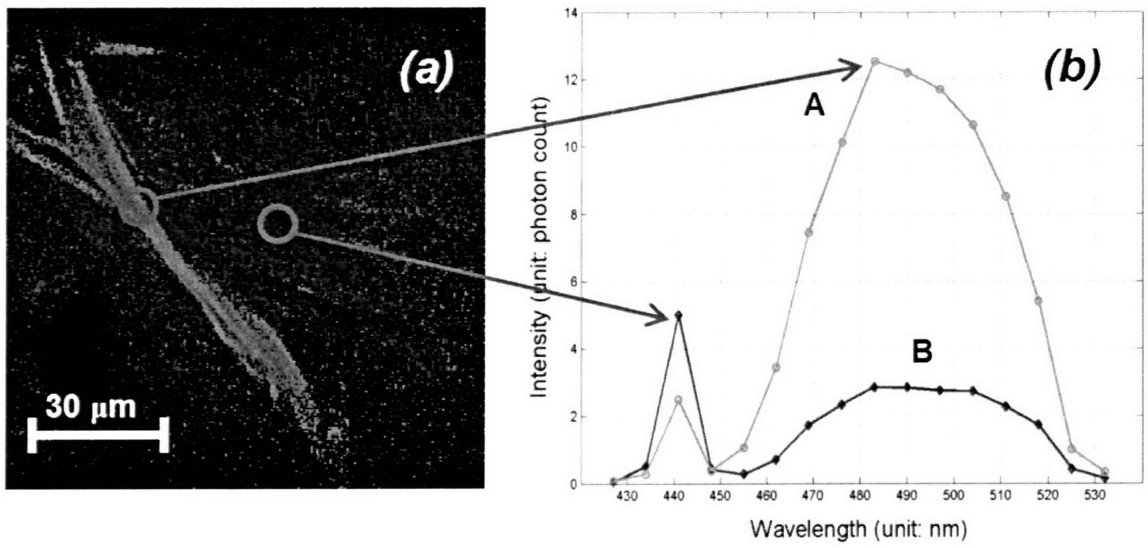

Fig. 4-7: Spectrally resolved imaging of *ex-vivo* human skin (dermal layer). Experimental settings are: excitation wavelength: 880 nm, power at the specimen: 5 mW, spectrum range: 100 nm, spectral resolution: 7 nm, acquisition time: 7 second per frame. (a) Color coded intensity image where blue color represents collagen and green color represents elastin **(b)** Representative spectra at two different positions. Position A corresponds to a collagen-rich area. Position B corresponds to an elastin rich area.

E Spectral tissues imaging

We applied our instrument to spectrally resolve structural components in *ex-vivo* tissues. The specimen studied was ex vivo, previously frozen human skin (obtained from Unilever Research US, courtesy of Dr. Peter Kaplan). Skin is composed of two layers: the top layer called epidermis is approximately 30-40 μm thick. The dermal layer is beneath the epidermal layer with thickness up to 1 mm. The dermal layer is composed mostly of extracellular matrix materials including collagen and elastin which are autofluorescent. At the two-photon excitation wavelength of 880 nm, the elastin fluorescence is efficiently excited but the excitation of collagen fluorescence is not optimal. However, collagen fibers are easily visualized via their second harmonic generated light. The excitation light power at the specimen was 5 mW. The acquired image cube covers a spectral range from 430 to 530 nm in 7 nm intervals, with spatial dimension of 120×120 μm^2. The pixel residence time and the frame acquisition time were 100 μs and 7 seconds, respectively. The depth of the imaging plane was approximately 40 μm below the skin surface. A representative image is shown in Fig. 4-

7. Both the intensity image and spectra from selected regions are shown. The intensity image is false color-labeled according to its spectrum information (channel number). All spectra obtained contain two emission peaks. The narrow emission peak at 440 nm corresponds to second harmonic generation from collagen at exactly half the excitation wavelength. The spectral width of this peak reflects the relatively narrow excitation spectrum of the Ti-Sapphire laser. The second, broader emission peak center at 550 nm corresponds to the autofluorescence of elastin. The measured spectral signature of elastin is consistent with that found in the literature (Freund et al. 1986). Based on spectral decomposition, we see that the large coarse fibers correspond to elastin-rich regions in the skin whereas the fine fibrous background corresponds to collagen-rich regions.

4.2.4. Conclusions

A spectrally resolved multi-photon microscope has been developed using multi-anode photomultiplier detectors operating in single photon counting mode. For high sensitivity detection using multi-anode PMTs, a dedicated multi-channel photon counter card (mC-PhCC) has been developed. Single photon counting from multi-anode PMT detectors open exciting opportunities for novel instrument development such as developing multi-focal multi-photon microscopes based on multi-anode PMTs instead of high cost CCD detectors.

Chapter 5

Conclusion

5.1. Summary

The technology of high-speed two-photon microscopy (HSTPM) has been successfully advanced in this thesis. We have implemented two versions of HSTPM.. A HSTPM based on polygonal mirror can achieve the imaging speed of 13 frames/s in tissues. This system is based on single-focus scanning and signal collection with large, non-spatial resolved detectors such as PMTs. It has excellent performance in the imaging of thick, turbid tissues. Importantly, this system delivers minimal photodamage as compared with wide field or confocal microscopes as demonstrated in the imaging of live protozoa motion. Since further speed increase in TPM is restricted by the lifetime of the fluorophores in the specimen and not by the excitation power delivered to the focal volume, the improvement of imaging speed in a single focus system is ultimately limited. The use of multifocal multiphoton microscopy can overcome this limitation. MMM allows high-speed imaging by parallelizing the image process. However, the application of MMM to deep tissue imaging remained unproven. We thoroughly investigated the effect of emission photon scattering, which was identified as the key limitation of applying MMM to deep tissue imaging. We provided the first experimental result of the emission point spread function variation in TPM as a function of the scattering length of the specimen. Our knowledge of the emission point spread function allowed us to design a novel MMM based on multi-anode multi-anode photomultiplier (MAPMT) detectors. Using this novel detector and applying a deconvolution approach, we demonstrated that this system has performance of tissue imaging almost comparable with conventional TPM in terms of imaging depth but can image at significantly higher speed. We believe that MAPMT based MMM can rival conventional TPM for deep tissue imaging but with significantly higher imaging speed.

The utility of these HSTPMs is demonstrated by a number of biomedical studies. In a study of transdermal transport with chemical enhancer, the HSTPM was able to measure the change of skin microscale transport properties in the presence of chemical enhancer even in topographically heterogeneous tissues. This study was the first highly quantitative measurement of microscopic transport coefficients in skin. We also elucidated the relative importance of various transdermal drug delivery pathways in skin for both hydrophoblic and hydrophilic molecules. In study of tumor physiology, tumor vasculature and lymphatic structures that were several hundred microns below the surface were characterized with in vivo two-photon imaging in real time allowing leukocyte-endothelium interaction to be first imaged in 3D. Finally, we have developed a novel method of 3D tissue cytometry based on HSTPM allowing the characterization of cell-cell, cell-tissue interaction to be quantified in 3D tissue. We have successfully applied this system to local cells underwent mitotic recombination in a novel mouse model.

5.2. Future outlook

The quantification of biology based on genomic and proteomic information opens the opportunity to understand tissue physiology and pathology on the molecular level. HSTPM will be used a valuable measurement tool to expand our molecular level understanding of tissues based on large section imaging. 3D imaging of sample on the size scale of cubic centimeters allow the study of whole organ physiology with cellular and molecular resolution. This information may be used to correlate and to elucidate tissue level diseases with cellular and molecular level changes on the mechanistic level. To image large tissue sections within a reasonable time, other instrument developments such as a high speed robotic sample stage needs to be optimized and integrated with HSTPM. Recently, a whole organ of mouse heart was imaged with a HSTPM and its complete 3D morphological information with subcellular resolution was obtained based on HSTPM technologies developed in this thesis (Ragan et al. 2005). This work demonstrates the potential of HSTPM technology in revolutionizing the field of physionomics.

Bibliography

1. Bennett, B. D., Jetton, T. L., Ying, G. T., Magnuson, M. A. and Piston, D. W. (1996). "Quantitative subcellular imaging of glucose metabolism within intact pancreatic islets." J. Bio. Chem. 271(7): 3647-3651.

2. Bewersdorf, J., Pick, R. and Hell, S. W. (1998). "Multifocal multiphoton microscopy." Opt. Lett. 23(9): 655-657.

3. Brakenhoff, G. J., Squier, J., Norris, T., Bliton, A. C., Wade, M. H. and Athey, B. (1996). "Real-time two-photon confocal microscopy using a femtosecond, amplified Ti:sapphire system." Journal of microscopy-oxford 181: 253-259 Part 3.

4. Buehler, C., Kim, K. H., Dong, C. Y., Masters, B. R. and So, P. T. C. (1999). "Innovations in two-photon deep tissue microscopy." IEEE Eng. Med. Biol. 18(5): 23-30.

5. Buist, A. H., Muller, M., Squier, J. and Brakenhoff, G. J. (1998). "Real time two-photon absorption microscopy using multi point excitation." J. Micros.-Oxf. 192: 217-226.

6. Centonze, V. E. and White, J. G. (1998). "Multiphoton excitation provides optical sections from deeper within scattering specimens than confocal imaging." Biophysical journal 75(4): 2015-2024.

7. Denk, W. (1994). "2-photon scanning photochemical microscopy." PNAS 91(14): 6629-6633.

8. Denk, W., Delaney, K. R., Gelperin, A., Kleinfeld, D., Strowbridge, B. W., Tank, D. W. and Yuste, R. (1994). "Anatomical and functional imaging of neurons using 2-photon laser-scanning microscopy." Journal of neuroscience methods 54(2): 151-162.

9. Denk, W., Strickler, J. H. and Webb, W. W. (1990). "2-photon laser scanning fluorescence microscopy." Science 248(4951): 73-76.

10. Engert, F. and Bonhoeffer, T. (1999). "Dendritic spine changes associated with hippocampal long-term synaptic plasticity." Nature 399(6731): 66-70.

11. Fan, G. Y., Fujisaki, H., Miyawaki, A., Tsay, R.-K., Tsien, R. Y. and Ellisman, M. H. (1999). "Video-Rate Scanning Two-Photon Excitation Fluorescence Microscopy and Ratio Imaging with Cameleons." Biophy. J. 78: 2412-2420.

12. Grutzendler, J., Kasthuri, N. and Gan, W.-B. (2002). "Long-term dendritic spine stability in the adult cortex." Nature 420(19): 812-816.

13. Helmchen, F., Svoboda, K., Denk, W. and Tank, D. W. (1999). "In vivo dendritic calcium dynamics in deep-layer cortical pyramidal neurons." Nature Neuroscience 2(11): 989-996.

14. Hockberger, P. E., Skimina, T. A., Centonze, V. E., Lavin, C., Chu, S., Dadras, S., Reddy, J. K. and White, J. G. (1999). "Activation of flavin-containing oxidases underlies light-induced production of H2O2 in mammalian cells." PNAS 96(11): 6255-6260.

15. Jacques, S. L., McAuliffe, D. J., Blank, I. H. and Parrish, J. A. (1987). "Controlled removal of human stratum-corneum by pulsed laser." Journal of investigative dermatology **88**(1): 88-93.

16. Jones, K. T., Soeller, C. and Cannel, M. B. (1998). "The passage of Ca2+ and fluorescent markers between the sperm and egg after fusion in the mouse." Development **125**(23): 4627-4635.

17. Keyse, S. M. and Tyrrell, R. M. (1990). "Induction of the heme oxygenase gene in human skin fibroblasts by hydrogen-peroxide and UVA (365 nm) radiation - evidence for the involvement of the hydroxyl radical." Carcinogenesis **11**(5): 787-791.

18. Kleinfeld, D., Mitra, P. P., Helmchen, F. and Denk, W. (1998). "Fluctuations and stimulus-induced changes in blood flow observed in individual capillaries in layers 2 through 4 of rat neocortex." PNAS **95**(26): 15741-15746.

19. Koester, H. J., Baur, D., Uhl, R. and Hell, S. W. (1999). "Ca2+ fluorescence imaging with pico- and femtosecond two-photon excitation: Signal and photodamage." Biophysical journal **77**(4): 2226-2236.

20. Konig, K., Becker, T. W., Fischer, P., Riemann, I. and Halbhuber, K. J. (1999). "Pulse-length dependence of cellular response to intense near-infrared laser pulses in multiphoton microscopes." Optics letters **24**(2): 113-115.

21. Konig, K., So, P. T. C., Mantulin, W. W., Tromberg, B. J. and Gratton, E. (1996). "Two-photon excited lifetime imaging of autofluorescence in cells during UVA and NIR photostress." Journal of microscopy-oxford **183**: 197-204.

22. Mainen, Z. F., Malinow, R. and Svoboda, K. (1999). "Synaptic calcium transients in single spines indicate that NMDA receptors are not saturated." Nature **399**(6732): 151-155.

23. Maletic-Savatic, M., Malinow, R. and Svoboda, K. (1999). "Rapid dendritic morphogenesis in CA1 hippocampal dendrites induced by synaptic activity." Science **283**(5409): 1923-1927.

24. Masters, B. R., So, P. T. C., Buehler, C., Barry, N., Sutin, J. D., Mantulin, W. W. and Gratton, E. (2004). "Mitigating thermal mechanical damage potential during two-photon dermal imaging." Journal of biomedical optics **9**(6): 1265-1270.

25. Masters, B. R., So, P. T. C. and Gratton, E. (1997). "Multiphoton excitation fluorescence microscopy and spectroscopy of in vivo human skin." Biophys. J. **72**(6): 2405-2412.

26. Mohler, W. A., Simske, J. S., Williams-Masson, E. M., Hardin, J. D. and White, J. G. (1998). "Dynamics and ultrastructure of developmental cell fusions in the Caenorhabditis elegans hypodermis." Current biology **8**(19): 1087-1090.

27. Mohler, W. A. and White, J. G. (1998). "Stereo-4-D reconstruction and animation from living fluorescent specimens." Biotech. **24**: 1006-1012.

28. Piston, D. W., Knobel, S. M., Postic, C., Shelton, K. D. and Magnuson, M. A. (1999). "Adenovirus-mediated knockout of a conditional glucokinase gene in isolated pancreatic islets reveals an essential role for proximal metabolic coupling events in glucose-stimulated insulin secretion." Journal of biological chemistry **274**(2): 1000-1004.

29. Piston, D. W., Masters, B. R. and Webb, W. W. (1995). "3-Dimensionally resolved NAD(P)H cellular metabolic redox imaging of the in-situ cornea with 2-photon excitation laser-scanning microscopy." Journal of microscopy-oxford **178**: 20-27 Part 1.

30. Pustavalov, V. K. (1995). "Initiation of explosive boiling and optical breakdown as a result of the action of laser pulses on melanosome in pigmented biotissues." Kvantovaya elektronika **22**(11): 1091-1095.

31. Sako, Y., Sekihata, A., Yanagisawa, Y., Yamamoto, M., Shimada, Y., Ozaki, K. and Kusumi, A. (1997). "Comparison of two-photon excitation laser scanning microscopy with UV-confocal laser scanning microscopy in three-dimensional calcium imaging using the fluorescence indicator Indo-1." Journal of microscopy-oxford **185**(Part 1): 9-20.

32. Schonle, A. and Hell, S. W. (1998). "Heating by absorption in the focus of an objective lens." Optics letters **23**(5): 325-327.

33. Shi, S. H., Hayashi, Y., Petralia, R. S., Zaman, S. H., Wenthold, R. J., Svoboda, K. and Malinow, R. (1999). "Rapid spine delivery and redistribution of AMPA receptors after synaptic NMDA receptor activation." Science **284**(5421): 1811-1816.

34. So, P. T. C., Kim, H. and Kochevar, I. E. (1998). "Two-photon deep tissue ex vivo imaging of mouse dermal and subcutaneous structures." OPTICS EXPRESS **3**(9): 339-350.

35. Squirrell, J. M., Wokosin, D. L., White, J. G. and Bavister, B. D. (1999). "Long-term two-photon fluorescence imaging of mammalian embryos without compromising viability." Nature Biotech. **17**(8): 763-767.

36. Svoboda, K., Denk, W., Kleinfeld, D. and Tank, D. W. (1997). "In vivo dendritic calcium dynamics in neocortical pyramidal neurons." Nature **385**(6612): 161-165.

37. Svoboda, K., Helmchen, F., Denk, W. and Tank, D. W. (1999). "Spread of dendritic excitation in layer 2/3 pyramidal neurons in rat barrel cortex in vivo." Nature Neuroscience **2**(1): 65-73.

38. Trachtenberg, J. T., Chen, B. E., Knott, G. W., Feng, G., Sanes, J. R., Welker, E. and Svoboda, K. (2002). "Long-term in vivo imaging of experience-dependent synaptic plasticity in adult cortex." Nature **420**(19): 788-794.

39. Tyrrell, R. M. and Keyse, S. M. (1990). "New trends in photobiology - the interaction of UVA radiation with cultured-cells." Journal of photochemistry and photobiology B-Biology **4**(4): 349-361.

40. Yuste, R., Majewska, A., Cash, S. S. and Denk, W. (1999). "Mechanisms of calcium influx into hippocampal spines: Heterogeneity among spines, coincidence detection by NMDA receptors, and optical quantal anaysis." Journal of neuroscience **19**(6): 1976-1987.

41. Bommannan, D., Potts, R. O. and Guy, R. H. (1990). Examination of the stratum corneum barrier function in vivo by infrared spectroscopy, Journal of investigative dermatology **95**: 403-408.

42. Centonze, V. E. and White, J. G. (1998). Multiphoton excitation provides optical sections from deeper within scattering specimens than confocal imaging, Biophysical journal **75**(4): 2015-2024.

43. Cullander, C. and Guy, R. H. (1992). (D) Routes of delivery: case studies (6), Adv. Drug. Deliv. Rev. **8**: 291-329.

44. Finnin, B. C. and Morgan, T. M. (1999). Transdermal penetration enhancers: applications, limitations, and potential, J. Pharm. Sci. **88**: 955-958.

45. Francouer, M. L., Golden, G. M. and Potts, R. O. (1990). Oleic acid: Its effect on stratum corneum in relation to (trans)dermal drug delivery, Pharm. Res **7**(6): 621-627.

46. Golden, G. M., McKie, J. E. and Potts, R. O. (1987). Role of stratum corneum lipid fluidity in transdermal drug flux, J. Pharm. Sci. **76**: 25-28.

47. Gonzalez, S., Zonios, G., Ngyugen, B. G., Gillies, R. and Kollias, N. (2000). Endogenous skin autofluorescence is a good marker for objective evaluation of comedolysis, Journal of investigative dermatology **115**: 100-105.

48. Jain, R. K. (1999). Understanding barriers to drug delivery: High resolution in vivo imaging is key, Clin. Cancer. Res. **5**: 1605-1606.

49. Jain, R. K., Munn, L. L. and Fukumura, D. (2001). Transparent window models and intravital microscopy in: Tumor models in cancer research. Totowa, NJ, Humana Press.

50. Johnson, M. E., Berk, D. A., Blankenstein, D., Golan, D. E., Jain, R. K. and Langer, R. S. (1996a). lateral diffusion of small compounds in human stratum corneum and model lipid bilayer systems, Biophysical journal **71**: 2656-2668.

51. Johnson, M. E., Mitragotri, S., Patel, A., Blankenstein, D. and Langer, R. (1996b). Synergistic effects of chemical enhancers and therpeutic ultrasound on transdermal drug delivery, J. Pharm. Sci. **85**: 670-679.

52. Kim, K. H., Buehler, C. and So, P. T. C. (1999). High-speed two-photon scanning microscope, App. Opt. **38**(28): 6004-6009.

53. Kollias, N., Gillies, R., Moran, M., Kochevar, I. E. and Anderson, R. R. (1998). Endogenous skin fluorescence includes bands that may serve as quantitative markers of aging and photoaging, Journal of investigative dermatology **111**: 776-780.

54. Leunig, M., Yuan, F., Menger, M. D., Boucher, Y., Goetz, A. E., Messmer, K. and Jain, R. K. (1992). Angiogenesis, microvascular architecture, microhemodynamics, and interstitial fluid pressure during early growth of human adenocarcinoma LS174T in SCID mice, Cancer Res. **52**: 6553-6560.

55. Li, S. K., Suh, W., Parikh, H. H., Ghanem, A. H., Mehta, S. C., Peck, K. D. and Higuchi, W. I. (1998). Lag time data for characterizing the pore pathway of intact and chemically pretreated human epidermal membrane, Int. J. Pharm **170**: 93-108.

56. Masters, B. R., So, P. T. C. and Gratton, E. (1997). Multiphoton excitation fluorescence microscopy and spectroscopy of in vivo human skin, Biophys. J. **72**(6): 2405-2412.

57. Masters, B. R., So, P. T. C. and Gratton, E. (1998). Optical biopsy of in vivo human skin: Multi-photon excitation microscopy, LASERS IN MEDICAL SCIENCE **13**(3): 196-203.

58. Matoltsy, A. G. (1976). Keratinization, Journal of investigative dermatology **67**: 20-25.

59. Mohler, W. A., Simske, J. S., Williams-Masson, E. M., Hardin, J. D. and White, J. G. (1998). Dynamics and ultrastructure of developmental cell fusions in the Caenorhabditis elegans hypodermis, Current biology **8**(19): 1087-1090.

60. Mohler, W. A. and White, J. G. (1998). Stereo-4-D reconstruction and animation from living fluorescent specimens, Biotech. **24**: 1006-1012.

61. Na, R., Stender, I.-M., Henriksen, M. and Wulf, H. C. (2001). Autofluorescence of human skin is age-related after correction for skin pigmentation and redness, Journal of investigative dermatology **116**: 536-540.

62. Naik, A., Pechtold, L. A. R. M., Potts, R. O. and Guy, R. H. (1995). Mechanism of oleic acid-induced skin penetration enhancement in vivo in humans, J. Control. Rel. **37**: 299-306.

63. Padera, T. P., Stoll, B. R., So, P. T. C. and Jain, R. K. (2002). Conventional and High-Speed Intravital Multiphoton Laser Scanning Microscopy of Microvasculature, Lymphatics, and Leukocyte.Endothelial Interactions, Molecular Imaging **1**: 9-15.

64. Peck, K. D., Ghanem, A. H. and Higuchi, W. I. (1994). Hindered diffusion of polar molecules through and effective pore radii estimates of intact and ethanol treated human epidermal membrane, Pharm. Res **11**: 1306-1314.

65. Peck, K. D., Hsu, J., Lee, S. K., Ghanem, A.-H. and Higuchi, W. I. (1998). Flux enhancement effects of ionic surfactants upon passive and electroosmotic transdermal transport, J. Pharm. Sci. **87**: 1161-1169.

66. Potts, R. O. and Francoeur, M. L. (1991). The influence of stratum corneum morphology on water permeability, Journal of investigative dermatology **96**: 495-499.

67. Schaefer, H. and Redelmeier, T. E. (1996). Skin Barrier. Basel, Karger.

68. Scheuplein, R. J. and Blank, I. H. (1971). Permeability of the skin, Physiol. Rev. **51**: 702-747.

69. Squirrell, J. M., Wokosin, D. L., White, J. G. and Bavister, B. D. (1999). Long-term two-photon fluorescence imaging of mammalian embryos without compromising viability, Nature Biotech. **17**(8): 763-767.

70. Yoneto, K., Ghanem, A. H., Higuchi, W. I., Peck, K. D. and Li, S. K. (1995). Mechanistic studies of the 1-alkyl-2-pyrrolidones as skin permeation enhancers, J. Pharm. Sci. **84**: 312-317.

71. Yu, B., Dong, C.-Y., So, P. T. C., Blankschtein, D. and Langer, R. (2001). In Vitro Visualization and Quantification of Oleic Acid Induced Changes in Transdermal Transport Using Two-Photon Fluorescence Microscopy, J. Invest. Dermatol. **117**: 16-25.

72. Yu, B., Kim, K. H., So, P. T. C., Blankschtein, D. and Langer, R. (2002). Topographic Heterogeneity in Transdermal Transport Revealed by High-Speed Two-Photon Microscopy: Determination of Representative Skin Sample Sizes, J. Invest. Dermatol. **118**:1085±1088.

73. Yu, B., Kim, K. H., So, P. T. C., Blankschtein, D. and Langer, R. (2003). Evaluation of Fluorescent Probe Surface Intensities as an Indicator of Transdermal Permeant Distributions Using Wide-Area Two-Photon Fluorescence Microscopy, Journal of pharmaceutical sciences **92**(12): 2354-2365.

74. Yu, B., Kim, K. H., So, P. T. C., Blankschtein, D. and Langer, R. (2003). Visualization of Oleic Acid-induced Transdermal Diffusion Pathways Using Two-photon Fluorescence Microscopy, J. Invest. Dermatol. **120**: 448-455.

75. Beaurepaire, E. and J. Mertz (2002). "Epifluorescence collection in two-photon microscopy." App. Opt. **41**(25): 5376-5382.

76. Bewersdorf, J., R. Pick, et al. (1998). "Multifocal multiphoton microscopy." Opt. Lett. **23**(9): 655-657.

77. Blanca, C. M. and C. Saloma (1998). "Monte Carlo analysis of two-photon fluorescence imaging through a scattering medium." App. Opt. **37**(34): 8092-8102.

78. Buist, A. H., M. Muller, et al. (1998). "Real time two-photon absorption microscopy using multi point excitation." J. Micros.-Oxf. **192**: 217-226.

79. Dong, C. Y., K. Koenig, et al. (2003). "Characterizing point spread functions of two-photon fluorescence microscopy in turbid medium." J. Biomed. Opt. **8**(3): 450-459.

80. Dunn, A. K., V. P. Wallace, et al. (2000). "Influence of optical properties on two-photon fluorescence imaging in turbid samples." App. Opt. **39**(7): 1194-1201.

81. Fan, G. Y., H. Fujisaki, et al. (1999). "Video-Rate Scanning Two-Photon Excitation Fluorescence Microscopy and Ratio Imaging with Cameleons." Biophy. J. **78**: 2412-2420.

82. Fantini, S., M. A. Franceshini, et al. (1994). "Semi-infinite-geometry boundary problem for light migration in highly scattering media: a frequency-domain study in the diffusion approximation." J. Opt. Soc. Am. B **11**(10): 2128-2138.

83. Feng, G., R. H. Mellor, et al. (2000). "Imaging neuronal subsets in transgenic mice expressing multiple spectral variants of GFP." Neuron **28**: 41-51.

84. Gan, X. and M. Gu (2000). "Spatial distribution of single-photon and two-photon fluorescence light in scattering media: Monte Carlo simulation." App. Opt. **39**(10): 1575-1579.

85. Kim, K. H., C. Buehler, et al. (1999). "High-speed two-photon scanning microscope." App. Opt. **38**(28): 6004-6009.

86. Oheim, M., E. Beaurepaire, et al. (2001). "Two-photon microscopy in brain tissue: parameters influencing the imaging depth." J. Neuro. Method. **111**: 29-37.

87. Ying, J., F. Liu, et al. (1999). "Spatial distribution of two-photon-excited fluorescence in scattering media." App. Opt. **38**(1): 224-229.

88. Yu, B., K. H. Kim, et al. (2002). "Topographic Heterogeneity in Transdermal Transport Revealed by High-Speed Two-Photon Microscopy: Determination of Representative Skin Sample Sizes." J. Invest. Dermatol. **118**:1085±1088.

89. Bewersdorf, J., Pick, R. and Hell, S. W. (1998). Multifocal multiphoton microscopy, Opt. Lett. **23**(9): 655-657.

90. Buehler, C., Kim, K. H., Greuter, U., Schlumpf, N. and So, P. T. C. (2005). Single-photon counting multicolor multiphoton fluorescence microscope, Journal of fluorescence **15**(1): 41-51.

91. Buist, A. H., Muller, M., Squier, J. and Brakenhoff, G. J. (1998). Real time two-photon absorption microscopy using multi point excitation, J. Micros.-Oxf. **192**: 217-226.

92. Dong, C. Y., Koenig, K. and So, P. T. C. (2003). Characterizing point spread functions of two-photon fluorescence microscopy in turbid medium, J. Biomed. Opt. **8**(3): 450-459.

93. Fantini, S., Franceshini, M. A. and Gratton, E. (1994). Semi-infinite-geometry boundary problem for light migration in highly scattering media: a frequency-domain study in the diffusion approximation, J. Opt. Soc. Am. B **11**(10): 2128-2138.

94. Feng, G., Mellor, R. H., Bernstein, M., Wallace, M., Nerbonne, J. M., Lichtman, J. W. and Sanes, J. R. (2000). Imaging neuronal subsets in transgenic mice expressing multiple spectral variants of GFP, Neuron **28**: 41-51.

95. Kim, K. H., Buehler, C., Heffer, E., Fantini, S. and So, P. T. C. (2005). Implications in tissue turbidity in multifocal multiphoton microscopy, In preparation for optics letters.

96. Kim, K. H., Ragan, T., Previte, M. J. R., Bahlmann, K., Harley, B. A., Stitt, M. S., Hendricks, C. A., Almeida, K. H., Engelward, B. P. and So, P. T. C. (2005). Three-dimensional tissue cytometer based on high-speed multiphoton microscopy, In preparation for cytometry.

97. Masters, B. R., So, P. T. C., Buehler, C., Barry, N., Sutin, J. D., Mantulin, W. W. and Gratton, E. (2004). Mitigating thermal mechanical damage potential during two-photon dermal imaging, Journal of biomedical optics **9**(6): 1265-1270.

98. Masters, B. R., So, P. T. C. and Gratton, E. (1997). Multiphoton excitation fluorescence microscopy and spectroscopy of in vivo human skin, Biophys. J. **72**(6): 2405-2412.

99. Nielsen, T., Frick, M., Hellweg, D. and Andresen, P. (2001). High efficiency beam splitter for multifocal multiphoton microscopy, Journal of microscopy-oxford **201**: 368-376.

100. So, P. T. C., Dong, C. Y., Masters, B. R. and Berland, K. M. (2000). Two-photon excitation fluorescence microscopy, Annual review of biomedical engineering **2**: 399-429.

101. So, P. T. C., Kim, H. and Kochevar, I. E. (1998). Two-photon deep tissue ex vivo imaging of mouse dermal and subcutaneous structures, OPTICS EXPRESS **3**(9): 339-350.

102. Bennett, B. D., Jetton, T. L., Ying, G. T., Magnuson, M. A. and Piston, D. W. (1996). Quantitative subcellular imaging of glucose metabolism within intact pancreatic islets, J. Bio. Chem. **271**(7): 3647-3651.

103. Buehler, C., Kim, K. H., Greuter, U., Schlumpf, N. and So, P. T. C. (2005). Single-photon counting multicolor multiphoton fluorescence microscope, Journal of fluorescence **15**(1): 41-51.

104. Darzynkiewicz, Z., Bedner, E., Li, X., Gorczyca, W. and Melamed, M. R. (1999). Laser-scanning cytometry: a new instrumentation with many applications, Experimetal Cell Research **249**: 1-12.

105. Davies, J. A. (2001). Extracellular matrix, Encyclopedia of life sciences.

106. Denk, W., Strickler, J. H. and Webb, W. W. (1990). 2-photon laser scanning fluorescence microscopy, Science **248**(4951): 73-76.

107. Ecker, R. C. and Steiner, G. E. (2004). Microscopy-based multicolor tissue cytometry at the single-cell level, Cytometry Part A **59A**: 182-190.

108. Gerstner, A. O. H., Trumpfheller, C., Racz, P., Osmancik, P., Tenner-Racz, K. and Tarnok, A. (2004). Quantitative histology by multicolor slide-based cytometry, Cytometry Part A **59A**: 210-219.

109. Gohongi, T., Fukumura, D., Boucher, Y., Yun, C. O., Soff, G. A., Compton, C., Todoroki, T. and Jain, R. K. (1999). Tumor-host interactions in the gallbladder suppress distal angiogenesis and tumor growth: involvement of transforming growth factor beta1, Nat Med **5**(10): 1203-8.

110. Hendricks, C. A., Almeida, K. H., Stitt, M. S., Jonnalagadda, V. S., Rugo, R. E., Kerrison, G. F. and Engelward, B. P. (2003). Spontaneous mitotic homologous recombination at an enhanced yellow fluorescent protein (EYFP) cDNA direct repeat in transgenic mice, PNAS **100**(11): 6325-6330.

111. Hendricks, C. A. and Engelward, B. P. (2004). "Recombomice": the past, present, and future of recombination-detection in mice, DNA Repair **3**: 1255-1261.

112. Kim, K. H., Bahlmann, K. and So, P. T. C. (2005). Multifocal multiphoton microscope based on multi-anode photomultiplier tube for tissue imaging, In preparation for optics express.

113. Kim, K. H., Buehler, C. and So, P. T. C. (1999). High-speed two-photon scanning microscope, App. Opt. **38**(28): 6004-6009.

114. Knezevic, V., Leethanakul, C., Bichsel, V. E., Worth, J. M., Prabhu, V. V., Gutkind, J. S., Liotta, L. A., Munson, P. J., Petricoin, E. F., 3rd and Krizman, D. B. (2001). Proteomic profiling of the cancer microenvironment by antibody arrays, Proteomics **1**(10): 1271-8.

115. Leethanakul, C., Knezevic, V., Patel, V., Amornphimoltham, P., Gillespie, J., Shillitoe, E. J., Emko, P., Park, M. H., Emmert-Buck, M. R., Strausberg, R. L., Krizman, D. B. and Gutkind, J. S. (2003). Gene discovery in oral squamous cell carcinoma through the Head and Neck Cancer Genome Anatomy Project: confirmation by microarray analysis, Oral Oncol **39**(3): 248-58.

116. Liotta, L. A. and Kohn, E. C. (2001). The microenvironment of the tumour-host interface, Nature **411**(6835): 375-9.

117. Muller, M. G., Valdez, T. A., Georgakoudi, I., Backman, V., Fuentes, C., Kabani, S., Laver, N., Wang, Z. M., Boone, C. W., Dasari, R. R., Shapshay, S. M. and Feld, M. S. (2003). Spectroscopic detection and evaluation of morphologic and biochemical changes in early human oral carcinoma, Cancer **97**(7): 1681-1692.

118. Nielsen, T., Frick, M., Hellweg, D. and Andresen, P. (2001). High efficiency beam splitter for multifocal multiphoton microscopy, Journal of microscopy-oxford **201**: 368-376.

119. O'Brien, F. J., Harley, B. A., Yannas, I. V. and Gibson, L. J. (2005). The effect of pore size on cell adhesion in collagen-GAG scaffolds, Biomaterials **26**: 433-441.

120. Rieseberg, M., Kasper, C., Reardon, K. F. and Scheper, T. (2001). Flow cytometry in biotechnology, Appl. Microbiol. Biotechnol. **56**: 350-360.

121. So, P. T. C., Dong, C. Y., Masters, B. R. and Berland, K. M. (2000). Two-photon excitation fluorescence microscopy, Annual review of biomedical engineering **2**: 399-429.

122. Steiner, G. E., Ecker, R. C., Kramer, G., Stockenhuber, F. and Marberger, M. J. (2000). Automated data acquisition by confocal laser scanning microscopy and image analysis of triple stained immunofluorescent leukocytes in tissue, Journal of Immunological Methods **237**: 39-50.

123. Stitt, M. S. (2001). Fluorescence detection of recombination in mammalian cells and mice. Toxicology. Cambridge, Massachusetts Institute of Technology.

124. Tarnok, A. and Gerstner, A. O. H. (2002). Clinical applications of laser scanning cytometry, Cytometry **50**: 133-143.

125. Corcuff, P., Bertrand, C. and Leveque, J. L. (1993). Morphometry of human epidermis in vivo by real-time confocal microscopy, Arch. Dermatol. Res. **285**: 475-481.

126. Corcuff, P. and Leveque, J. L. (1993). In vivo vision of the human skin with the tandem scanning microscope, Dermatology **186**: 50-54.

127. Masters, B. R., So, P. T. C. and Gratton, E. (1997). Multiphoton excitation fluorescence microscopy and spectroscopy of in vivo human skin, Biophys. J. **72**(6): 2405-2412.

128. Masters, B. R., So, P. T. C. and Gratton, E. (1998). Optical biopsy of in vivo human skin: Multi-photon excitation microscopy, LASERS IN MEDICAL SCIENCE **13**(3): 196-203.

129. Petran, M., Hadravasky, M., Egger, M. D. and Galambas, R. (1968). Tandem scanning opitcal microscope, J. Opt. Soc. Am. **58**: 661-664.

130. Rajadhyaksha, M., Grossman, M., Estrowitz, D. and Webb, R. H. (1995). In-vivo confocal scanning laser microscopy of human kin - melanin provides strong contrast, Journal of investigative dermatology **104**(6): 946-952.

131. So, P. T. C., Dong, C. Y., Masters, B. R. and Berland, K. M. (2000). Two-photon excitation fluorescence microscopy, Annual review of biomedical engineering **2**: 399-429.